

Separating Xylene Isomers by Commensurate Stacking of *p*-Xylene within Channels of MAF-X8**

Ariana Torres-Knoop, Rajamani Krishna, and David Dubbeldam*

Abstract: The development of energy-efficient processes for selective separation of *p*-xylene from mixtures with its isomers is of vital importance in the petrochemical industries. Current industrial practice uses BaX zeolite that has high adsorption selectivity for *p*-xylene. Finding *para*-selective structures is challenging. With state-of-the-art simulation methodologies we systematically screened a wide variety of zeolites and metal–organic frameworks (MOFs). Our investigations highlight the crucial importance of the channel dimension on the separation. MAF-X8 is particularly noteworthy because the channel dimensions and geometry allow “commensurate stacking” which we exploit as a separation mechanism at saturation conditions. Due to a significantly improved capacity compared to BaX, the cycle times for *p*-xylene with MAF-X8 are found to be about a factor of 4.5 longer. This is expected to result in significant process improvements.

The separation of C₈ aromatic hydrocarbons is of great importance in the petrochemical industries. Some mixed xylenes are used for blending in gasoline, as solvents, and in the printing, rubber, and leather industries.^[1] Most mixed xylenes are separated and the individual isomers consumed in specific end-uses. *para*-Xylene, the most valuable of the isomers, is primarily used as a feedstock with purity requirements of 99% + for terephthalic acid or dimethyl terephthalate production, whose end-use includes polyester fibers and polyethylene terephthalate (PET) resins for beverage bottles.^[2] The separation of C₈ aromatic hydrocarbons is difficult because of the small differences in the boiling points (Figure 1). There are, however, significant differences in the freezing points that allow fractional crystallization to be used for separations.^[3] The differences in the freezing points arise because of differences in the stacking efficiency of molecules. *para*-Xylene has the highest freezing point because the molecules stack most efficiently; pure *p*-xylene crystals are the first to emerge from the solution. However, the energy requirements for fractional crystallization are high because of

the need to cool to temperatures of about 220 K. Selective adsorption of xylene isomers within the pores of ordered crystalline microporous materials is an energy efficient alternative to fractional crystallization.^[4] In industrial processing, the feed to the xylene separation unit is most commonly in the liquid phase, and the operation is performed under conditions of pore saturation. At these conditions, differences in saturation capacity are of great importance in determining separations (as explained in detail in Section S5). Because of the low *p*-xylene content of the feed it is often easier to reach a high productivity with *p*-xylene-selective adsorbents.^[4]

Thanks to early simulation work on xylenes in zeolites, for example by Snurr et al.,^[5] molecular simulations have now sufficiently evolved in speed and accuracy that large-scale screening studies have become feasible. Moghadam and Düren^[6] found that small-pore structures are *para*-selective and slightly larger pores are *ortho*-selective. However, this *para*-selectivity mechanism is based on “sieving”: the channel-dimensions are selected such that *p*-xylene is adsorbed and the larger *o*- and *m*-xylene are excluded from the channels. Sieving is therefore usually associated with small-pore systems with low *p*-xylene loadings. Moreover, such sieving is unable to separate *p*-xylene from ethylbenzene because of the diffusional limitations in such systems.


To search for systems that are superior to the current technology (BaX zeolite adsorbent used in UOP Parex and IFP Eluxyl, which employ simulated moving beds^[4,7,8]), we require 1) a high *para*-selective structure, 2) with a high pore volume, and 3) a structure that is able to operate near or at saturation conditions. In this work, we show that these goals can be achieved by exploiting “commensurate stacking”.

Commensurate stacking is much like stacking books on a bookshelf. Figure 1 shows a prototypical stacking of *o*- and *p*-xylene in a carefully chosen rectangular channel system. A MOF with channels of 0.85 nm allows the most efficient stacking of *o*-xylene. Channels of 1 nm are desirable for stacking *p*-xylene. In a 1 nm system, *p*-xylene is able to make full use of all the available pore volume and has a strong interaction, adsorbing flat on a wall while both methyl-groups interact with a sidewall. For molecules with different dimensions four effects occur: 1) “wider” molecules (like *o*- and *m*-xylene) will be able to stack less molecules per channel-length, 2) “longer” molecules (ethylbenzene) have to align obliquely and therefore also stack less molecules per channel-length, 3) “shorter” molecules (*o*- and *m*-xylene) will have a less optimal interaction with the pore structure; 4) more bulky molecules (ethylbenzene) are unable to form commensurate layers and will therefore have a lower saturation loading. The strategy we adopt in this work is to exploit

[*] A. Torres-Knoop,^[†] Prof. Dr. R. Krishna,^[†] Dr. D. Dubbeldam^[†]
Van't Hoff Institute for Molecular Sciences
University of Amsterdam
Science Park 904, 1098 XH Amsterdam (The Netherlands)
E-mail: D.Dubbeldam@uva.nl
Homepage: <http://molsim.chem.uva.nl>

[†] These authors contributed equally to this work.

[**] This work is supported by the Netherlands Research Council for Chemical Sciences (NWO/CW) through a VIDI grant (D.D.).

 Supporting information for this article (adsorption and breakthrough simulation results) is available on the WWW under <http://dx.doi.org/10.1002/anie.201402894>. Figure numbers starting with S refer to Figures in the Supporting Information.

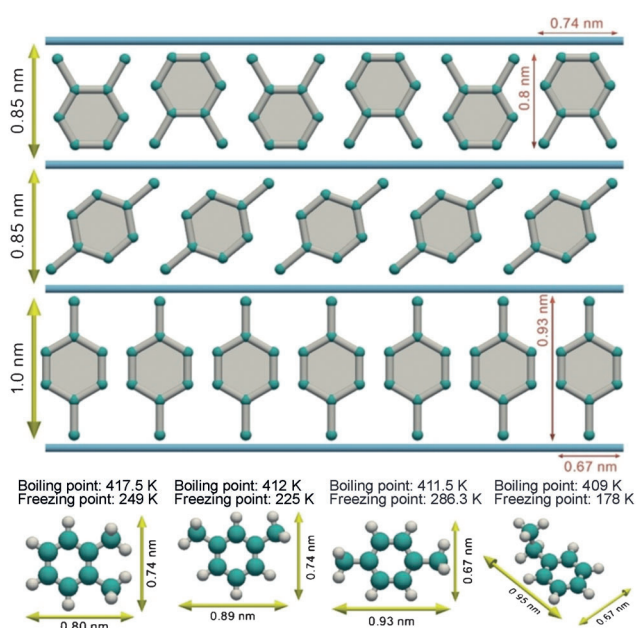


Figure 1. Schematic representation of “commensurate stacking” of xylenes in rectangular channels. The yellow arrows denote the characteristic lengths of the molecules, which have to be commensurate with the channel dimensions. Channels of about 0.85 nm in size allow an efficient stacking of *o*-xylene molecules. The same channel size forces *p*-xylene molecule to align obliquely, reducing the adsorption of *p*-xylene compared to *o*-xylene. A *p*-xylene stacking would require channel dimensions of about 1.0 nm.

differences in the stacking efficiencies of C_8 aromatic hydrocarbons within the MOF channels.

Ortho-selective structures: The adsorption of ethylbenzene as well as *o*-, *m*-, and *p*-xylenes within the one-dimensional, lozenge-shaped rhombohedral channels of MIL-47(V) of approximately 0.85 nm was considered. Adsorption within the channels of MIL-47(V) favors *o*-xylene because the molecules can most effectively stack along the channel length.^[9,10] Essentially, MIL-47(V) offers the appropriate “bookshelf” structure that is required to optimally stack *o*-xylene molecules^[8] (see Figure 2). Note that the channel dimensions of MIL-47(V) (and also of MIL-53, to be discussed next) is not large enough to allow *p*-xylene to stack vertically; these molecules align obliquely along the channel length (Figures S9a and S13a, respectively).

Breakthrough simulations for four-component *o*-xylene/*m*-xylene/*p*-xylene/ethylbenzene (Figure S11a) show the

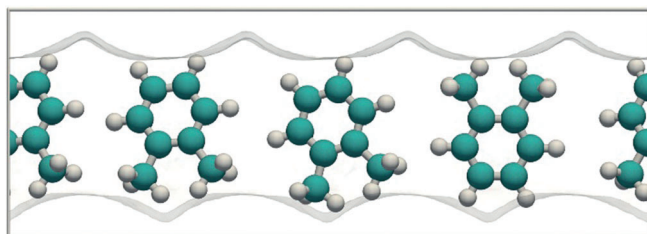


Figure 2. Snapshot of *o*-xylene in MIL-47 at 433 K. MIL-47 offers a 0.85 nm “bookshelf” which optimally stacks molecules that are commensurate with this dimension (i.e. *o*-xylene).

sequence of breakthroughs in a fixed-bed adsorber as ethylbenzene, *p*-xylene, *m*-xylene, and *o*-xylene. This is in agreement with the experimental breakthroughs reported by Finsy et al.^[11] The computed six-component breakthroughs of *o*-xylene/*m*-xylene/*p*-xylene/ethylbenzene/benzene/toluene in MIL-47 (Figure S11b) show that the presence of benzene and toluene in the fluid mixture does not alter the sequence of breakthroughs.

The framework structure of MIL-53(Al) is similar to that of MIL-47(V). The sequence of breakthroughs (Figure S15) is in qualitative agreement with experiments of Remy et al.^[12] Their work indicates that guest-induced structural changes of MIL-53(Al) also have to be considered in quantitative modeling of the breakthrough characteristics.

Fang et al.^[13] report pulse-breakthrough simulations for four-component *o*-xylene/*m*-xylene/*p*-xylene/ethylbenzene in MOF-CJ3 that clearly indicate adsorption selectivity toward *o*-xylene. MOF-CJ3 has square channels of approximately 0.8 nm size. The rationalization of *o*-xylene-selective adsorption is expected to be similar to that of MIL-47. CBMC simulations of pure component isotherms confirm that the adsorption is selective to the *ortho* isomer. Breakthrough simulations for four-component *o*-xylene/*m*-xylene/*p*-xylene/ethylbenzene in MOF-CJ3 show the hierarchy of breakthroughs to be ethylbenzene, *p*-xylene, *m*-xylene, and *o*-xylene (Figure S19). This hierarchy is not influenced by the presence of benzene and toluene in the feed mixture. For comparison with the pulse chromatographic experiments of Fang et al.,^[13] we also conducted pulse-breakthrough simulations. The pulse-chromatographic simulations (Figure S3) indicate that ethylbenzene and *p*-xylene peak at nearly the same time, in precise agreement with the experiments. The subsequent breakthroughs of *m*-xylene and *o*-xylene are in good agreement with the experimental data, albeit on a different time scale.

Nicolau et al.^[14] report experimental breakthrough data for C_8 hydrocarbons in beds packed with Zn(bdc)dabco, a framework that has two types of intersecting channels of about 0.75 nm × 0.75 nm along the x-axis. The sequence of breakthroughs of xylene isomers is *p*-xylene, *m*-xylene, and *o*-xylene.

Bárcia et al.^[15] and Moreira et al.^[16] report breakthrough data for C_8 aromatic hydrocarbons in UiO-66(Zr), a zirconium-based metal–organic framework (MOF). Its cubic rigid 3D pore structure consists of an array of octahedral cavities with 1.1 nm diameter, and tetrahedral cavities with 0.8 nm diameter. The two types of cages are connected through narrow triangular windows of approximately 0.6 nm. The sequence of experimental breakthroughs of xylene isomers is *p*-xylene, *m*-xylene, and *o*-xylene. The adsorption selectivity is in favor of *o*-xylene; this is most likely due to the more compact configuration of *o*-xylene that allows preferential location in the smaller tetrahedral cages of UiO-66. The separation performance is strongly influenced by intracrystalline diffusion considerations because of the small windows at the entrance to the cages.

All the MOFs (MIL-47(V), MIL-53(Al), MOF-CJ3, UiO-66, and Zn(bdc)dabco) discussed in the foregoing paragraph are selective for the adsorption of *o*-xylene, and less suitable

for use in industrial practice. Let us turn our attention to MOFs that have the desired selectivity towards *p*-xylene.

Para-selective structures: MIL-125(Ti) comprises of two different types of cages: larger 1.2 nm octahedral cages, and smaller tetrahedral 0.6 nm cages. Those are connected through narrow triangular windows of 0.5 nm. Amino functionalization of the benzene linker yields MIL-125(Ti)-NH₂. Due to the protrusion of the amino groups in the pore space the pore space of MIL-125(Ti)-NH₂ is slightly smaller than that in MIL-125(Ti).

The CBMC pure component isotherm for both MIL-125(Ti) and MIL-125(Ti)-NH₂, together with breakthrough simulations (Figure S23 and S27, respectively), show that these materials have selectivity towards the *para* isomer. The experimental data of Vermoortele et al.^[17] and Moreira et al.^[18,19] on breakthroughs of xylene isomers in MIL-125(Ti) and MIL-125(Ti)-NH₂, appear to confirm that these materials have the desirable selectivity towards *p*-xylene. However, the breakthrough experiments also show that the selectivity towards *p*-xylene appears to depend on the concentration of ethylbenzene in the feed stream. Indeed, for a range of feed compositions, *p*-xylene and ethylbenzene breakthrough at the same time. This indicates that both MIL-125(Ti) and MIL-124(Ti)-NH₂ are unlikely to be considered as suitable adsorbents because industrial feed mixtures invariably contain a sizable proportion of ethylbenzene.

CBMC simulation data for the adsorption of C₈ hydrocarbons in 1.0 nm square-shaped 1D channels of Co(BDP) show separation characteristics that are desirable from an industrial perspective. The channel dimension is large enough to allow the *p*-xylene molecules to align vertically. This leads to a good packing of the *para* isomer within the 1D channels. The simulations of the pure component isotherms clearly demonstrate a higher adsorption loading of *p*-xylene than any of the other C₈ hydrocarbons. Breakthrough simulations confirm that *p*-xylene is the last component to emerge from the fixed bed (Figure S31).

Jin et al.^[20] have presented isotherm data for xylene isomers in JUC-77 which is a MOF that has rhombus-shaped channels running in two perpendicular directions. The size of the channels is such as to favor only *p*-xylene that has the smallest width; this results in *para*-selectivity in separation. The simulations of pure component isotherms and breakthrough simulations (Figures S34 and S35) confirm the *para* selectivity observed in the experiments. Diffusional limitations are expected to be of paramount importance for JUC-77.

MAF-X8 possesses the right channel dimensions for the stacking of *para*-xylene to occur. MAF-X8 is a Zn^{II} pyrazolate-carboxylate framework whose synthesis has been reported by He et al.^[21] We observed a high adsorption selectivity of *p*-xylene with respect to *o*- and *m*-xylene and ethylbenzene; see mixture isotherm data in Figure 3a. The ideal adsorption solution theory (IAST) prediction of the mixture equilibrium based on the pure components is of excellent accuracy as verified by molecular simulations of mixture adsorption. The breakthrough simulations presented in Figure 3b confirm the strong *para* selectivity. The presence of benzene and toluene in the feed mixture does not seem to

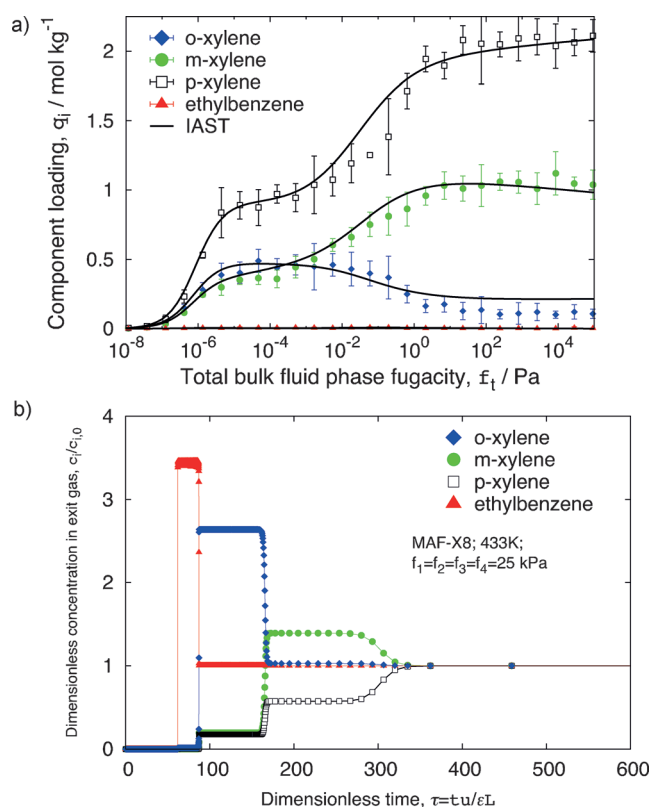


Figure 3. Xylene separation at 433 K using MAF-X8. a) Equimolar mixture isotherms and IAST prediction based on pure component isotherms. b) Simulated step breakthrough at 25 kPa partial pressure. The IAST prediction is in excellent agreement with the mixture simulations and its validation is important because IAST is the basis for the breakthrough computations. The mixture and breakthrough simulations show high *p*-xylene selectivity combined with a high *p*-xylene loading in the mixture (about 2.2 mol kg⁻¹ at 1 bar). At 433 K the bulk fluid is in the liquid phase if the total mixture fugacity is higher than about 1 MPa. Our breakthrough simulations operate at 100 kPa, and therefore are somewhat conservative with regard to separation.

influence the sharp separations that are achievable with MAF-X8 (Figure S43b). In contrast to CoBDP, MAF-X8 is commensurate with the structure in all three coordinate directions. Snapshots (Figure 4) highlight that the high selectivity is due to stacking. This raises the question: “How good is molecular stacking compared to other separation mechanisms?”

Figure 5 compares the separation characteristics of materials that are selective to *p*-xylene adsorption. We note that MAF-X8 has nearly the same adsorption selectivity as BaX, but has a significantly higher capacity to adsorb *p*-xylene. This higher capacity of MAF-X8 results in a significantly longer cycle time, which implies that less frequent regeneration will be required. All other MOFs appear to be significantly poorer in selectivity as compared to BaX and MAF-X8. The other MOFs are also lower in *p*-xylene adsorption capacity. This shows that molecular stacking is able to make (near) optimal use of the available pore volume.

Using state-of-the-art molecular simulation methodologies, we have systematically screened a wide variety of

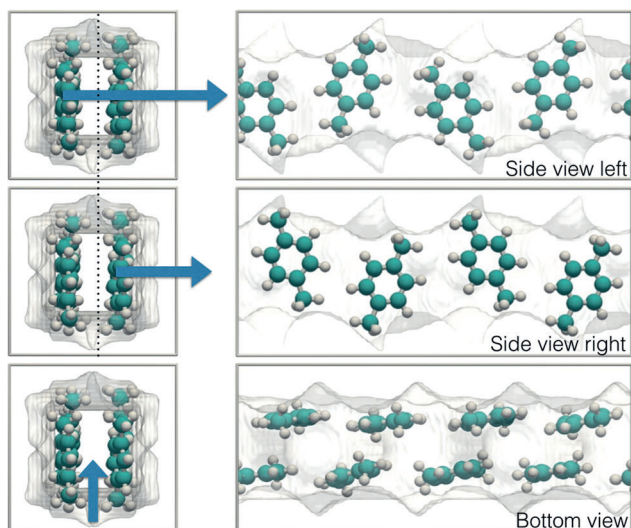


Figure 4. Stacking of *p*-xylene in the MAF-X8 structure. Note that *p*-xylene is commensurate in three directions: it fits perfectly length-wise, it forms two layers that fit snugly, and along the channel *p*-xylene stacks in an alternating fashion.

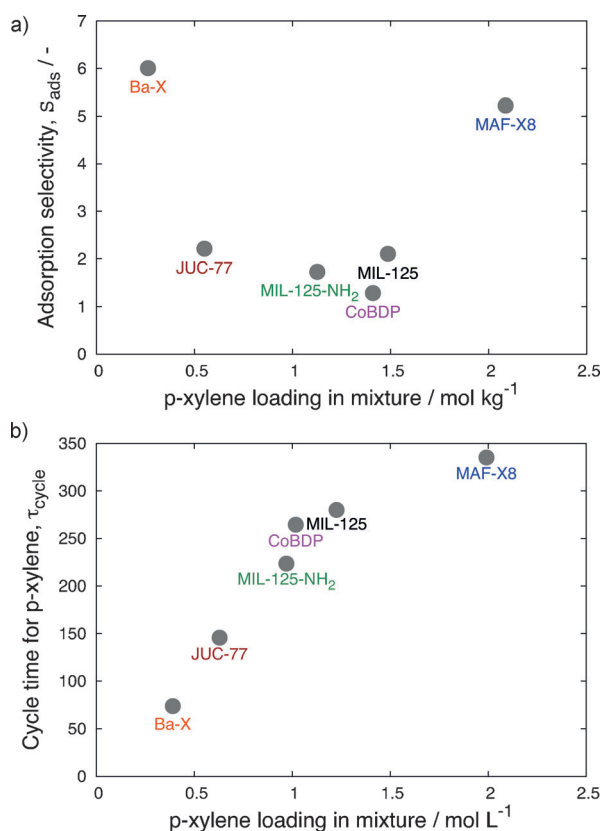


Figure 5. Comparison of *p*-xylene selective MOFs: a) Adsorption selectivity versus *p*-xylene capacity. b) Comparison of adsorption selectivity versus *p*-xylene cycle time for various MOFs. The adsorption selectivity is defined as $3q_3/(q_1+q_2+q_4)$ where 1 = *o*-xylene, 2 = *m*-xylene, 3 = *p*-xylene, and 4 = ethylbenzene. We define the cycle time for *p*-xylene as the dimensionless time, τ_{cycle} , at which the concentration of the gas at the outlet is 99% of the value at the inlet.

zeolites and metal–organic frameworks (MOFs) to investigate the possibilities of achieving separation performances that are superior to BaX. Our investigations have highlighted the crucial importance of channel dimensions on separations. MOFs such as MIL-47(V), MIL-53(Al), MOF-CJ3, UiO-66, and Zn(bdc)dabco exhibit selectivity towards *o*-xylene, a feature that is not desirable in industrial practice. On the other hand, MAF-X8, Co(BDP), MIL-125(Ti), MIL-125(Ti)-NH₂, MFI, and JUC-77 have the desirable selectivity towards *p*-xylene isomers. Of these MOFs, MAF-X8 is particularly noteworthy because the channel dimensions and geometry allow efficient and commensurate stacking of *p*-xylene molecules. Such efficient stacking results in adsorption selectivities that are comparable to that of BaX. More importantly, the *p*-xylene adsorption capacity of MAF-X8 is significantly higher than that of BaX. Consequently, the cycle times for *p*-xylene are found to be about a factor of 4.5 longer with MAF-X8 and this is expected to result in significant process improvements.

Experimental Section

The adsorption computations are performed using the configurational-bias Monte Carlo (CBMC), continuous fractional component Monte Carlo (CFCMC),^[22] and configurational-bias continuous fractional component Monte Carlo (CB/CFCMC)^[23] algorithms in the grand-canonical ensemble. The systems are modeled in full atomistic detail (all atom model) using classical force fields:^[24] OPLS for the adsorbents, DREIDING for the MOFs, and TraPPE for the zeolites.

Using the dual-site Langmuir–Freundlich fits of the pure component isotherms, breakthrough calculations were carried out by solving a set of partial differential equations for each of the species in the gas mixture.^[25]

Received: March 3, 2014

Revised: April 9, 2014

Published online: June 10, 2014

Keywords: adsorption · stacking interactions · MOFs · selective separation · xylenes

- [1] E. W. Flick in *Industrial solvent handbook*, 5th ed., Noyes Data Corporation, Westwood, **1998**.
- [2] J. Scheirs, T. E. Long in *Industrial Modern Polyesters: chemistry and technology of polyesters and copolyesters*, Wiley, Chichester, **2003**.
- [3] J. Vicens, A. E. Armah, S. Fujii, K.-I. Tomita, *J. Inclusion Phenom. Macrocyclic Chem.* **1991**, *10*, 159–163.
- [4] D. Peralta, K. Barthelet, J. Pérez-Pellitero, C. Chizallet, G. Chaplais, A. Simon-Masseron, G. D. Pirngruber, *J. Phys. Chem. C* **2012**, *116*, 21844–21855; K. A. O. Santos, A. A. Dantas Neto, M. C. P. A. Moura, T. N. Castro Dantas, *Braz. J. Petroleum Gas* **2011**, *5*, 255–268.
- [5] R. Q. Snurr, A. T. Bell, D. N. Theodorou, *J. Phys. Chem.* **1993**, *97*, 13742–13752.
- [6] “Molecular simulation studies of gas adsorption and separation in metal–organic frameworks”: P. Z. Moghadam, PhD thesis, University of Edinburgh, **2012**.
- [7] M. Minceva, A. E. Rodrigues, *Chem. Eng. Res. Des.* **2004**, *82*, 667–681.
- [8] M. Minceva, P. S. Gomes, V. Meshko, A. E. Rodrigues, *Chem. Eng. J.* **2008**, *140*, 305–323.

- [9] R. Krishna, *Microporous Mesoporous Mater.* **2014**, *185*, 30–50.
- [10] J. M. Castillo, T. J. H. Vlught, S. Calero, *J. Phys. Chem. C* **2009**, *113*, 20869–20874.
- [11] V. Finsy, H. Verelst, L. Alaerts, D. De Vos, P. A. Jacobs, G. V. Baron, J. F. M. Denayer, *J. Am. Chem. Soc.* **2008**, *130*, 7110–7118.
- [12] T. Remy, G. V. Baron, J. F. M. Denayer, *Langmuir* **2011**, *27*, 13064–13071.
- [13] L. Z. Fang, S. R. Zheng, J. B. Tan, S. L. Cai, J. Fan, X. Yan, W. G. Zhang, *J. Chromatogr. A* **2013**, *1285*, 132–138.
- [14] M. P. M. Nicolau, P. S. Barcia, J. M. Gallegos, J. A. C. Silva, A. E. Rodrigues, B. Chen, *J. Phys. Chem. C* **2009**, *113*, 13173–13179.
- [15] P. S. Barcia, D. Guimaraes, P. A. P. Mendes, J. A. C. Silva, V. Guillermin, H. Chevreau, C. Serre, A. E. Rodrigues, *Microporous Mesoporous Mater.* **2011**, *139*, 67–73.
- [16] M. A. Moreira, J. C. Santos, A. F. P. Ferreira, J. Loureiro, F. Ragon, P. Horcajada, K. E. Shim, Y. K. Hwang, U. H. Lee, J. S. Chang, C. Serre, A. E. Rodrigues, *Langmuir* **2012**, *28*, 5715–5723.
- [17] F. Vermoortele, M. Maes, P. Z. Moghadam, M. J. Lennox, F. Ragon, M. Boulhout, S. Biswas, K. G. M. Laurier, I. Beurroies, R. Denoyel, M. Roeffaers, N. Stock, T. Duren, C. Serre, D. E. De Vos, *J. Am. Chem. Soc.* **2011**, *133*, 18526–18529.
- [18] M. A. Moreira, J. C. Santos, A. F. P. Ferreira, J. Loureiro, F. Ragon, P. Horcajada, P. G. Yot, C. Serre, A. E. Rodrigues, *Langmuir* **2012**, *28*, 3494–3502.
- [19] M. A. Moreira, J. C. Santos, A. F. P. Ferreira, J. Loureiro, F. Ragon, P. Horcajada, P. G. Yot, C. Serre, A. E. Rodrigues, *Microporous Mesoporous Mater.* **2012**, *158*, 229–234.
- [20] Z. Jin, H. Y. Zhao, X. J. Zhao, Q. R. Fang, J. R. Long, G. S. Zhu, *Chem. Commun.* **2010**, *46*, 8612–8614.
- [21] C. T. He, J. Y. Tian, S. Y. Liu, G. Ouyang, J. P. Zhang, M. Chen, *Chem. Sci.* **2013**, *4*, 351–356.
- [22] W. Shi, E. J. Maginn, *J. Chem. Theory Comput.* **2007**, *3*, 1451–1463.
- [23] A. Torres-Knoop, S. P. Balaji, T. Vlught, D. Dubbeldam, *J. Chem. Theory Comput.* **2014**, *10*, 942–952.
- [24] W. L. Jorgensen, D. S. Maxwell, J. Tirado-Rives, *J. Am. Chem. Soc.* **1996**, *118*, 11225–11236; S. L. Mayo, B. D. Olafson, W. A. Goddard, *J. Phys. Chem.* **1990**, *94*, 8897–8909; P. Bai, M. Tsapatsis, J. I. Siepmann, *J. Phys. Chem. C* **2013**, *117*, 24375–24387.
- [25] R. Krishna, J. R. Long, *J. Phys. Chem. C* **2011**, *115*, 12941–12950.

Supporting Information

© Wiley-VCH 2014

69451 Weinheim, Germany

Separating Xylene Isomers by Commensurate Stacking of *p*-Xylene within Channels of MAF-X8**

*Ariana Torres-Knoop, Rajamani Krishna, and David Dubbeldam**

ange_201402894_sm_miscellaneous_information.pdf

Nomenclature

Notation

$b_{i,A}$	dual-Langmuir-Freundlich constant for species i at adsorption site A , $\text{Pa}^{-\nu_i}$
$b_{i,B}$	dual-Langmuir-Freundlich constant for species i at adsorption site B , $\text{Pa}^{-\nu_i}$
c_i	molar concentration of species i in the gas mixture, mol m^{-3}
c_{i0}	molar concentration of species i in the gas mixture at inlet of adsorber, mol m^{-3}
\mathcal{D}_i	Maxwell-Stefan diffusivity, $\text{m}^2 \text{s}^{-1}$
f_i	partial fugacity in the bulk fluid phase of species i in mixture, Pa
f_t	total fugacity in the bulk fluid phase of species i in mixture, Pa
L	length of packed bed adsorber, m
n	number of species in the mixture, dimensionless
N_i	molar flux of species i , $\text{mol m}^{-2} \text{s}^{-1}$
p_i	partial pressure in the bulk fluid phase of species i in mixture, Pa
p_t	total system pressure, Pa
q_i	component molar loading of species i , mol kg^{-1}
$q_{i,\text{sat}}$	component molar loading of species i at saturation, mol kg^{-1}
q_t	total molar loading in mixture, mol kg^{-1}
$q_{\text{sat},A}$	saturation loading of site A , mol kg^{-1}
$q_{\text{sat},B}$	saturation loading of site B , mol kg^{-1}
$\bar{q}_i(t)$	<i>spatially averaged</i> component molar loading of species i , mol kg^{-1}
r_c	radius of crystallite, m
R	gas constant, $8.314464919 \text{ J mol}^{-1} \text{ K}^{-1}$
t	time, s
T	absolute temperature, K
u	superficial gas velocity in packed bed, m s^{-1}
v	interstitial gas velocity in packed bed, m s^{-1}
x_i	mole fraction of species i in adsorbed phase, dimensionless
y_i	mole fraction of component i in bulk vapor phase, dimensionless
V_p	pore volume, $\text{m}^3 \text{ kg}^{-1}$
a, b, c	unit cell lengths, \AA
\mathcal{H}	transformation matrix from fractional space to Cartesian space.

Greek letters

ε	voidage of packed bed, dimensionless
μ_i	molar chemical potential, J mol ⁻¹
Θ_i	loading of species i , molecules per unit cell
$\Theta_{i,\text{sat}}$	saturation loading of species i , molecules per unit cell
$\Theta_{t,\text{sat}}$	total molar loading of mixture, molecules per unit cell
ν	exponent in dual-Langmuir-Freundlich isotherm, dimensionless
ρ	framework density, kg m ⁻³
τ	time, dimensionless
τ_{cycle}	time at which the concentration of the gas at the outlet is 99% of the value at the inlet, dimensionless
θ	bend angle between atoms, degrees
ϕ	dihedral angle between atoms, degrees
α	unit cell angle between b and c, degrees
β	unit cell angle between a and c, degrees
γ	unit cell angle between a and b, degrees
ε	the Lennard-Jones strength parameter, $k_B T$
σ	the Lennard-Jones size parameter, Å

Subscripts

i	referring to component i
A	referring to site A
B	referring to site B
t	referring to the total mixture

Contents

1. Simulation Methodology for Transient Breakthrough	S6
1.1. Fitting of pure component CBMC isotherms	S6
1.2. Simulation methodology for transient breakthrough in fixed bed adsorbers	S6
1.3. Validation	S10
2. Simulation Methodology for Computing Adsorption	S11
2.1. Force field	S11
2.2. Adsorbate model	S11
2.3. Framework model	S13
2.4. Monte Carlo simulations	S14
2.5. Computing adsorption isotherms	S15
2.6. Configurational-Bias Monte Carlo	S16
2.7. Continuous Fractional Monte Carlo	S16
2.8. Monte Carlo moves for thermalization	S18
3. BaX	S20
4. Short-list of Potential Adsorbents	S21
4.1. MIL-47(V)	S22
4.1.1. Energy landscapes	S22
4.1.2. Stacking of o-xylene in MIL-47	S23
4.1.3. Snapshots	S24
4.1.4. Langmuir-Freundlich parameters	S25
4.1.5. Adsorption isotherms	S25
4.1.6. Breakthrough simulations	S25
4.2. MIL-53(Al)	S26
4.2.1. Energy landscapes	S26
4.2.2. Snapshots	S27
4.2.3. Langmuir-Freundlich parameters	S28
4.2.4. Adsorption isotherms	S28
4.2.5. Breakthrough simulations	S28
4.3. MOF-CJ3	S29
4.3.1. Energy landscapes	S29
4.3.2. Snapshots	S30
4.3.3. Langmuir-Freundlich parameters	S31
4.3.4. Adsorption isotherms	S31
4.3.5. Breakthrough simulations	S31
4.4. MIL-125(Ti)	S32
4.4.1. Energy landscapes	S32
4.4.2. Snapshots	S33
4.4.3. Langmuir-Freundlich parameters	S34
4.4.4. Adsorption isotherms	S34
4.5. MIL-125(Ti)-NH ₂	S35
4.5.1. Energy landscapes	S35
4.5.2. Snapshots	S36
4.5.3. Langmuir-Freundlich parameters	S37

4.5.4. Adsorption isotherms	S37
4.6. CoBDP	S38
4.6.1. Energy landscapes	S38
4.6.2. Snapshots	S39
4.6.3. Langmuir-Freundlich parameters	S40
4.6.4. Adsorption isotherms	S40
4.6.5. Breakthrough simulations	S40
4.7. JUC-77	S41
4.7.1. Energy landscapes	S41
4.7.2. Snapshots	S42
4.7.3. Langmuir-Freundlich parameters	S43
4.7.4. Adsorption isotherms	S43
4.8. MAF-X8	S44
4.8.1. Energy landscapes	S44
4.8.2. Stacking of p-xylene in MAF-X8	S45
4.8.3. Stacking of p-xylene in MAF-X8: schematic snapshots	S46
4.8.4. Snapshots at low loading	S47
4.8.5. Snapshots at saturation loading	S48
4.8.6. Langmuir-Freundlich parameters	S49
4.8.7. Adsorption isotherms	S49
4.8.8. Breakthrough simulations	S49
5. Influence of saturation capacities on separations in fixed bed adsorbers	S50
6. Comparison of p-Selective Adsorbents	S52
7. Screening of Potential Zeolite Adsorbents	S54
7.1. BEA	S55
7.2. DON	S56
7.3. EMT	S57
7.4. FAU-Si	S58
7.5. LTL	S59
7.6. MFI-ortho (Olson)	S60
7.7. MFI-ortho (Van Koningsveld)	S61
7.8. MFI-mono	S62
7.9. MFI-para	S63
7.10. MOR	S64
7.11. MRE	S65
7.12. MTW	S66
8. Screening of Potential MOF Adsorbents	S67
8.1. IRMOF-1	S68
8.2. CoBDP	S69
8.3. CoDOBDC	S70
8.4. MAF-X8	S71
8.5. JUC-77	S72
8.6. NiDOBDC	S73
8.7. PAF-2	S74
8.8. UiO-66	S75
8.9. ZnDOBDC	S76
8.10. MIL-125	S77
8.11. MIL-125-NH ₂	S78
8.12. MIL-47	S79
8.13. MIL-53	S80
8.14. MOF-CJ3	S81

Simulation Methodology for Transient Breakthrough

1.1 Fitting of pure component CBMC isotherms

For IAST calculations of component loadings in 4-component o-xylene(1)/m-xylene(2)/p-xylene(3)/ethylbenzene(4) and 6-component o-xylene(1)/m-xylene(2)/p-xylene(3)/ethylbenzene(4)/benzene(5)/toluene(6) mixtures of C8 hydrocarbons, the unary isotherm data on the absolute component loadings, of o-xylene(1)/m-xylene(2)/p-xylene(3)/ethylbenzene(4)/benzene(5)/toluene(6) were fitted with the dual-site Langmuir-Freundlich model:

$$q_i = q_{i,A,\text{sat}} \frac{b_{i,A} f_i^{v_{i,A}}}{1 + b_{i,A} f_i^{v_{i,A}}} + q_{i,B,\text{sat}} \frac{b_{i,B} f_i^{v_{i,B}}}{1 + b_{i,B} f_i^{v_{i,B}}} \quad (1.1)$$

The saturation capacities $q_{i,\text{sat}}$, Langmuir constants b_i , for the two sites, A , and B , are provided in Tables [S4](#), [S5](#), [S6](#), [S7](#), [S8](#), [S9](#), [S10](#), [S11](#), for various MOFs discussed in this article.

1.2 Simulation methodology for transient breakthrough in fixed bed adsorbers

Fixed bed, packed with crystals of nanoporous materials, are commonly used for separation of mixtures (see schematic in Figure [S1](#)); such adsorbers are commonly operated in a transient mode, and the compositions of the gas phase, and within the crystals, vary with position and time. Experimental data on the transient breakthrough of mixtures across fixed beds are commonly used to evaluate and compare the separation performance of zeolites and MOFs [[1](#), [2](#), [3](#), [4](#)]. For a given separation task, transient breakthroughs provide a more realistic evaluation of the efficacy of a material, as they reflect the combined influence of adsorption selectivity, and adsorption capacity [[4](#), [5](#)].

Furthermore, transient breakthroughs are influenced by both mixture adsorption equilibrium, and intra-crystalline diffusion. In order to determine the extent of the relative importance of adsorption and diffusion in determining the separation performance we perform transient breakthrough simulations, and compare these with experimental data. We describe below the simulation methodology used to perform transient breakthrough calculations.

Assuming plug flow of an n -component gas mixture through a fixed bed maintained under isothermal conditions, the partial pressures in the gas phase at any position and instant of time are obtained by solving

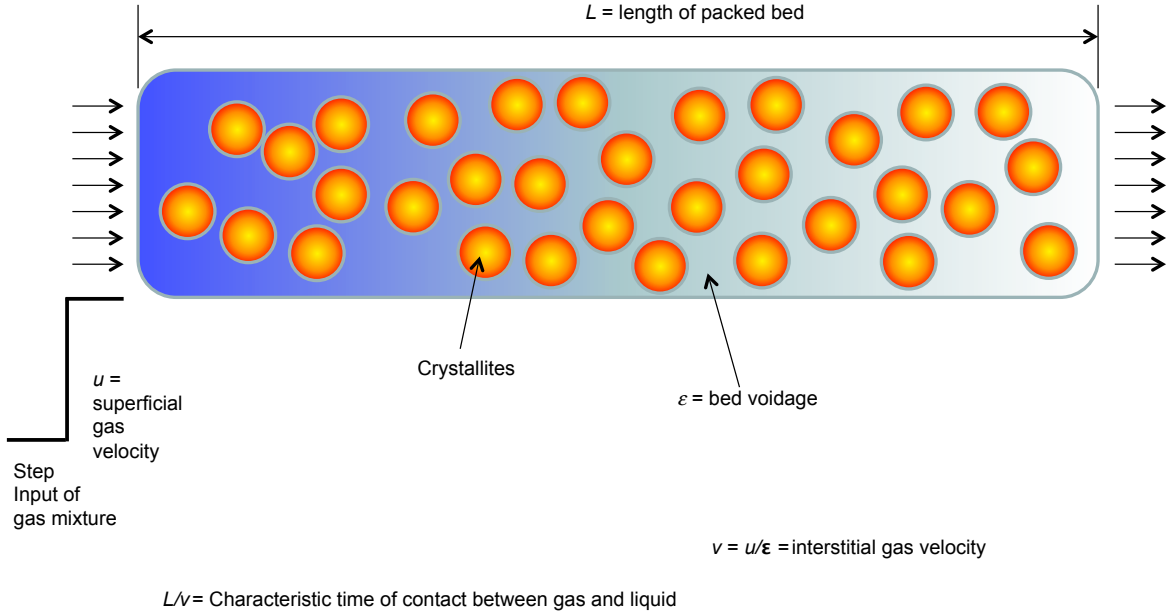


Figure S1: Schematic of packed bed adsorber.

the following set of partial differential equations for each of the species i in the gas mixture [6]

$$\frac{1}{RT} \frac{\partial p_i(t,z)}{\partial t} = -\frac{1}{RT} \frac{\partial (v(t,z) p_i(t,z))}{\partial z} - \frac{(1-\varepsilon)}{\varepsilon} \rho \frac{\partial \bar{q}_i(t,z)}{\partial t}; \quad i = 1, 2, \dots, n \quad (1.2)$$

In equation 1.2, t is the time, z is the distance along the adsorber, ρ is the framework density, ε is the bed voidage, v is the interstitial gas velocity, and $\bar{q}_i(t,z)$ is the spatially averaged molar loading within the crystallites of radius r_c , monitored at position z , and at time t .

At any time t , during the transient approach to thermodynamic equilibrium, the spatially averaged molar loading within the crystallite r_c is obtained by integration of the radial loading profile

$$\bar{q}_i(t) = \frac{3}{r_c^3} \int_0^{r_c} \bar{q}_i(r,t) r^2 dr \quad (1.3)$$

For transient unary uptake within a crystal at any position and time with the fixed bed, the radial distribution of molar loadings, q_i , within a spherical crystallite, of radius r_c , is obtained from a solution of a set of differential equations describing the uptake

$$\frac{\partial q_i(r,t)}{\partial t} = -\frac{1}{\rho} \frac{1}{r^2} \frac{\partial (r^2 N_i)}{\partial r} \quad (1.4)$$

in which both correlation effects and thermodynamic coupling effects are considered to be of negligible importance

$$N_i = -\rho \mathcal{D}_i \frac{\partial q_i}{\partial r} \quad (1.5)$$

Summing equation 1.3 over all n species in the mixture allows calculation of the *total average* molar loading of the mixture within the crystallite

$$\bar{q}_t(t,z) = \sum_{i=1}^n \bar{q}_i(t,z) \quad (1.6)$$

The *interstitial* gas velocity is related to the *superficial* gas velocity by

$$v = \frac{u}{\varepsilon} \quad (1.7)$$

In industrial practice, the most common operation is to use a step-wise input of mixtures to be separated into an adsorber bed that is initially free of adsorbates, i.e. we have the initial condition

$$t = 0; \quad q_i(0, z) = 0 \quad (1.8)$$

At time, $t = 0$, the inlet to the adsorber, $z = 0$, is subjected to a step input of the n -component gas mixture and this step input is maintained till the end of the adsorption cycle when steady-state conditions are reached

$$t \geq 0; \quad p_i(0, t) = p_{i0}; \quad u(0, t) = u_0 \quad (1.9)$$

where u_0 is the superficial gas velocity at the inlet to the adsorber.

Besides, the breakthrough simulations with a step-input (equation 1.9), we also carried out simulations for a packed bed adsorber with injection of a short duration pulse of the mixture to be separated. This type of simulation is particularly useful to demonstrate the fractionating capability of adsorbents. For simulation of pulse chromatographic separations, we use the corresponding set of inlet conditions

$$0 \leq t \leq t_0; \quad p_i(0, t) = p_{i0}; \quad u(0, t) = u_0 \quad (1.10)$$

where the time for duration of the pulse is t_0 .

The breakthrough characteristics for any component are essentially dictated by two sets of parameters:

1. The characteristic contact time $\frac{L}{v} = \frac{L\varepsilon}{u}$ between the crystallites and the surrounding fluid phase, and
2. $\frac{\mathcal{D}_i}{r_c^2}$ that reflect the importance of intra-crystalline diffusion limitations.

It is common to use the dimensionless time, $\tau = \frac{tu}{L\varepsilon}$, obtained by dividing the actual time, t , by the characteristic time, $\frac{L\varepsilon}{u}$ when plotting simulated breakthrough curves [5].

For all breakthrough simulations reported here we use the parameter values: $L = 0.3$ m; voidage of bed, $\varepsilon = 0.4$; interstitial gas velocity, $v = 0.1$ m/s; superficial gas velocity, $u = 0.04$ m/s. In pulse chromatographic simulations we take the pulse duration $t_0 = 10$ s. When matching experimental data on breakthroughs, the parameter values used correspond to those relevant to the experiments being simulated. Further details of the numerical procedures used in this work, are provided by Krishna and co-workers [6, 7, 8, 9].

There are essentially two different scenarios to quantify the influence of intra-crystalline diffusion effects on breakthroughs. If the value of $\frac{\mathcal{D}_i}{r_c^2}$ is large enough to ensure that intra-crystalline gradients are absent then the entire crystallite particle can be considered to be in thermodynamic equilibrium with the surrounding bulk gas phase at that time t and position z of the adsorber

$$\bar{q}_i(t, z) = q_i(t, z) \quad (1.11)$$

The molar loadings at the outer surface of the crystallites, i.e. at $r = r_c$, are calculated on the basis of adsorption equilibrium with the bulk gas phase partial pressures p_i at that position z and time t . The adsorption equilibrium can be calculated on the basis of the Ideal Adsorption Solution Theory (IAST). This scenario is the one that is commonly adopted for screening different nanoporous materials for a given separation task [5, 9, 10, 11]. A summary of the equations describing the packed bed adsorber is given in Figure S2.

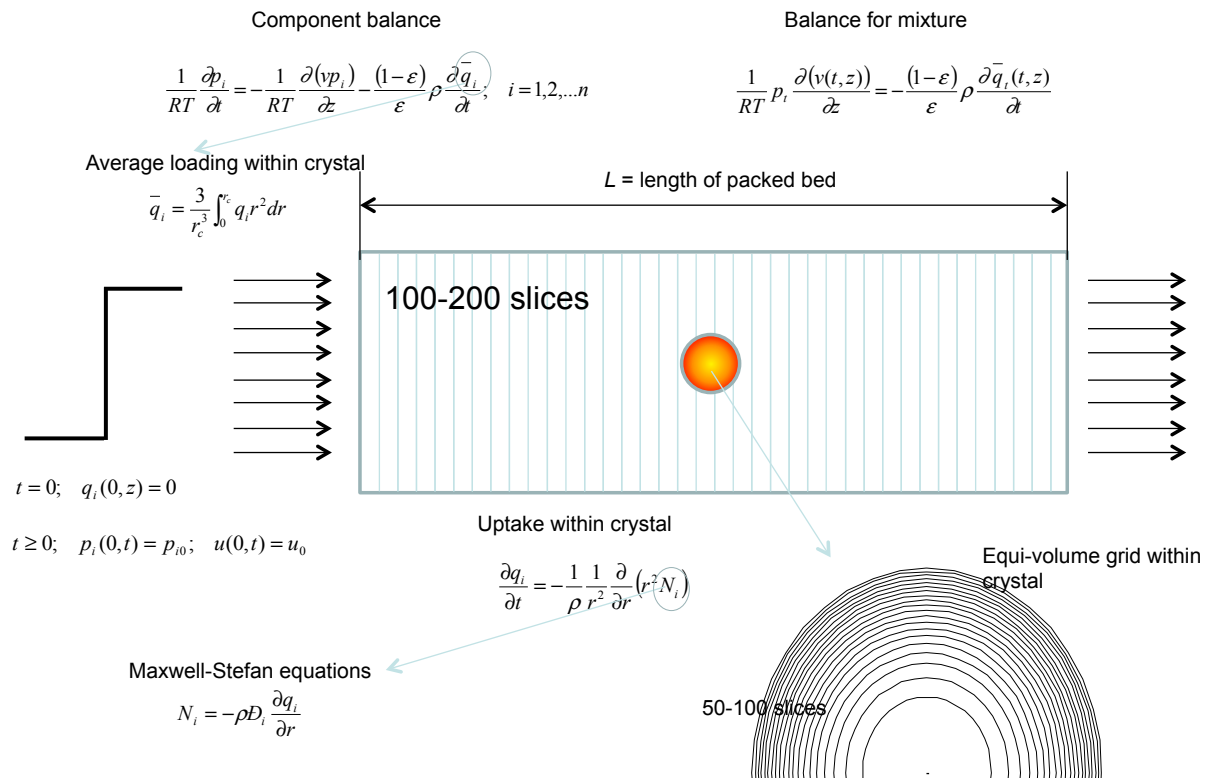


Figure S2: Summary of model equations describing packed bed adsorber, along with discretization scheme.

1.3 Validation

Fang et al.[12] report pulse breakthrough simulations for 4-component o-xylene/m-xylene/p-xylene/ethylbenzene in MOF-CJ3 that clearly indicate adsorption selectivity towards o-xylene; see Figure S3a. MOF-CJ3 has square channels of approximately 8 Å size. The rationalization of o-xylene selective adsorption is expected to be similar to that of MIL-47. CBMC simulations of pure component isotherms confirm that the adsorption is selective to the ortho isomer; see Figure S18. For comparison with the pulse chromatographic experiments of Fang et al. [12], we conducted pulse breakthrough simulations, shown in Figure S3b. The pulse chromatographic simulations indicate that ethylbenzene and p-xylene peak at nearly the same time, in precise agreement with the experiments of Fang et al. [12]. The subsequent breakthroughs of m-xylene and o-xylene are in good agreement with the experimental data, albeit on a different time scale.

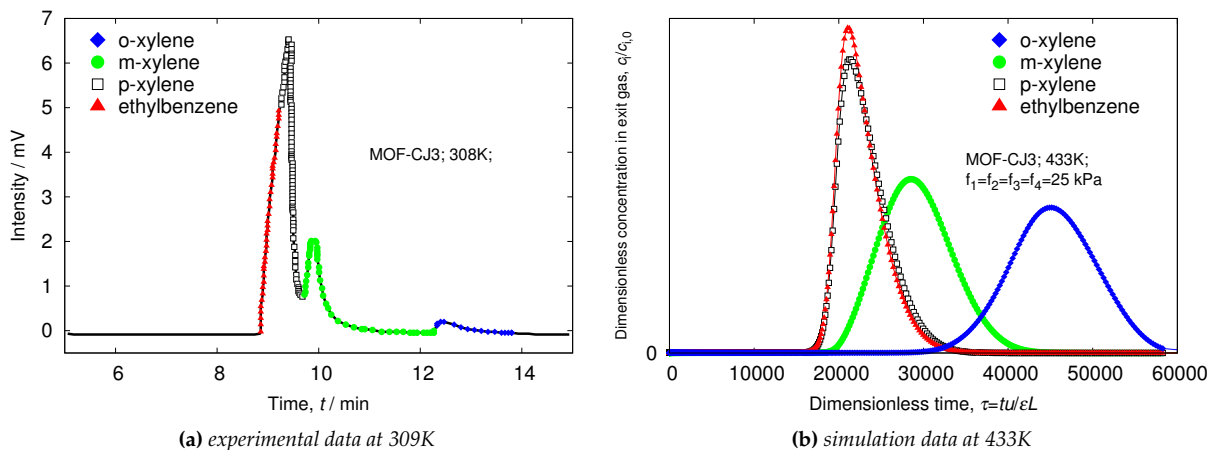


Figure S3: Simulated pulse-type breakthrough of ethylbenzene and xylene isomers for MOF-CJ3 compared to experiments of Fang et al.[12] (gas chromatograms of MOF-CJ3 coated capillary [10 m long \times 0.32 mm i.d.]). Plotted data are scanned from the article. The colors in the experimental data are a guide to the eye to compare to the simulation data.

2

Simulation Methodology for Computing Adsorption

2.1 Force field

The molecular energy can be described as an Taylor expansion in bonds, bends, torsions, etc.

$$\begin{aligned} U = & \sum_{\text{bonds}} U_r(r) + \sum_{\text{bends}} U_\theta(\theta) + \sum_{\text{torsions}} U_\phi(\phi) + \sum_{\text{out-of-plane bends}} U_\chi(\chi) + \sum_{\text{non-bonded}} U_{nb}(r) \\ & + \sum_{\text{bond-bond}} U_{bb'}(r, r') + \sum_{\text{bond-bend}} U_{b\theta'}(r, \theta) + \sum_{\text{bend-bend}} U_{\theta\theta'}(\theta, \theta') \\ & + \sum_{\text{bond-torsion}} U_{r\phi}(r, \phi, r') + \sum_{\text{bend-torsion}} U_{\theta\phi}(\theta, \phi, \theta') + \dots \end{aligned} \quad (2.1)$$

This expansion is believed to capture all the chemical entities we can think of, such as atoms, bonds, angles, etc, and physical properties like equilibrium structures, vibrational spectra, etc. The cross terms are not ad-hoc functions, but arise naturally from this expansion. For example, bonds and bends interact, as the bend angle becomes smaller the bond lengths tend to increase. Their inclusion leads to two advantages: 1) they increase the accuracy of the force field (especially the vibrational frequencies), and 2) they increase the transferability of the diagonal terms $U_r(r)$, $U_\theta(\theta)$, $U_\phi(\phi)$, $U_\chi(\chi)$. On top of the terms in Eq. 2.1 one can add ad hoc terms, such as hydrogen bonding, that are not adequately accounted for otherwise.

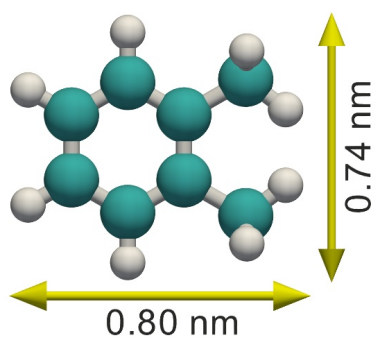
Eq. 2.1 is historically referred to as an *force field*. The name arose from the lowest order approximation using only springs with *force constants*. Force fields have matured and have become quite accurate and many parameters exist for a wide range of structures. These parameters are crucial and determine the quality of the force field.

For more details on molecular simulations in general we refer to: “Statistical Mechanics: Theory and Molecular Simulations” by M. Tuckerman [13], “Computer Simulations of Liquids” by M.P. Allen and D.J. Tildesley [14], “Understanding Molecular Simulations: from Algorithms to Applications” by D. Frenkel and B. Smit [15], “The Art of Molecular Dynamics Simulation” by D.C. Rapaport [16], and “Molecular Modeling: Principles and Applications” by A. Leach [17].

2.2 Adsorbate model

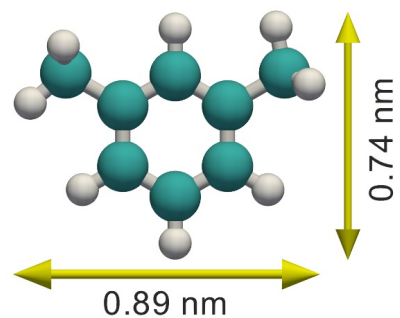
Xylenes, benzene and toluene were modeled using the all-atom OPLS force field for organic liquids [19]. The adsorbates are described as multisite rigid molecules with properties and configurations shown in Figs. S4 and S5. The interactions between xylene-xylene isomers and xylene-framework consist of Lennard-Jones and electrostatic interactions. The parameters are listed in Table S1. Cross-interactions with other

Boiling point: 417.5 K
Freezing point: 249 K



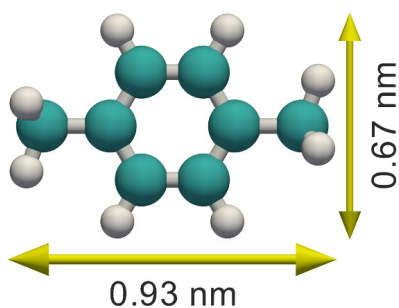
(a) *o*-xylene

Boiling point: 412 K
Freezing point: 225 K



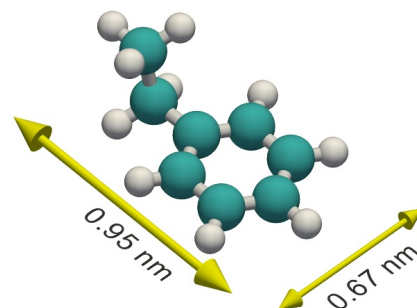
(b) *m*-xylene

Boiling point: 411.5 K
Freezing point: 286.3 K



(c) *p*-xylene

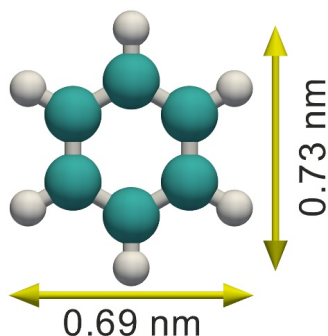
Boiling point: 409 K
Freezing point: 178 K



(d) ethylbenzene (non-planar)

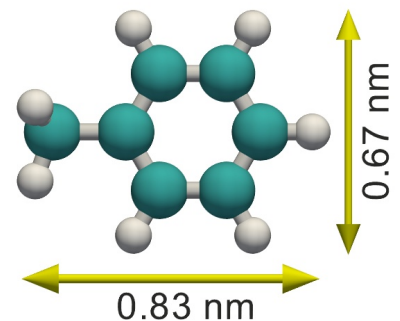
Figure S4: Xylenes are a family of C₈ aromatic hydrocarbons obtained from petroleum and generally produced as a mixture of all three isomers: *ortho*-, *meta*- and *para*-, with methyl groups attached to the aromatic ring in positions 1-2, 1-3, 1-4 respectively, and ethylbenzene. The differences in boiling points are small. There are, however, significant differences in the freezing points that allow fractional crystallization to be used for separations. The differences in the freezing points arise because of differences in the stacking efficiencies of molecules.

Boiling point: 353.3 K
Freezing point: 278.7 K



(a) benzene

Boiling point: 384 K
Freezing point: 178 K



(b) toluene

Figure S5: The other two components of BTX: benzene and toluene. The acronym BTX refers to mixtures of benzene, toluene, and the three xylene isomers. If ethylbenzene is included, the mixture is often referred to as BTEX. In this work we have included benzene and toluene in the simulations to verify that their presence in the fluid mixture does not alter the sequence of breakthroughs.

type	ϵ/k_B [K]	σ [Å]	q [e]
C, benzene	35.2254	3.55	-0.115
H, benzene	15.0966	2.42	0.115
C, CH ₃ of toluene	33.2125	3.50	-0.065
C, CH ₂ of ethylbenzene	33.2125	3.50	-0.005
C, RCH ₃	33.2125	3.50	-0.180
H, RH, alkanes	15.0966	2.50	0.060

Table S1: Force field VDW parameters for the adsorbates.

molecule	L_x [Å]	L_y [Å]	L_z [Å]
o-xylene	7.95	7.36	4.18
m-xylene	8.85	7.40	4.16
p-xylene	9.25	6.70	4.16
ethylbenzene	9.51	6.71	4.86
benzene	6.87	7.34	3.40
toluene	8.31	6.70	4.16

Table S2: Molecular shadow distances [18].

molecules and the framework are computed using Lorentz-Berthelot mixing rules. Table S2 shows typical lengths, widths, and heights of the modeled adsorbates. Distances are “molecular shadow lengths” [18] from Materials Studio [20] calculated by projecting the molecular surface on three mutually perpendicular planes. The molecules are first rotated to align the principal moments of inertia with the X, Y and Z axes (i.e. the distances depend on the conformation, but also on the orientation of the molecule).

2.3 Framework model

The framework is modeled as rigid with atom positions taken from crystallographic experimental data. Most MOFs were further optimized using VASP (PBE, precision=high) with the cell fixed to the experimentally determined unit cell size and shape. The fixed framework approximation is very common because lattice flexibility is not important for small alkanes in all-silica zeolites [21] and also for MOFs little influence of flexibility on adsorption and diffusion has been found [22]¹. Periodic boundary conditions are commonly applied to overcome the problems of surface effects. The original simulation box, including all the atoms within it, is replicated throughout space. When a molecule in the original box moves, its periodic images in each of the surrounding boxes moves in exactly the same way. If a molecule leaves the central box, one of its images will enter the box through the opposite face. It is not necessary to store the coordinates and momenta of all the images, only the ones in the central box are needed, because the images can be obtained from translation operators. Usually, one imposes the minimum-image convention: the distance between two particles is taken to be the shortest distance between their periodic images. The boundary of the periodic box does not have any physical significance, only the shape and orientation.

In crystallography, the crystal structure is defined by the unit cell (cell lengths a, b, c and angles α, β, γ), and by the fractional coordinates of the atoms within the unit cell. These coordinates form an orthonormal dimensionless \mathcal{S} -space. The transformation from \mathcal{S} -space to real \mathcal{R} -space can be carried out by the matrix \mathcal{H} :

$$\mathcal{H} = \begin{pmatrix} a & b \cos(\gamma) & c \cos(\beta) \\ 0 & b \sin(\gamma) & c\zeta \\ 0 & 0 & c\sqrt{1 - \cos^2\beta - \zeta^2} \end{pmatrix} \quad (2.2)$$

with

$$\zeta = \frac{\cos\alpha - \cos\gamma \cos\beta}{\sin\gamma} \quad (2.3)$$

Conversely, \mathcal{H}^{-1} transforms real coordinates to fractional coordinates. With the chosen \mathcal{H} the scaled box has a length of 1. Our potential forcefield is defined in real space, therefore it is convenient to store position in \mathcal{R} space, transform them to \mathcal{S} space, apply periodic boundary conditions in \mathcal{S} space, and transform back to \mathcal{R} space to compute distances within the simulation box

$$\begin{aligned} \mathbf{s} &= \mathcal{H}^{-1} \mathbf{r} \\ \mathbf{s}' &= \mathbf{s} - \text{rint}(\mathbf{s}) \\ \mathbf{r}' &= \mathcal{H} \mathbf{s}' \end{aligned} \quad (2.4)$$

¹Known exceptions are structures that transform under loading or as a function of temperature, e.g. MIL-53(Cr).

type	ϵ/k_B [K]	σ [Å]	type	ϵ/k_B [K]	σ [Å]	type	ϵ/k_B [K]	σ [Å]
O	48.1581	3.03315	N	38.9492	3.26256	C	47.8562	3.47299
F	36.4834	3.0932	B	47.8058	3.58141	P	161.03	3.69723
S	173.107	3.59032	Cl	142.562	3.51932	Br	186.191	3.51905
H	7.64893	2.84642	Zn	62.3992	2.46155	Be	42.7736	2.44552
Cr	7.54829	2.69319	Fe	6.54185	2.5943	Mn	6.54185	2.63795
Cu	2.5161	3.11369	Co	7.04507	2.55866	Ga	208.836	3.90481
Ti	8.55473	2.8286	Sc	9.56117	2.93551	V	8.05151	2.80099
Ni	7.54829	2.52481	Zr	34.7221	2.78317	Mg	55.8574	2.69141
Ne	21.1352	2.88918	Ag	18.1159	2.80455	Te	200.281	3.98232
Cd	114.734	2.53728	Sb	225.946	3.93777	Si*	22	2.3
Al	155.998	3.91105	Si	155.998	3.80414	O*	53	3.30

Table S3: Framework force field VDW parameters. Charges for the frameworks are computed using the REPEAT [23] methodology on primitive unit cells for each structure. Values denoted with a * correspond to the TraPPE zeolite force field.

where the “rint”-function returns the rounded integer value of its argument. The smallest perpendicular width of the unit cell has to be larger than twice the spherical cutoff in \mathcal{R} space to be consistent with the minimum image convention.

The DREIDING force field [24] is a well-known force field developed to handle a wide range of small organic molecules, including organometallic systems. The small number of adjustable parameters in this force field makes it easy to extend the force field to more complex systems. Van der Waals parameters not found in DREIDING were taken from the universal force field (UFF) [25]. DREIDING and UFF force-fields were designed to be very generic, so that broad coverage of the periodic table, including inorganic compounds, metals, and transition metals, could be achieved. UFF was tailored for simulating molecules containing any combination of elements in the periodic table. For the zeolites the TraPPE [26] force field was used. All van der Waals parameters used for the frameworks are listed in Table S3.

The charge-charge interactions were computed using the Ewald summation (relative precision 10^{-6}). Charges for the frameworks were computed by minimizing the difference of the classical electrostatic potential and a quantum mechanics electrostatic potential over many grid points using the REPEAT method [23, 27].

2.4 Monte Carlo simulations

In the canonical ensemble, the number of particles N , the temperature T , and the volume V are constant. The partition function is

$$Z_{\text{NVT}} = \frac{1}{\Lambda^{3N} N!} \int e^{-\beta U} d\mathbf{r}^N \quad (2.5)$$

where $\Lambda = \sqrt{h^2 / (2\pi m k_B T)}$ is the thermal de Broglie wavelength, h denotes Planck’s constant, m is the mass, $\beta = 1 / (k_B T)$, with k_B the Boltzmann constant, and $U(\mathbf{r}^N)$ is the total energy of the system with N particles at positions \mathbf{r}^N . The probability of finding configuration \mathbf{r}^N is given by

$$\mathcal{N}(\mathbf{r}^N) \propto e^{-\beta U(\mathbf{r}^N)} \quad (2.6)$$

The average of the variable $A(\mathbf{r}^N)$ in the NVT ensemble is given by

$$\langle A(\mathbf{r}^N) \rangle = \frac{\int A(\mathbf{r}^N) e^{-\beta U} d\mathbf{r}^N}{\int e^{-\beta U} d\mathbf{r}^N} \quad (2.7)$$

The Markov Chain Monte Carlo method (MCMC) is an important tool to estimate the average properties of systems with a very large number of accessible states. Often the quantity of interest are not the configurational part of the partition function itself, but averages of the type of Eq. 2.7. The ratio $e^{-\beta U} / Z$ is the probability density of finding the system in a configuration around \mathbf{r}^N . The Monte Carlo scheme makes use of the fact that only the relative probability of visiting points in configuration space is needed, *not* the

absolute probability. To visit points with the correct frequency, the MCMC algorithm generates random trial moves from the current (“old”) state (o) to a new state (n). To show that an arbitrary initial distribution eventually relaxes to the equilibrium distribution, it is often convenient to apply the condition of detailed balance (as is used in the original Metropolis scheme). If $P_B(o)$ and $P_B(n)$ denote the probability of finding the system in state (o) and (n), respectively, and $\alpha(o \rightarrow n)$ and $\alpha(n \rightarrow o)$ denote the conditional probability to perform a trial move from $o \rightarrow n$ and $o \rightarrow n$, respectively, then the probability $P_{\text{acc}}(o \rightarrow n)$ to accept the trial move from $o \rightarrow n$ is related to $P_{\text{acc}}(n \rightarrow o)$ by the following

$$P_B(o)\alpha(o \rightarrow n)P_{\text{acc}}(o \rightarrow n) = P_B(n)\alpha(n \rightarrow o)P_{\text{acc}}(n \rightarrow o) \quad (2.8)$$

Metropolis et al. assumed that

$$\alpha(o \rightarrow n) = \alpha(n \rightarrow o) \quad (2.9)$$

and fixed the acceptance probability using

$$P_{\text{acc}}(o \rightarrow n) = \min\left(1, \frac{P_B(n)}{P_B(o)}\right) \quad (2.10)$$

2.5 Computing adsorption isotherms

In adsorption studies one would like to know the amount of materials adsorbed as a function of pressure and temperature of the reservoir with which the sieve is in contact. Therefore the natural ensemble to use is the grand-canonical ensemble (or μ, V, T ensemble). In this ensemble, the temperature T , the volume V , and the chemical potential μ are fixed. The partition function is given by

$$Z_{\mu VT} \equiv \sum_{N=0}^{\infty} \frac{e^{\beta\mu N} V^N}{\Lambda^{3N} N!} \int e^{-\beta U(\mathbf{s}^N)} d\mathbf{s}^N \quad (2.11)$$

with a corresponding probability density

$$\mathcal{N}_{\mu VT} \propto \frac{e^{\beta\mu N} V^N}{\Lambda^{3N} N!} e^{-\beta U(\mathbf{s}^N)} \quad (2.12)$$

The Metropolis algorithm is implemented in the same way as for NVT ensemble, but now we also allow the number of particles to change. We have two additional Monte-Carlo moves. The creation of a particle is accepted with a probability

$$\text{acc}(N \rightarrow N+1) = \min\left(1, \frac{V}{\Lambda^3(N+1)} e^{\beta(\mu - U(N+1) + U(N))}\right) \quad (2.13)$$

and the removal of a particle is accepted with a probability

$$\text{acc}(N \rightarrow N-1) = \min\left(1, \frac{\Lambda^3 N}{V} e^{-\beta(\mu + U(N-1) - U(N))}\right) \quad (2.14)$$

The equilibrium conditions are that the temperature and chemical potential of the gas inside and outside the adsorbent must be equal. The imposed chemical potential μ can be related to the fugacity f

$$\beta\mu = \beta\mu_{\text{id}}^0 + \ln(\beta f), \quad (2.15)$$

where μ_{id}^0 is the reference chemical potential. All information of the reference state drops out, because it simply acts as a shift of the chemical potential that has no effect on the observable thermodynamic properties of the system. The fugacity f_j of component j in the reservoir is defined as the partial pressure of component j in the reservoir under the condition that the reservoir would be an ideal gas. Using the ideal gas law

$$f_j V \beta = N_j \quad (2.16)$$

we obtain for the insertion and deletion of a particle in the system

$$\text{acc}(N \rightarrow N + 1) = \min \left(1, \frac{V\beta f}{(N + 1)} e^{-\beta(U(N+1)-U(N))} \right) \quad (2.17)$$

$$\text{acc}(N \rightarrow N - 1) = \min \left(1, \frac{N}{V\beta f} e^{-\beta(U(N-1)-U(N))} \right) \quad (2.18)$$

The pressure p is related to the fugacity f by

$$f = \phi p, \quad (2.19)$$

where ϕ is the fugacity coefficient computed directly from the equation of state of the vapor in the reservoir. In our study we have plotted absolute loading versus the fugacity as this is not affected by gas-liquid transitions of the reservoir.

2.6 Configurational-Bias Monte Carlo

Conventional Monte Carlo (CBMC) is time-consuming for long chain molecules. The fraction of successful insertions into the sieve is too low. To increase the number of successfully inserted molecules we apply the CBMC technique. In the CBMC scheme it is convenient to split the total potential energy U of a trial site into two parts.

$$U = U^{\text{int}} + U^{\text{ext}}. \quad (2.20)$$

The first part is the internal, bonded potential U^{int} which is used for the generation of trial orientations. The second part of the potential, the external potential U^{ext} , is used to bias the selection of a site from the set of trial sites. This bias is exactly removed by adjusting the acceptance rules. In the CBMC technique a molecule is grown segment-by-segment. For each segment we generate a set of k trial orientations according to the internal energy U^{int} and compute the external energy $U_i^{\text{ext}}(j)$ of each trial position j of segment i . In this work the number of trial positions k is set to 10. We select one of these trial positions with a probability

$$P_i(j) = \frac{e^{-\beta U_i^{\text{ext}}(j)}}{\sum_{l=1}^k e^{-\beta U_i^{\text{ext}}(l)}} = \frac{e^{-\beta U_i^{\text{ext}}(j)}}{w(i)}. \quad (2.21)$$

The selected trial orientation is added to the chain and the procedure is repeated until the entire molecule has been grown. For this newly grown molecule we compute the so-called Rosenbluth factor

$$W^{\text{new}} = \prod_i w(i). \quad (2.22)$$

To compute the old Rosenbluth factor W^{old} of an already existing chain, $k - 1$ trial orientations are generated for each segment. These orientations, together with the already existing bond, form the set of k trial orientations. In a dynamic scheme, a Markov chain of states is generated. The average of a property is the average of over the elements of the Markov chain. For an infinite Markov chain the expression is exact. Every new configuration is accepted or rejected using an acceptance/rejection rule.

We have defined μ^{ex} as the difference in chemical potential of the interacting alkane and an alkane in the ideal gas state. The Rosenbluth weight $\langle W^{\text{IG}} \rangle$ of the reference state of the ideal gas is needed when comparing with real experimental data. When CBMC is used, it is straightforward to show that $e^{-\beta\Delta U}$ has to be replaced by $\frac{W(\text{new chain})}{W(\text{IG})}$ for inserting a particle and by $\frac{W(\text{IG})}{W(\text{old chain})}$ for the deletion of a particle. Detailed balance is obeyed when W^{IG} is replaced by $\langle W^{\text{IG}} \rangle$, i.e. the *average* Rosenbluth weight of a chain in the reservoir. This implies that $\langle W^{\text{IG}} \rangle$ has to be computed only *once* for a given molecule and temperature.

2.7 Continuous Fractional Monte Carlo

Continuous Fractional Monte Carlo (CFMC) was developed by Shi and Maginn [28] inspired by a group of schemes known as “expanded ensembles” [29, 30]. The system is expanded with an additional particle which interactions with the surrounding molecules are scaled using a parameter λ . Various choices for the

scaling are possible. In the original CFMC method, and also in this work, Lennard-Jones (LJ) interactions $u_{\text{LJ}}(r)$ and charge-charge interactions u_{Coul} are scaled as

$$u_{\text{LJ}}(r) = \lambda 4\epsilon \left[\frac{1}{\left[\frac{1}{2}(1-\lambda)^2 + \left(\frac{r}{\sigma}\right)^6\right]^2} - \frac{1}{\left[\frac{1}{2}(1-\lambda)^2 + \left(\frac{r}{\sigma}\right)^6\right]} \right] \quad (2.23)$$

$$u_{\text{Coul}} = \lambda^5 \frac{1}{4\pi\epsilon_0} \frac{q_i q_j}{r}. \quad (2.24)$$

where ϵ_0 is the dielectric constant in vacuum, R is the inter-atomic distance, q is the atomic charge, ϵ is the LJ strength parameter and σ is the LJ size parameter.

The modified form forces the potential to remain finite when $r \rightarrow 0$ for $\lambda \neq 1$. The scaled potential has the correct behavior at the limits of $\lambda = 0$ and $\lambda = 1$, *i.e.* for $\lambda = 0$ there are no interactions, and for $\lambda = 1$ the conventional LJ and Coulombic interactions are recovered. Note that only the inter-molecular energy (U^{inter}) is scaled. Many variations on the algorithm are possible. For example λ can be changed per molecule or per atom. In any case the method slowly “inflates” and “deflates” the molecule like a balloon.

CFMC uses conventional MC for thermalization (such as translations, rotations, and/or MC-MD hybrid moves[31, 32]), but in addition attempts to change λ of the fractional molecule using $\lambda(n) = \lambda(o) + \Delta\lambda$. The value of $\Delta\lambda$ is chosen uniformly between $-\Delta\lambda^{\text{max}}$ and $+\Delta\lambda^{\text{max}}$ and adjusted to achieve approximately 50% acceptance. However, many systems show behavior where λ -changes are difficult [28, 33, 34] because in the Boltzmann ensemble the distribution of λ can go through a deep minimum. An additional bias η on λ can be used, where each state of λ has an associated biasing factor η . This bias will be removed by the acceptance rules. A careful calibration of η will make the λ histograms flat and hence can avoid situations where the system gets stuck in certain λ -range. There are three possible outcomes of a change from $\lambda(o)$ to $\lambda(n)$:

- $\lambda(n)$ remains between 0 and 1:

The change in energy of the particle with the new $\lambda(n)$ compared to the old energy is computed and the move is accepted using

$$P_{\text{acc}} = \min(1, \exp[-\beta(U_{\text{inter}}(n) - U_{\text{inter}}(o)) + \eta(\lambda(n)) - \eta(\lambda(o))]) \quad (2.25)$$

There is no change in the number of particles, the positions, or in the intra-molecular energies. Only λ and the inter-molecular energy are changed.

- $\lambda(n)$ becomes larger than 1:

When $\lambda(n)$ exceeds unity, *i.e.* $\lambda(n) = 1 + \epsilon$, the current fractional molecule is made fully present ($\lambda = 1$), and an additional particle is randomly inserted with $\lambda = \epsilon$. In the original paper [28], an ideal gas molecule is taken from a reservoir of equilibrated gas phase molecules stored in the memory of the computer. In our implementation, the ideal gas molecule is generated “on the fly” during the simulation.

- $\lambda(n)$ becomes smaller than 0:

When $\lambda(n)$ falls below 0, *i.e.* $\lambda(n) = -\epsilon$, the current fractional molecule is removed from the system ($\lambda = 0$) and a new fractional molecule is chosen with $\lambda = 1 - \epsilon$.

The acceptance rules for insertion and deletion in the grand-canonical ensemble the rules are given by [28, 34]

$$P_{\text{acc}}(N \rightarrow N+1) = \min\left(1, \frac{f\beta V}{N+1} \exp[\eta(\lambda(n)) - \eta(\lambda(o))] \exp[-\beta(U_{\text{inter}}(n) - U_{\text{inter}}(o))]\right) \quad (2.26)$$

$$P_{\text{acc}}(N \rightarrow N-1) = \min\left(1, \frac{N}{f\beta V} \exp[\eta(\lambda(n)) - \eta(\lambda(o))] \exp[-\beta(U_{\text{inter}}(n) - U_{\text{inter}}(o))]\right) \quad (2.27)$$

where N is the number of *integer* molecules. Hence, measured properties and loadings should exclude the fractional molecule.

The CFMC method is able to force molecules into and out of the system. If the molecule is too quickly removed after insertion then nothing is gained. The environment should be able to adjust to the new insertion and equilibrate properly. The adjustment is also called thermalization. CFMC uses conventional MC

moves such as translation, rotation, and/or MC-MD hybrid moves for thermalization. In our implementation we also use (partial-)reinsertion moves using configurational biasing (identical to CBMC), for both integer molecules and the fractional molecules. The insertion of an additional molecule is already biased using λ -biasing and as soon as the molecule is present in the system the reinsertion is able to efficiently move the molecules around in the system.

Shi and Maginn found that Wang-Landau sampling is very efficient in obtaining the biasing factors for CFMC [28, 33, 35]. The objective of the Wang-Landau sampling method [36, 37] is to make all system energy states equally probable. In CFMC this translates in making all system λ states equally probable. During a random walk the weights are iteratively adjusted using importance sampling. The λ range is for example divided into 20 bins. Initially all biasing factors are zero. During equilibration the bin corresponding to the current λ is modified according to $\eta(\lambda_j) \rightarrow \eta(\lambda_j) - \nu$ after a MC move attempt, where ν is a scaling parameter initially set to 0.01. Histograms are measured and every 10000 attempts checked for flatness. The histogram is considered sufficiently flat when all bins are at least 30% as often visited as the most visited bin. If so, then the histograms are set to zero and the scaling factor is modified to $\nu \rightarrow \frac{1}{2}\nu$. Equilibration of η can be stopped once the value of ν is lower than 10^{-6} .

2.8 Monte Carlo moves for thermalization

Several types of Monte Carlo moves (in addition to insertion/deletion moves) are employed during a simulation to thermalize the system

- Displacement move

A molecule is selected at random and given a random displacement. The maximum displacement is taken such that 50% of the moves is accepted. The acceptance rule is

$$\text{acc}(\text{old} \rightarrow \text{new}) = \min\left(1, e^{-\beta(U^{\text{new}} - U^{\text{old}})}\right). \quad (2.28)$$

Note that the energy of the new configuration U^{new} and the energy of the old configuration U^{old} only differ in the external energy.

- Rotation move

A molecule is selected at random and given a random rotation. The center of the rotation is the center of mass. The maximum rotation angle is selected such that 50% of the moves are accepted. The acceptance rule is given by Eq. 2.28. Again, the energy of the new configuration U^{new} and the energy of the old configuration U^{old} only differ in the external energy.

- Insertion move

A molecule is inserted at a random position. The acceptance rule for insertion of the particle is given by

$$\text{acc}(N \rightarrow N + 1) = \min\left(1, \frac{W^{\text{new}} \beta V}{N + 1} \frac{f}{\langle W^{\text{IG}} \rangle}\right). \quad (2.29)$$

- Deletion move

A molecule is chosen at a random position and the old Rosenbluth factor is computed. The acceptance rule for deletion of the particle is given by

$$\text{acc}(N \rightarrow N - 1) = \min\left(1, \frac{N}{W^{\text{old}} \beta V} \frac{\langle W^{\text{IG}} \rangle}{f}\right). \quad (2.30)$$

- Full reinsertion move

A molecule is selected at random and is reinserted at a random position. The acceptance rule for full reinsertion move is given by

$$\text{acc}(\text{old} \rightarrow \text{new}) = \min\left(1, \frac{W^{\text{new}}}{W^{\text{old}}}\right). \quad (2.31)$$

Simulations are performed in cycles. The number of cycles needed for equilibration depends on the number of molecules. We define a cycle to consist of smaller steps proportional to the number number of molecules with 20 as the minimum.

$$N_{\text{cycles}} = \max(20, N) \times N_{\text{steps}}. \quad (2.32)$$

In each step one Monte Carlo move is performed. For the isotherms we used at least 500000 initialization cycles, while 500000 cycles are used to compute the isotherms. The error bars in the isotherms are computed by dividing the simulations results up into five blocks. The error is computed from the standard deviation of the five blocks and corresponds to the 95% confidence interval.

3

BaX

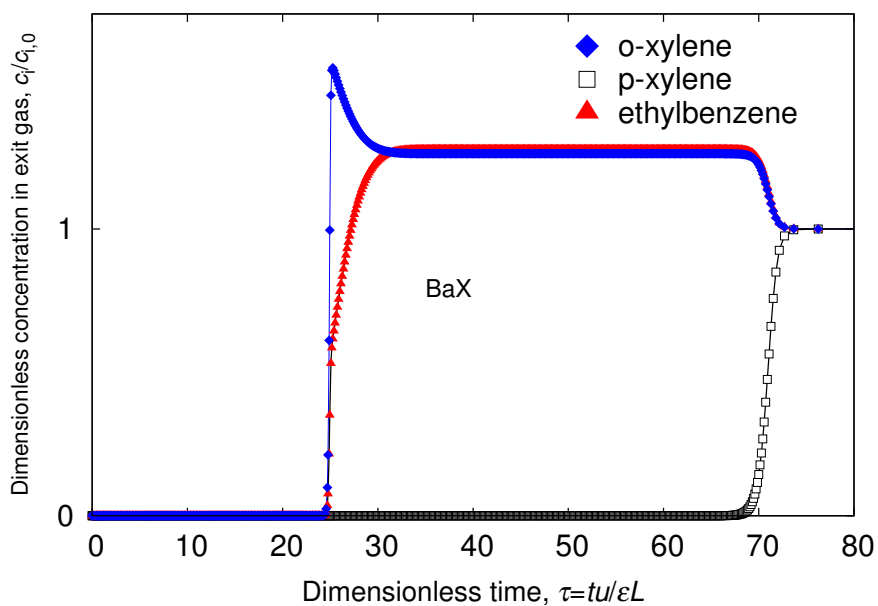


Figure S6: Breakthrough simulations for CS hydrocarbons in BaX assuming thermodynamic equilibrium i.e. invoking Equation 6.2. The isotherm data are taken from Minceva and Rodrigues [38]. The adsorption isotherms for o-xylene and m-xylene are nearly the same, and the breakthroughs of these isomers will occur at nearly the same times.

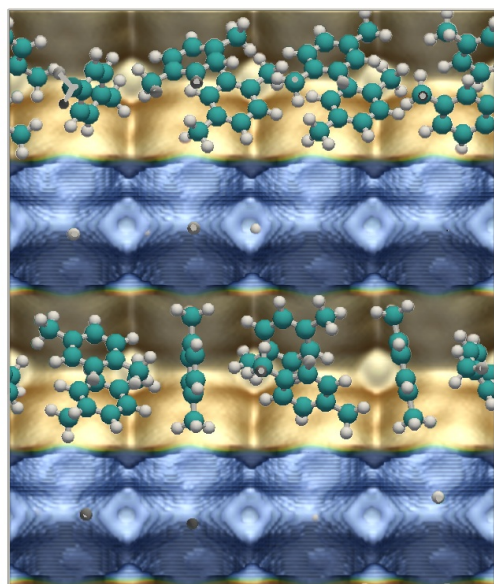
Minceva and Rodrigues [38] did not report the isotherm data for m-xylene; therefore, we performed breakthrough calculations for BaX for 2:1:1 o-xylene/p-xylene/ethylbenzene mixture. These breakthrough calculations should be a good reflection of the performance of BaX for a 4-component mixture that also contains m-xylene.

4

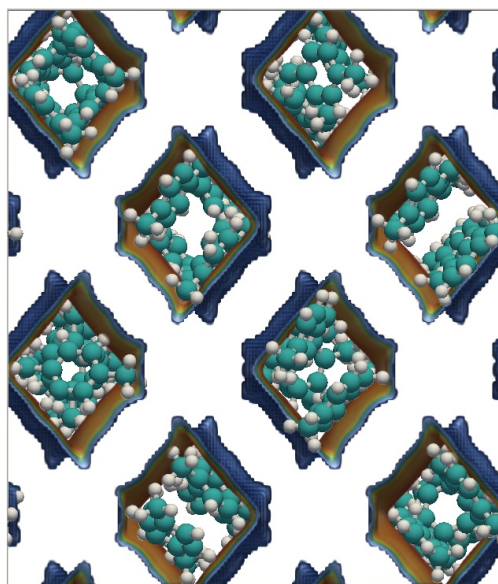
Short-list of Potential Adsorbents

4.1 MIL-47(V)

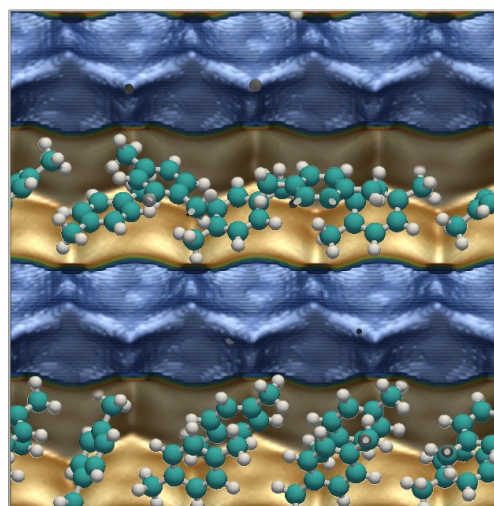
4.1.1 Energy landscapes



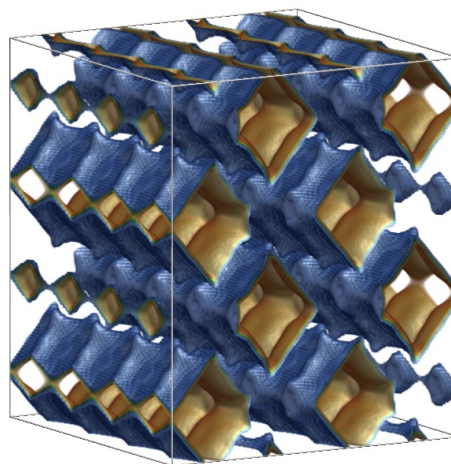
(a) MIL-47(V) ($4 \times 2 \times 2$); XY-view.



(b) MIL-47(V) ($4 \times 2 \times 2$); XZ-view.



(c) MIL-47(V) ($4 \times 2 \times 2$); YZ-view



(d) MIL-47(V) ($4 \times 2 \times 2$); XYZ-view

Figure S7: Energy landscape of a system of $4 \times 2 \times 2$ MIL-47(V) unit cells. The MIL-47(V) unit cell has edge lengths $a = 6.8179 \text{ \AA}$, $b = 16.143 \text{ \AA}$, and $c = 13.939 \text{ \AA}$, with cell angles $\alpha = \beta = \gamma = 90^\circ$. The MIL-47(V) pore system consists of lozenge-shaped rhombohedral channels running in a -direction. About 61% of the structure is void. Shown adsorbates: p -xylene at 1 kPa and 433K. Color code: carbon (cyan), hydrogen (white).

4.1.2 Stacking of o-xylene in MIL-47

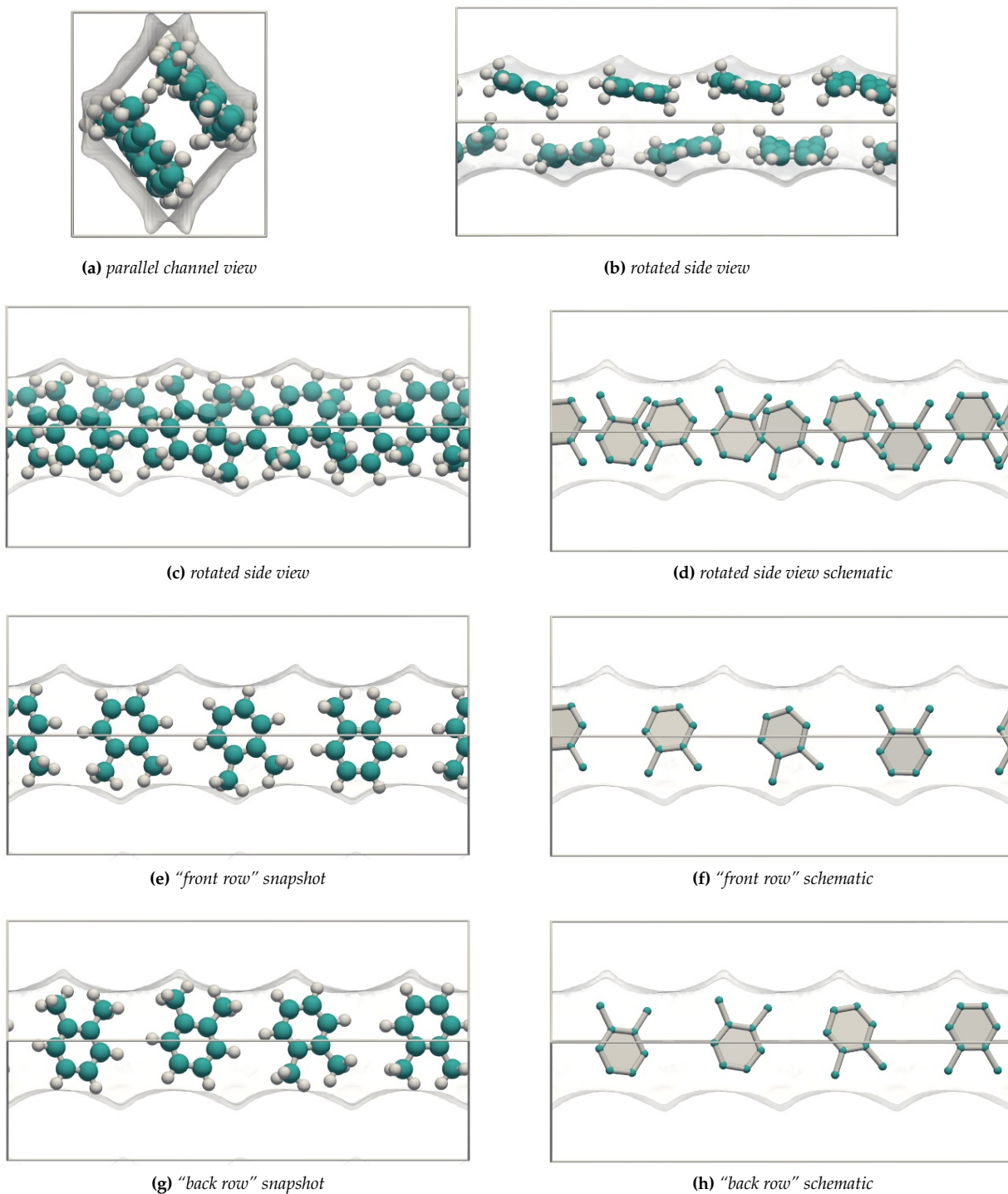
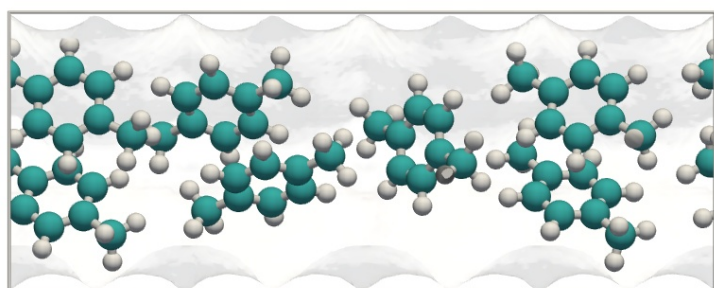
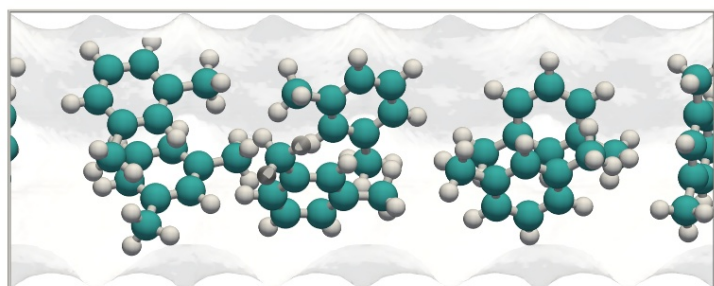
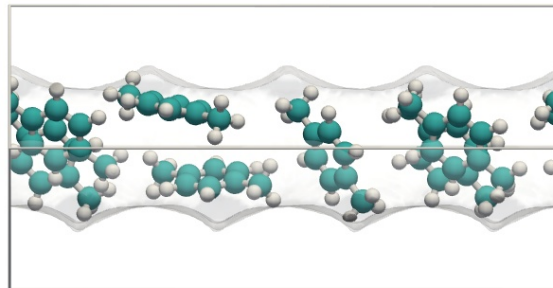


Figure S8: Stacking of o-xylene in MIL-47(V). The molecules are stacked in an alternating fashion. Ortho-xylene is able to make efficient use of the space available in the MIL-47(V) structure. The size of the channel allows the methyl groups of o-xylene to interact with the benzene groups of the structure and pack in a two layers. Color code: carbon (cyan), hydrogen (white).

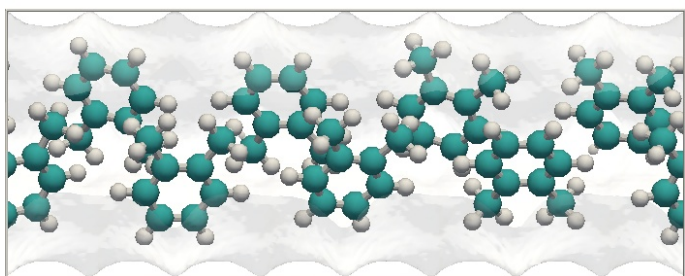
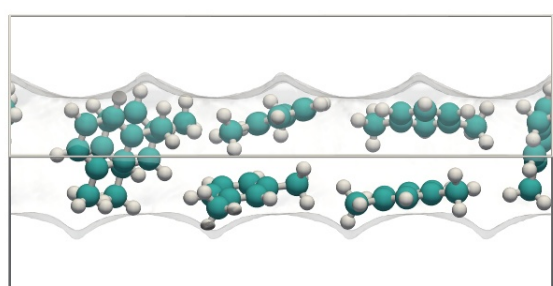
4.1.3 Snapshots



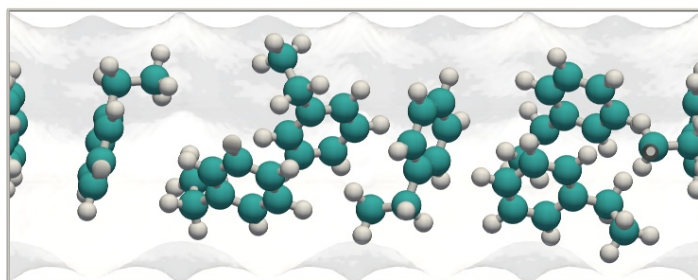
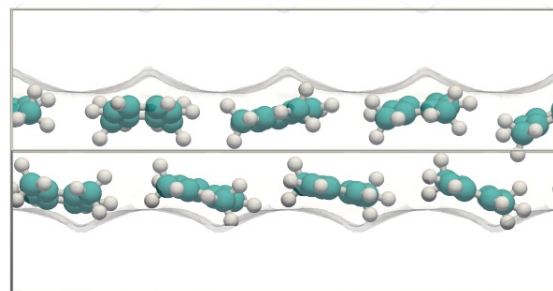
(a) *p*-xylene.



(b) *m*-xylene.



(c) *o*-xylene.



(d) ethylbenzene.

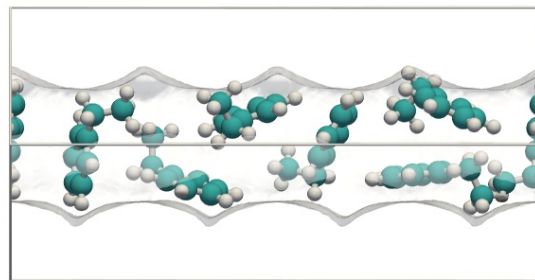


Figure S9: Snapshots of *p*-xylene, *o*-xylene, *m*-xylene, and ethylbenzene in MIL-47(V) at 10 kPa and 433 K. The left side snapshots correspond to the XY view of a channel. The right snapshots correspond to a clockwise rotation around the channel axis. Color code: carbon (cyan), hydrogen (white).

4.1.4 Langmuir-Freundlich parameters

	site A			site B		
	$q_{i,A,sat}$ [molec. uc ⁻¹]	$b_{i,A}$ [Pa ^{-$\nu_{i,A}$]}	$\nu_{i,A}$ [-]	$q_{i,B,sat}$ [molec. uc ⁻¹]	$b_{i,B}$ [Pa ^{-$\nu_{i,B}$]}	$\nu_{i,B}$ [-]
o-xylene	2.8	5.03×10^{-3}	1.08	0.8	3.78×10^{-4}	0.8
m-xylene	2.6	2.48×10^{-3}	1.1	0.8	3.86×10^{-5}	0.9
p-xylene	2.8	3.22×10^{-3}	1.07	0.8	3.23×10^{-5}	0.9
ethylbenzene	0.9	3.94×10^{-4}	0.62	2.2	4.73×10^{-3}	1.05
benzene	4	1.23×10^{-4}	1	0.45	3.03×10^{-8}	0.95
toluene	0.85	4×10^{-7}	1.4	3.1	8.68×10^{-4}	1.04

Table S4: Dual-site Langmuir-Freundlich parameters for pure component xylene isomers at 433 K in MIL-47(V). The saturation capacities are expressed in molecules per unit cell; these numbers need to be multiplied by the conversion factor of 1.082.

4.1.5 Adsorption isotherms

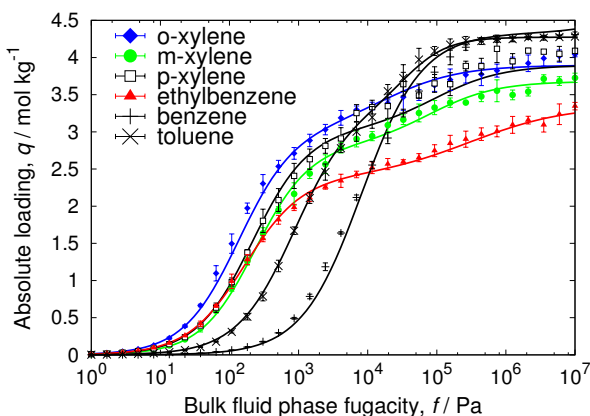
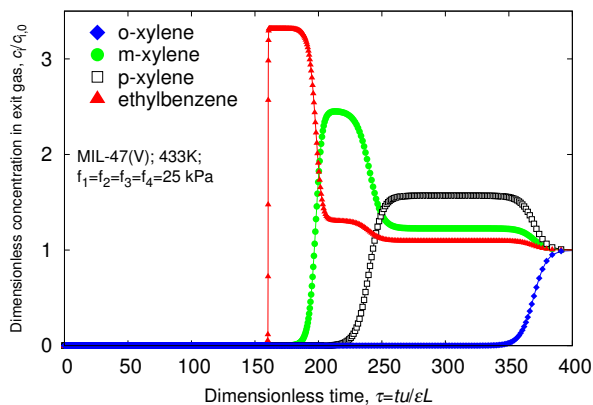
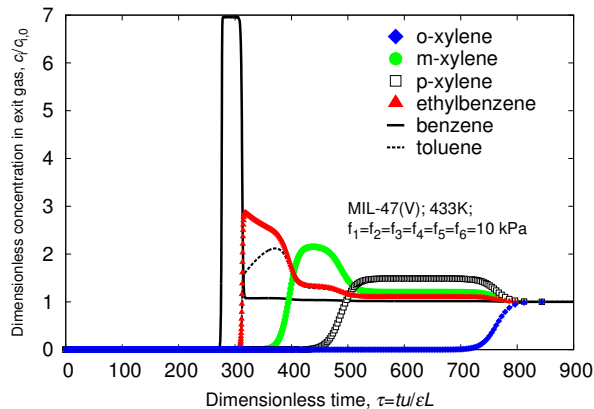


Figure S10: Pure component isotherms of xylene isomers (lines are dual-site Langmuir-Freundlich fits of the pure components, points are the pure component isotherms from CFMC simulations).

4.1.6 Breakthrough simulations



(a) 4-component equimolar mixture of o-, m-, p-xylene and ethylbenzene

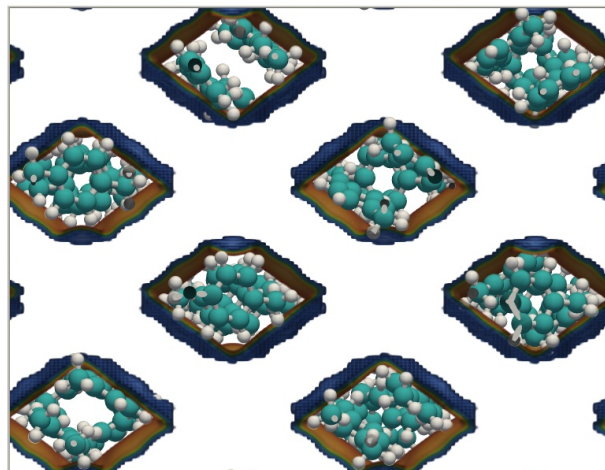


(b) 6-component equimolar mixture of o-, m-, p-xylene and ethylbenzene mixed with benzene and toluene

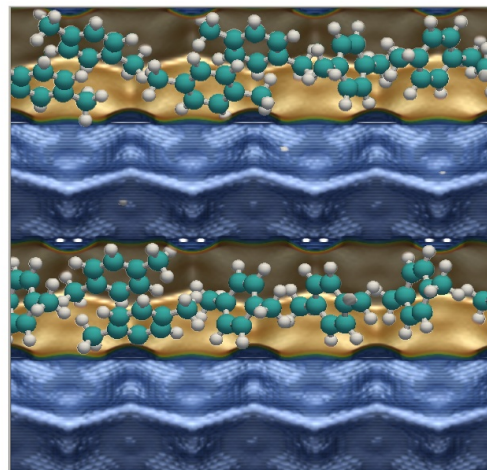
Figure S11: Simulated step-type breakthrough of xylene isomers in MIL-47(V) at 433K. Video animations of the breakthrough behavior as a function of time are provided as Supplementary information.

4.2 MIL-53(Al)

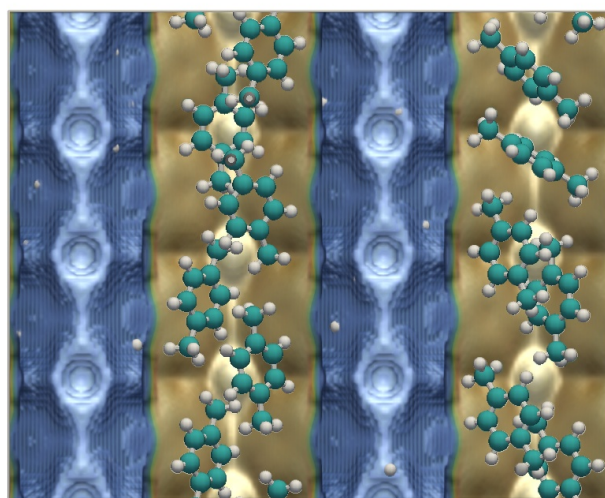
4.2.1 Energy landscapes



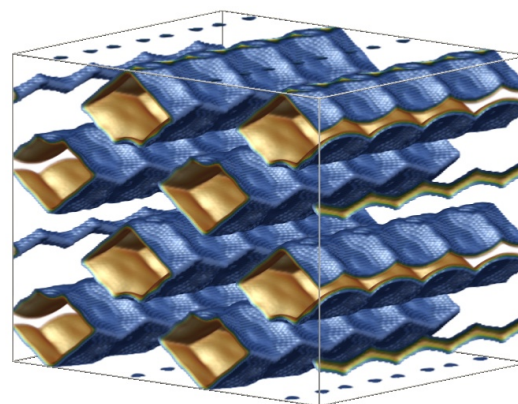
(a) MIL-53(Al) ($2 \times 2 \times 4$); XY-view.



(b) MIL-53(Al) ($2 \times 2 \times 4$); XZ-view.



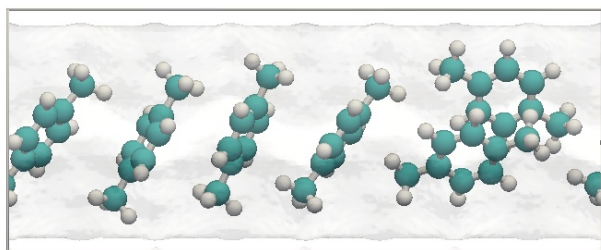
(c) MIL-53(Al) ($2 \times 2 \times 4$); YZ-view



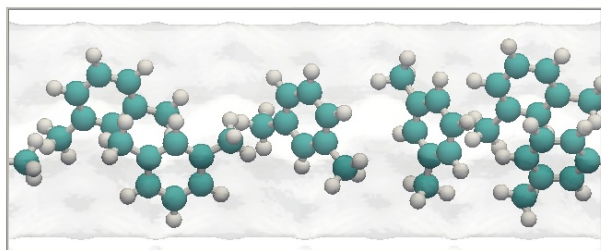
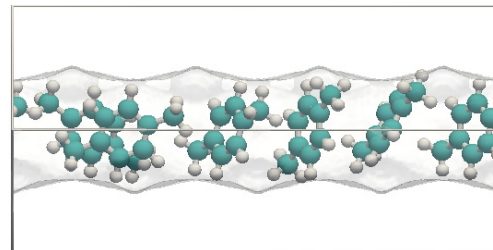
(d) MIL-53(Al) ($2 \times 2 \times 4$); XYZ-view

Figure S12: Energy landscape of a system of $2 \times 2 \times 4$ MIL-53(Al) unit cells. The MIL-53(Al) unit cell has edge lengths $a = 16.733 \text{ \AA}$, $b = 13.038 \text{ \AA}$, and $c = 6.812 \text{ \AA}$, with cell angles $\alpha = \beta = \gamma = 90^\circ$. The MIL-53(Al) pore system consists of lozenge-shaped rhombohedral channels running in c -direction. About 55% of the structure is void. Shown adsorbates: p -xylene at 1 kPa and 433K. Color code: carbon (cyan), hydrogen (white).

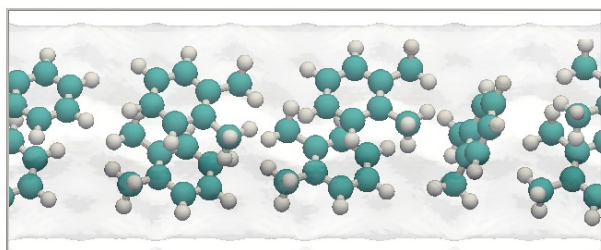
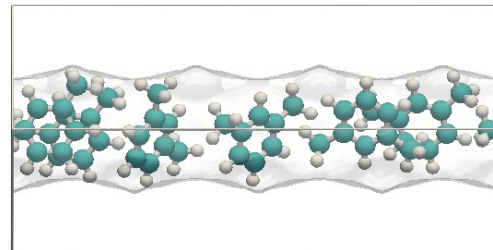
4.2.2 Snapshots



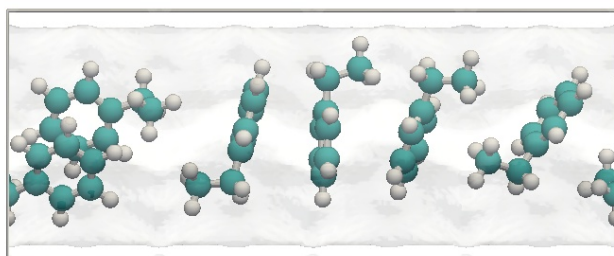
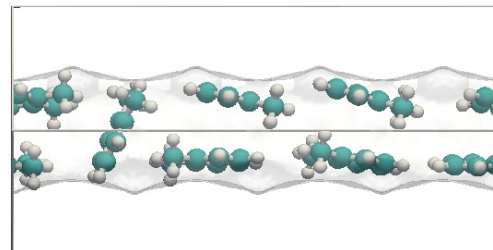
(a) *p*-xylene.



(b) *m*-xylene.



(c) *o*-xylene.



(d) ethylbenzene.

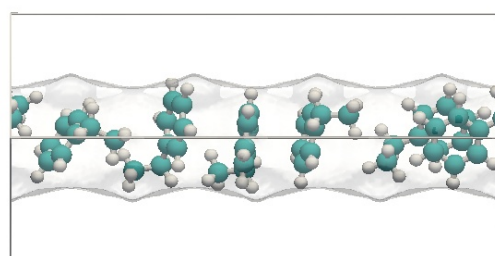


Figure S13: Snapshots of *p*-xylene, *o*-xylene, *m*-xylene, and ethylbenzene in MIL-53(Al) at $10e7$ Pa and 433 K. The left side snapshots correspond to the XZ view of a channel. The right snapshots correspond to a clockwise rotation around the channel axis. Color code: carbon (cyan), hydrogen (white).

4.2.3 Langmuir-Freundlich parameters

	site A			site B		
	$q_{i,A,sat}$ [molec. uc ⁻¹]	$b_{i,A}$ [Pa ^{-$\nu_{i,A}$}]	$\nu_{i,A}$ [-]	$q_{i,B,sat}$ [molec. uc ⁻¹]	$b_{i,B}$ [Pa ^{-$\nu_{i,B}$}]	$\nu_{i,B}$ [-]
o-xylene	2.2	7.22×10^{-3}	1.05	0.74	2.21×10^{-4}	0.74
m-xylene	1.9	5.01×10^{-3}	1	0.9	7.44×10^{-5}	0.74
p-xylene	2	5.34×10^{-3}	1.06	0.81	1.47×10^{-4}	0.8
ethylbenzene	0.6	6.02×10^{-5}	0.79	2	6.97×10^{-3}	1
benzene	2.2	2.53×10^{-4}	1.06	1.8	5.95×10^{-5}	0.76
toluene	1.1	3.74×10^{-5}	0.74	2.3	7.76×10^{-4}	1.1

Table S5: Dual-site Langmuir-Freundlich parameters for pure component xylene isomers at 433 K in MIL-53(AI). The saturation capacities are expressed in molecules per unit cell; these numbers need to be multiplied by the conversion factor of 1.0724.

4.2.4 Adsorption isotherms

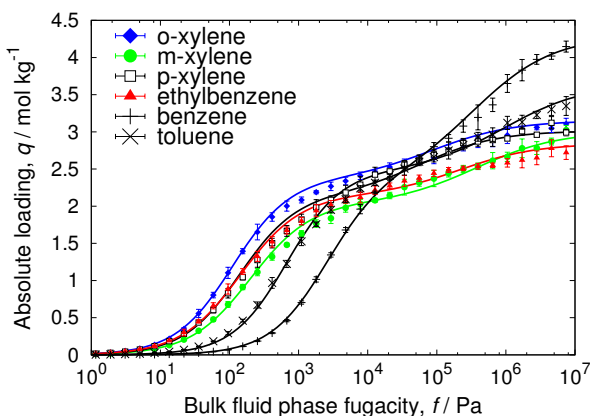
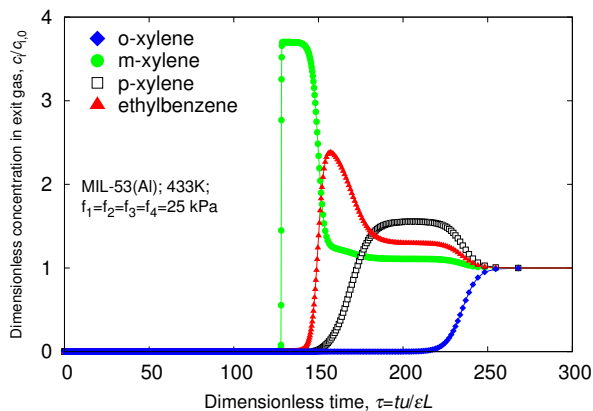
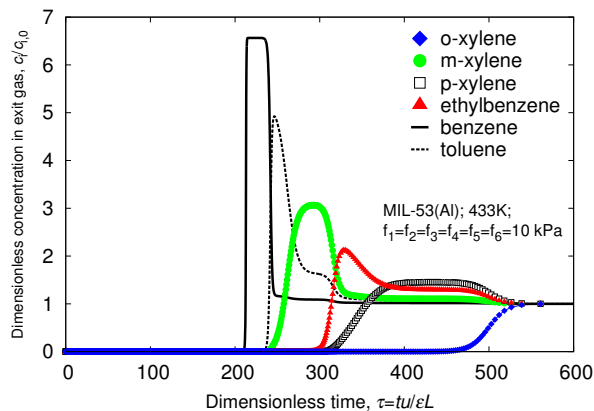


Figure S14: Pure component isotherms of xylene isomers (lines are dual-site Langmuir-Freundlich fits of the pure components, points are the pure component isotherms from CFMC simulations).

4.2.5 Breakthrough simulations



(a) 4-component equimolar mixture of o-, m-, p-xylene and ethylbenzene

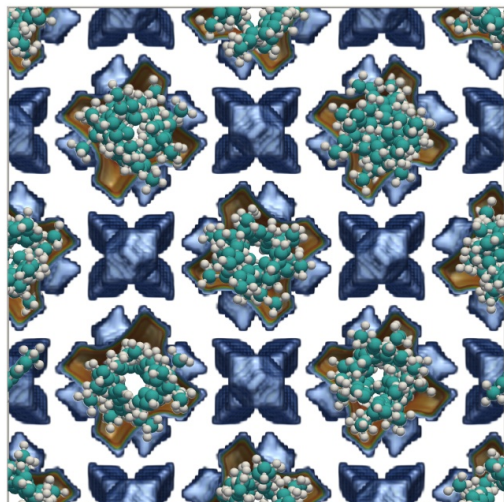


(b) 6-component equimolar mixture of o-, m-, p-xylene and ethylbenzene mixed with benzene and toluene

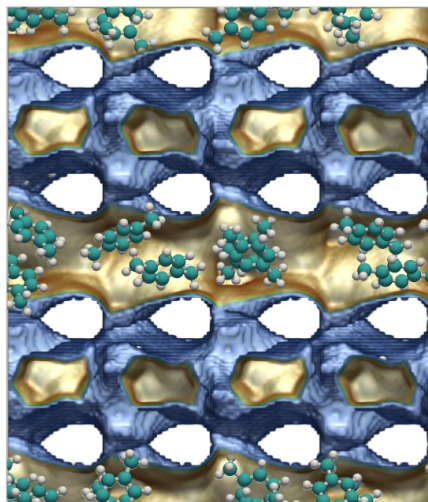
Figure S15: Simulated step-type breakthrough of xylene isomers in MIL-53(AI) at 433K. Video animations of the breakthrough behavior as a function of time are provided as Supplementary information.

4.3 MOF-CJ3

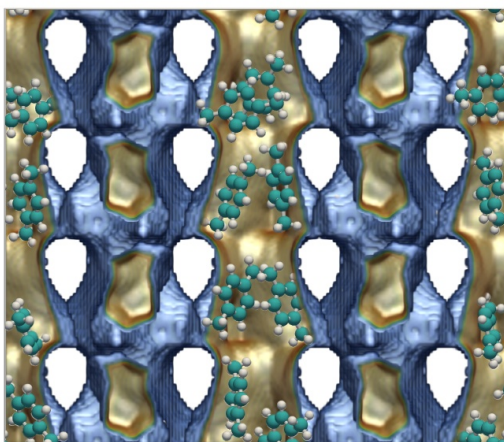
4.3.1 Energy landscapes



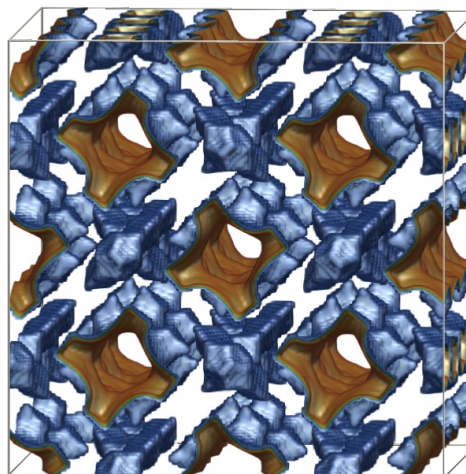
(a) MOF-CJ3 ($2 \times 2 \times 2$); XY-view.



(b) MOF-CJ3 ($2 \times 2 \times 2$); XZ-view



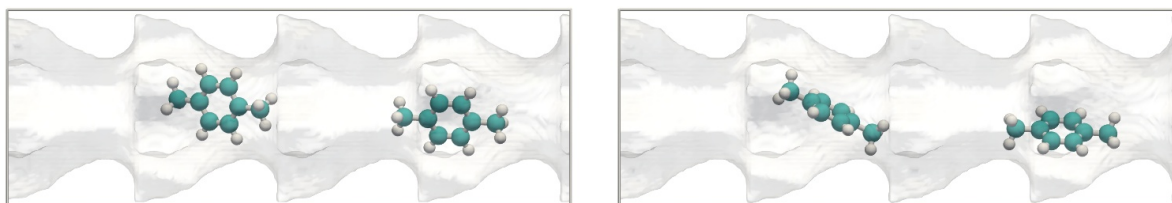
(c) MOF-CJ3 ($2 \times 2 \times 2$); YZ-view



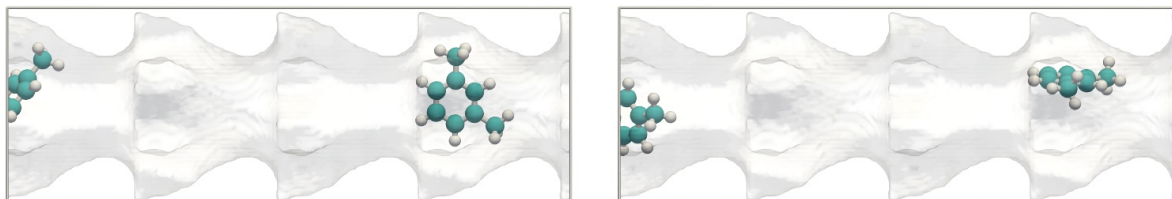
(d) MOF-CJ3 ($2 \times 2 \times 2$); XYZ-view

Figure S16: Energy landscape of a system of $2 \times 2 \times 2$ MOF-CJ3 unit cells. The MOF-CJ3 unit cell has edge lengths $a = 20.588 \text{ \AA}$, $b = 20.588 \text{ \AA}$, and $c = 17.832 \text{ \AA}$, with cell angles $\alpha = \beta = \gamma = 90^\circ$. The MOF-CJ3 pore system consists of rectangular channels running in the c -direction. About 45% of the structure is void. Shown adsorbates: p -xylene at 1 kPa and 433K. Color code: carbon (cyan), hydrogen (white).

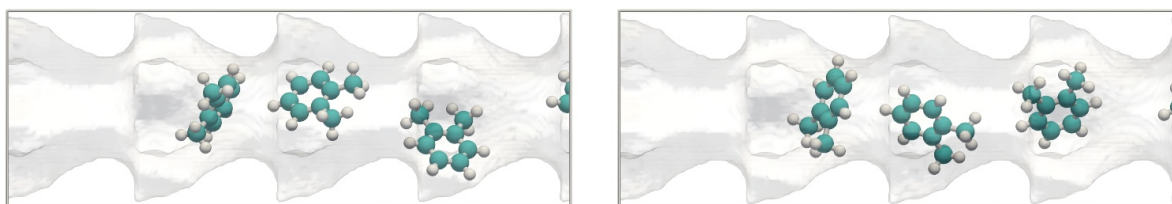
4.3.2 Snapshots



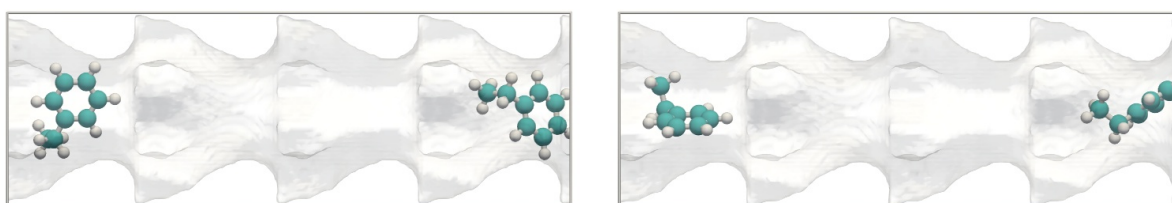
(a) *p*-xylene.



(b) *m*-xylene.



(c) *o*-xylene.



(d) ethylbenzene.

Figure S17: Snapshots of *p*-xylene, *o*-xylene, *m*-xylene, and ethylbenzene in MOF-CJ3 at 100 Pa and 433 K. Color code: carbon (cyan), hydrogen (white).

4.3.3 Langmuir-Freundlich parameters

	site A			site B		
	$q_{i,A,sat}$ [mol kg ⁻¹]	$b_{i,A}$ [Pa ^{-$\nu_{i,A}$}]	$\nu_{i,A}$ [-]	$q_{i,B,sat}$ [mol kg ⁻¹]	$b_{i,B}$ [Pa ^{-$\nu_{i,B}$}]	$\nu_{i,B}$ [-]
o-xylene	1.4	7.06×10^{-3}	1.04	1.8	2.43×10^{-7}	1.09
m-xylene	1.4	5.28×10^{-3}	1	0.83	5.79×10^{-8}	1
p-xylene	1.36	4.57×10^{-3}	1	0.8	2.01×10^{-7}	1
ethylbenzene	1.2	5.22×10^{-3}	1	0.3	2.91×10^{-5}	1
benzene	2.3	1.52×10^{-4}	1	-	-	-
toluene	1.55	1.05×10^{-3}	1	1	8.59×10^{-6}	1

Table S6: Dual-site Langmuir-Freundlich parameters for pure component xylene isomers at 433 K in MOF-CJ3.

4.3.4 Adsorption isotherms

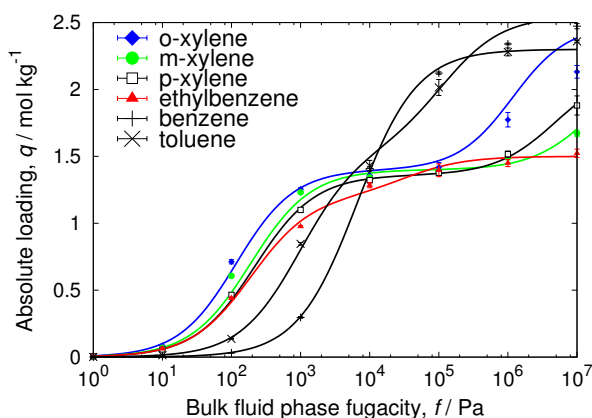
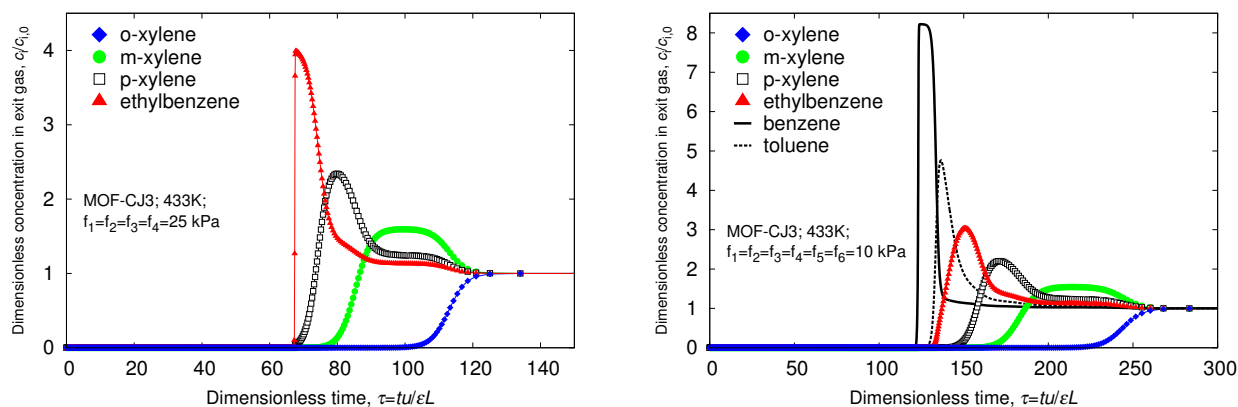


Figure S18: Pure component isotherms of xylene isomers (lines are dual-site Langmuir-Freundlich fits of the pure components, points are the pure component isotherms from CFMC simulations).

4.3.5 Breakthrough simulations



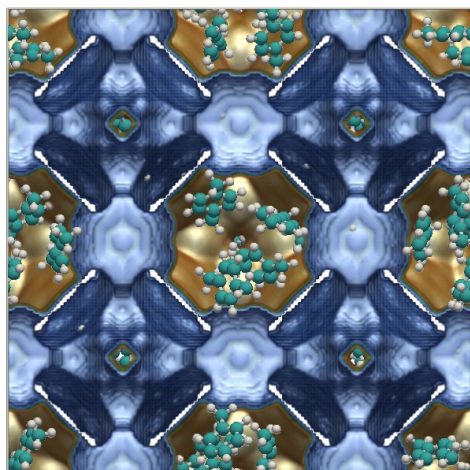
(a) 4-component equimolar mixture of o-, m-, p-xylene and ethylbenzene

(b) 6-component equimolar mixture of o-, m-, p-xylene and ethylbenzene mixed with benzene and toluene

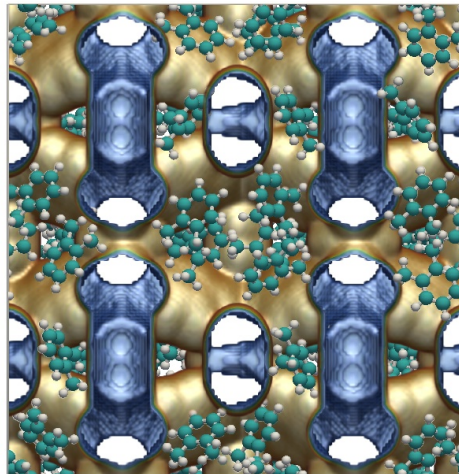
Figure S19: Simulated step-type breakthrough of xylene isomers in MOF-CJ3 at 433K. Video animations of the breakthrough behavior as a function of time are provided as Supplementary information.

4.4 MIL-125(Ti)

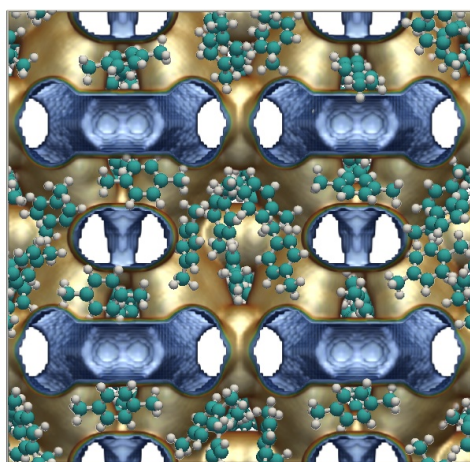
4.4.1 Energy landscapes



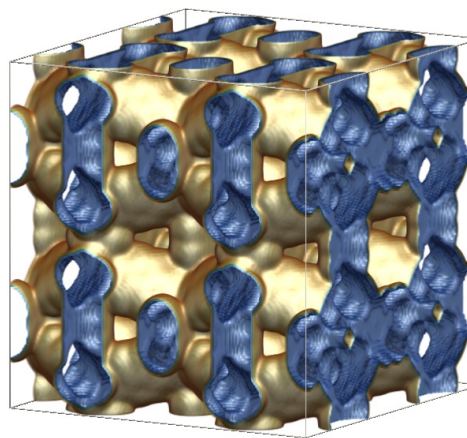
(a) MIL-125(Ti) ($2 \times 2 \times 2$); XY-view.



(b) MIL-125(Ti) ($2 \times 2 \times 2$); XZ-view.



(c) MIL-125(Ti) ($2 \times 2 \times 2$); YZ-view



(d) MIL-125(Ti) ($2 \times 2 \times 2$); XYZ-view

Figure S20: Energy landscape of a system of $2 \times 2 \times 2$ MIL-125(Ti) unit cells. The MIL-125(Ti) unit cell has edge lengths $a = 18.6543 \text{ \AA}$, $b = 18.6543 \text{ \AA}$, and $c = 18.1444 \text{ \AA}$, with cell angles $\alpha = \beta = \gamma = 90^\circ$. The MIL-125 pore system consists of two different types of cages, larger octahedral cages and smaller tetrahedral cages. About 62% of the structure is void. Shown adsorbates: *p*-xylene at 10^6 Pa and 433K . Color code: carbon (cyan), hydrogen (white).

4.4.2 Snapshots

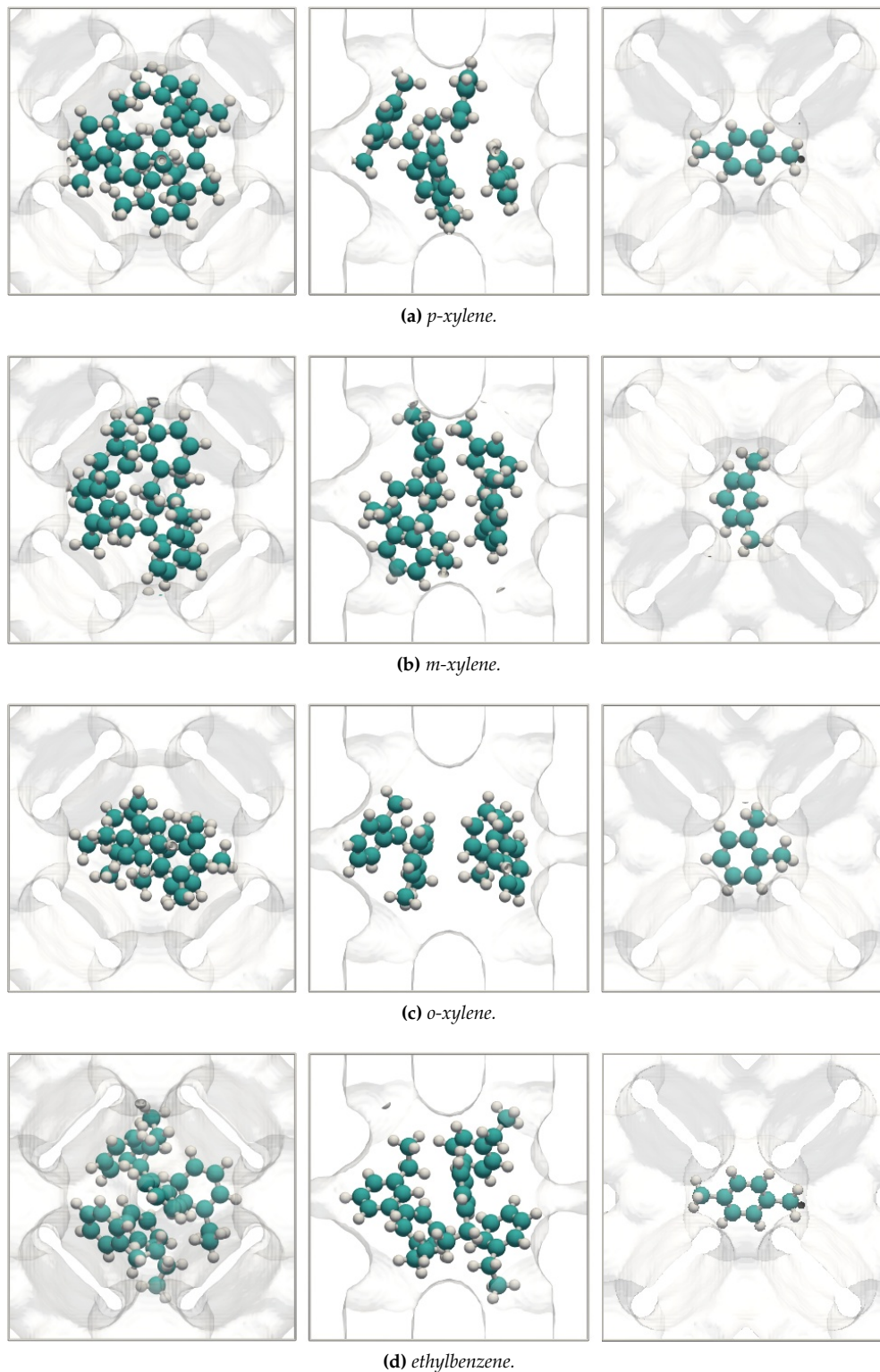


Figure S21: Snapshots of *p*-xylene, *o*-xylene, *m*-xylene, and ethylbenzene in MIL-125(Ti) at 10e6 Pa and 433 K. The saturation loading of *p*-xylene, *o*-xylene, and ethylbenzene is the same. The saturation value for *m*-xylene is lower because it does not fit comfortably in the tetrahedral cage. Color code: carbon (cyan), hydrogen (white).

4.4.3 Langmuir-Freundlich parameters

	site A			site B		
	$q_{i,A,sat}$ [mol kg ⁻¹]	$b_{i,A}$ [Pa ^{-$v_{i,A}$}]	$v_{i,A}$ [-]	$q_{i,B,sat}$ [mol kg ⁻¹]	$b_{i,B}$ [Pa ^{-$v_{i,B}$}]	$v_{i,B}$ [-]
o-xylene	2.4	3.86×10^{-5}	0.83	2.6	4.06×10^{-5}	1.2
m-xylene	1.8	1.23×10^{-5}	0.83	2.9	3.53×10^{-5}	1.2
p-xylene	0.95	1.73×10^{-5}	0.8	4	2.93×10^{-5}	1.2
ethylbenzene	0.75	4.4×10^{-28}	6.7	3.8	3.75×10^{-5}	1
benzene	1.45	7.43×10^{-6}	0.72	5.2	8.6×10^{-8}	1.5
toluene	4.8	5.93×10^{-6}	1.2	1.06	1.1×10^{-5}	0.67

Table S7: Dual-site Langmuir-Freundlich parameters for pure component xylene isomers at 433 K in MIL-125(Ti).

4.4.4 Adsorption isotherms

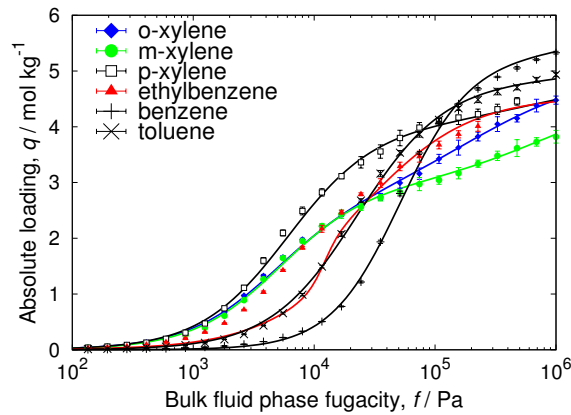
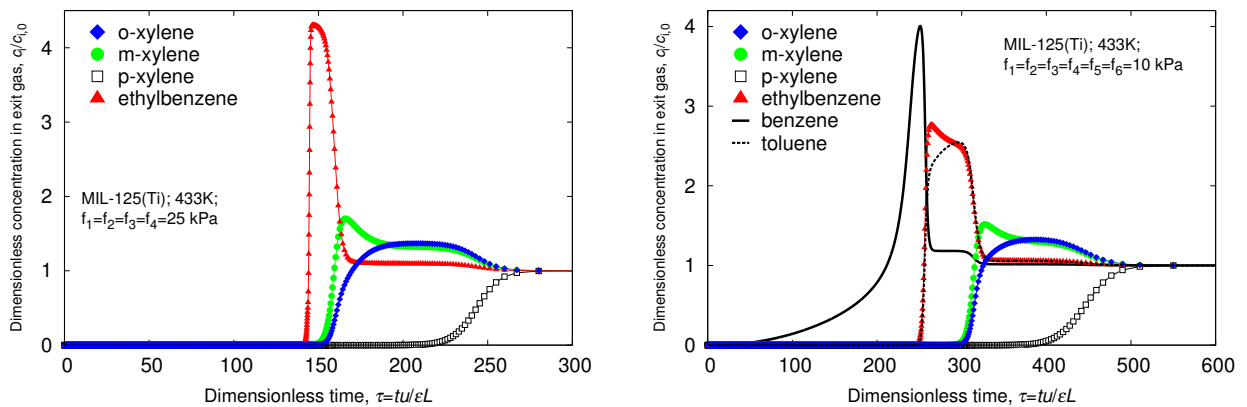


Figure S22: Pure component isotherms of xylene isomers (lines are dual-site Langmuir-Freundlich fits of the pure components, points are the pure component isotherms from CFMC simulations).



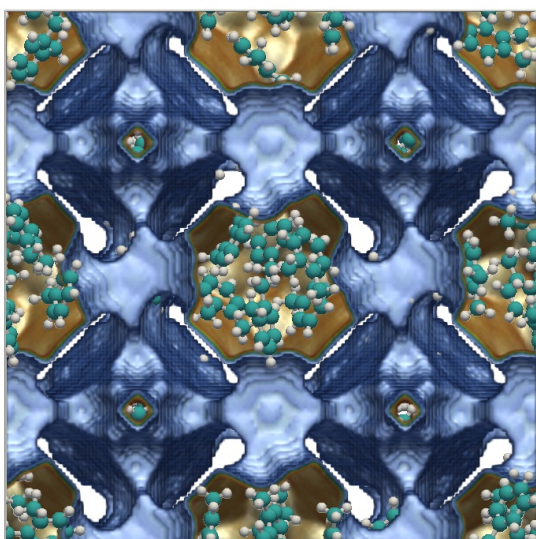
(a) 4-component equimolar mixture of o-, m-, p-xylene and ethylbenzene

(b) 6-component equimolar mixture of o-, m-, p-xylene and ethylbenzene mixed with benzene and toluene

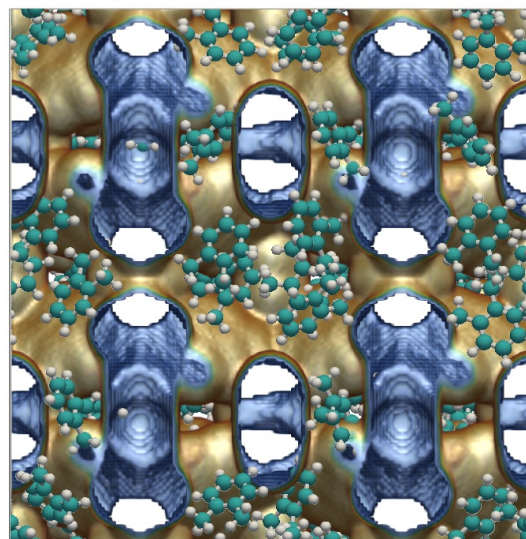
Figure S23: Simulated step-type breakthrough of xylene isomers in MIL-125(Ti) at 433K. Video animations of the breakthrough behavior as a function of time are provided as Supplementary information.

4.5 MIL-125(Ti)-NH₂

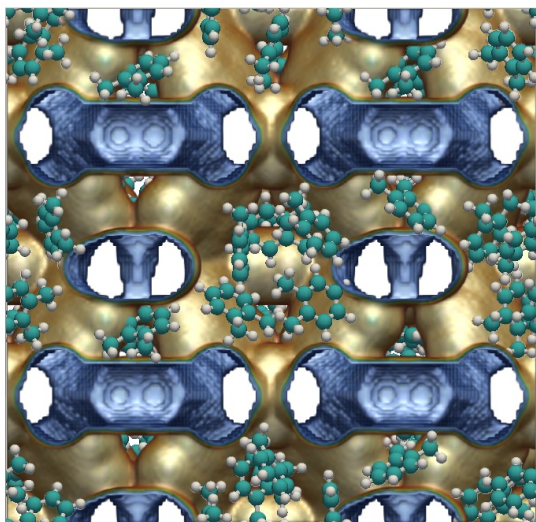
4.5.1 Energy landscapes



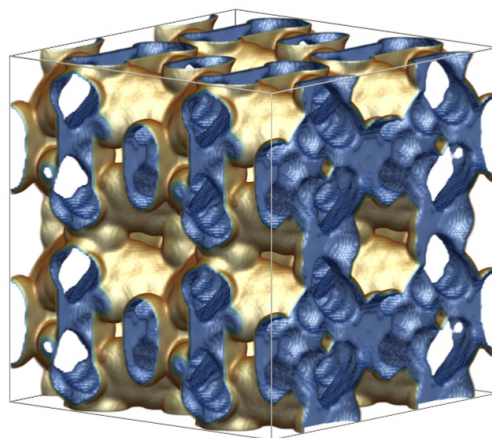
(a) MIL-125(Ti)-NH₂ ($2 \times 2 \times 2$); XY-view.



(b) MIL-125(Ti)-NH₂ ($2 \times 2 \times 2$); XZ-view.



(c) MIL-125(Ti)-NH₂ ($2 \times 2 \times 2$); YZ-view



(d) MIL-125(Ti)-NH₂ ($2 \times 2 \times 2$); XYZ-view

Figure S24: Energy landscape of a system of $2 \times 2 \times 2$ MIL-125(Ti)-NH₂ unit cells. The MIL-125(Ti)-NH₂ unit cell has edge lengths $a = 18.729 \text{ \AA}$, $b = 18.729 \text{ \AA}$, and $c = 18.172 \text{ \AA}$, with cell angles $\alpha = \beta = \gamma = 90^\circ$. The MIL-125-NH₂ pore system consists of octahedral and tetrahedral cages connected by channels. About 59% of the structure is void. Shown adsorbates: *p*-xylene at 1 kPa and 433K. Color code: carbon (cyan), hydrogen (white).

4.5.2 Snapshots

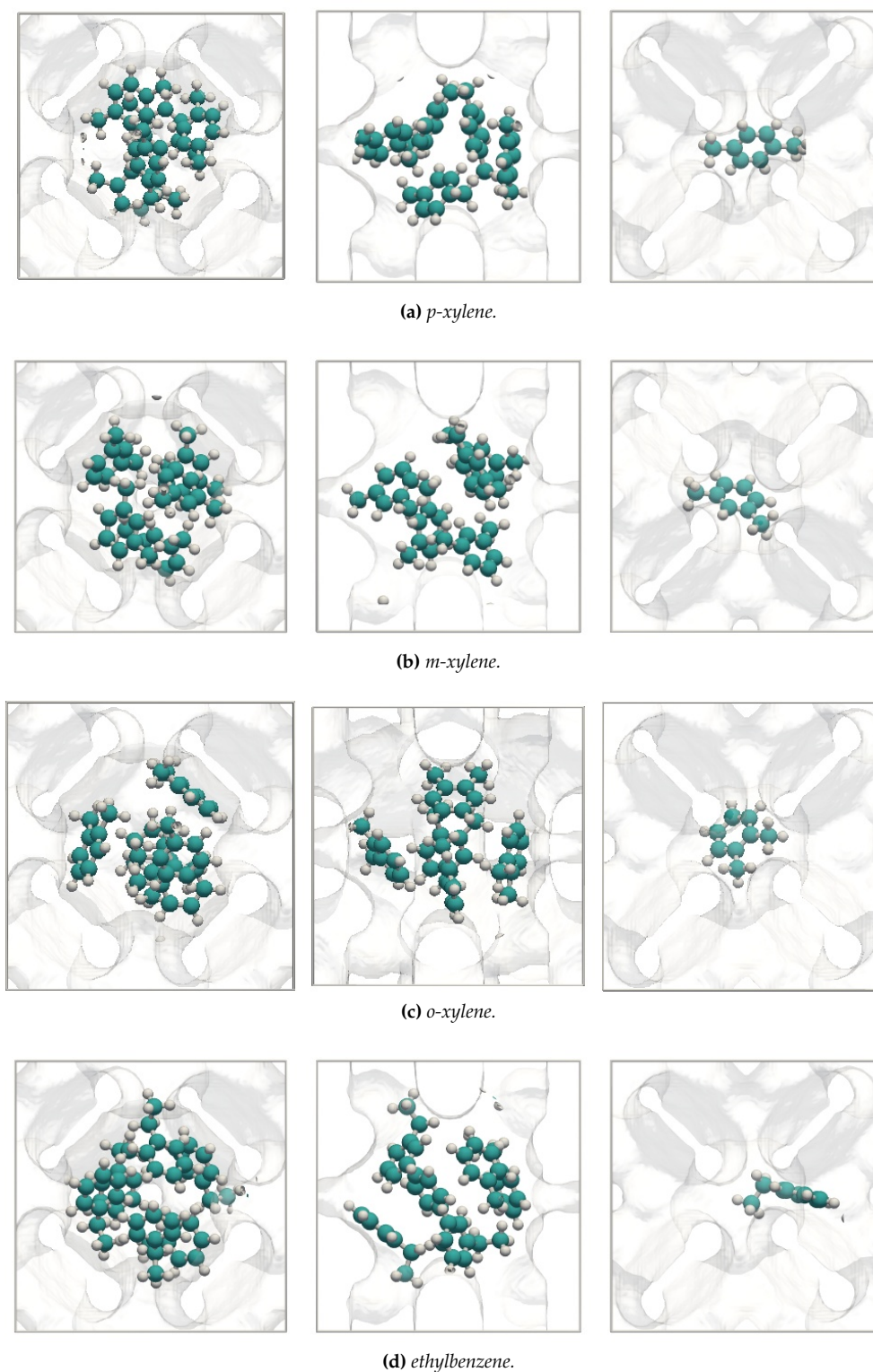


Figure S25: Snapshots of *p*-xylene, *o*-xylene, *m*-xylene, and ethylbenzene in MIL-125(Ti)-NH₂ at 1 kPa and 433 K. The tetrahedral cages in this case are even smaller than in MIL-125(Ti), this reduces the saturation value of the two bulkier isomers: *m*-xylene and *o*-xylene.

4.5.3 Langmuir-Freundlich parameters

	site A			site B		
	$q_{i,A,sat}$ [mol kg ⁻¹]	$b_{i,A}$ [Pa ^{-$v_{i,A}$}]	$v_{i,A}$ [-]	$q_{i,B,sat}$ [mol kg ⁻¹]	$b_{i,B}$ [Pa ^{-$v_{i,B}$}]	$v_{i,B}$ [-]
o-xylene	1.8	1.59×10^{-5}	0.62	2.9	1.5×10^{-4}	1.06
m-xylene	1.1	1.69×10^{-5}	0.68	3	9.98×10^{-5}	1.1
p-xylene	1.2	3.61×10^{-6}	0.87	3.3	8.33×10^{-5}	1.15
ethylbenzene	1.3	2.61×10^{-6}	0.9	3.1	8.02×10^{-5}	1.1
benzene	5.3	5.42×10^{-6}	1.1	1.1	4.79×10^{-6}	0.7
toluene	1.3	2.01×10^{-5}	0.7	4.1	2.12×10^{-5}	1.1

Table S8: Dual-site Langmuir-Freundlich parameters for pure component xylene isomers at 433 K in MIL-125(Ti)-NH₂.

4.5.4 Adsorption isotherms

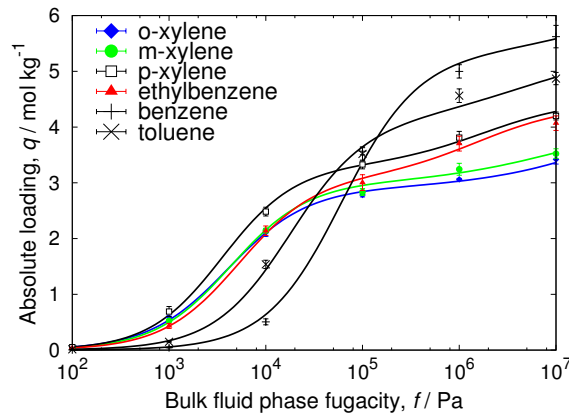
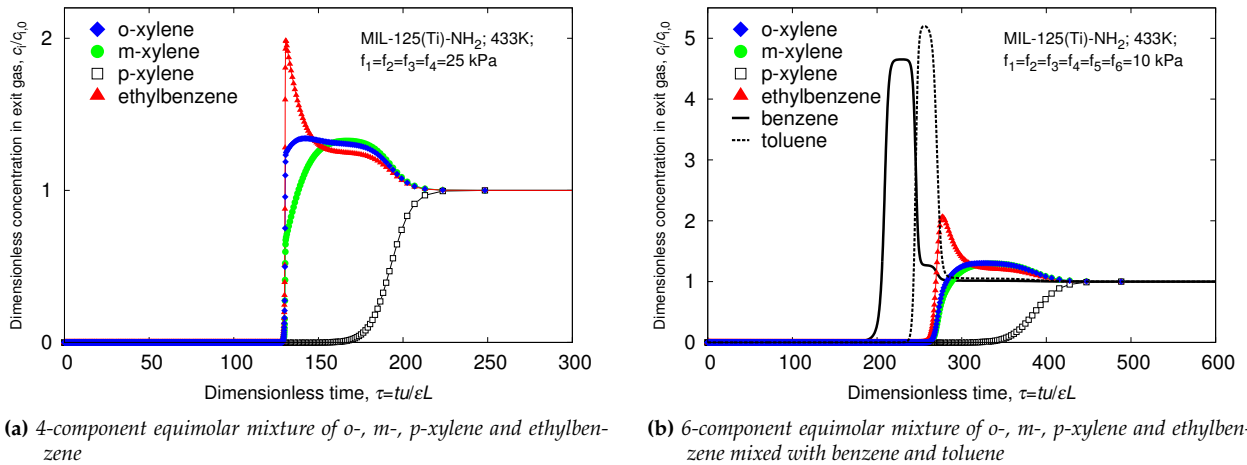


Figure S26: Pure component isotherms of xylene isomers (lines are dual-site Langmuir-Freundlich fits of the pure components, points are the pure component isotherms from CFMC simulations).



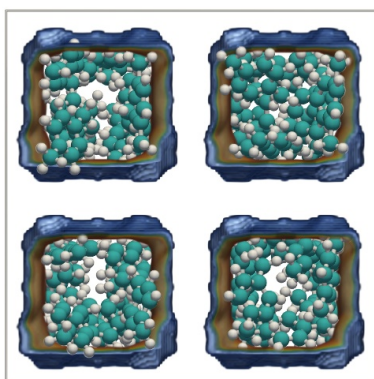
(a) 4-component equimolar mixture of o-, m-, p-xylene and ethylbenzene

(b) 6-component equimolar mixture of o-, m-, p-xylene and ethylbenzene mixed with benzene and toluene

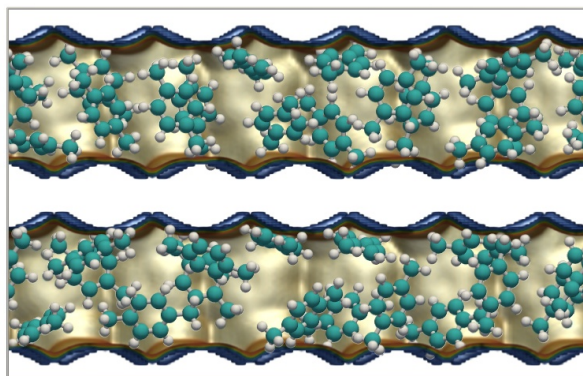
Figure S27: Simulated step-type breakthrough of xylene isomers in MIL-125(Ti)-NH₂ at 433K. Video animations of the breakthrough behavior as a function of time are provided as Supplementary information.

4.6 CoBDP

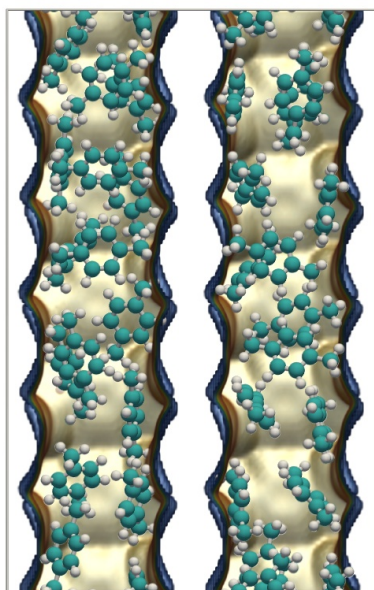
4.6.1 Energy landscapes



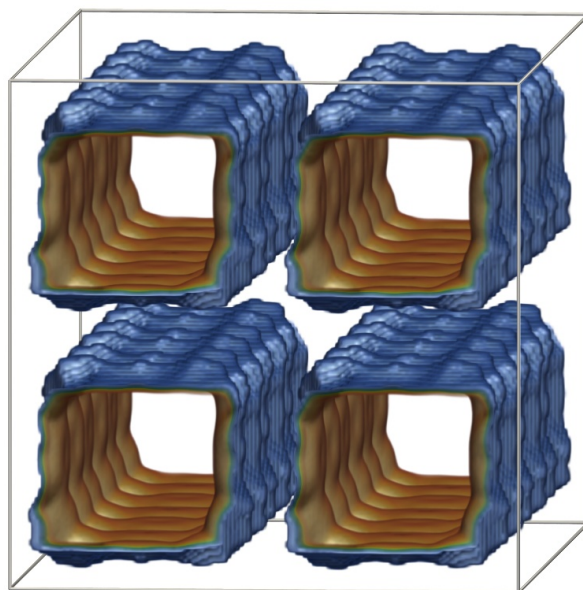
(a) CoBDP ($2 \times 2 \times 3$); XY-view.



(b) CoBDP ($2 \times 2 \times 3$); XZ-view



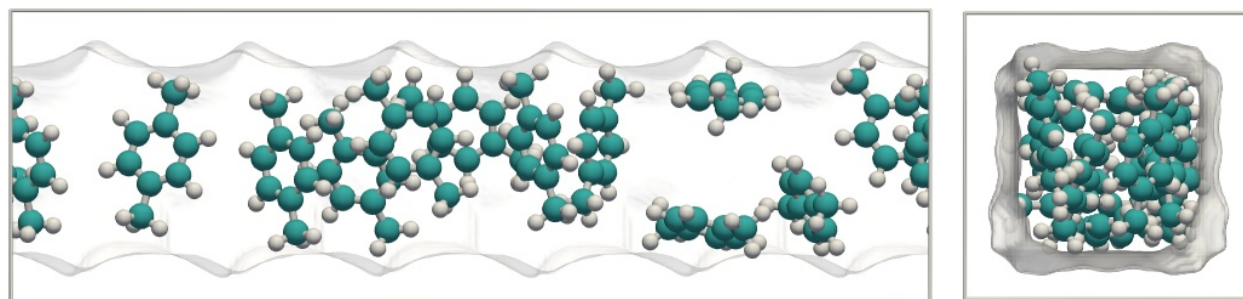
(c) CoBDP ($2 \times 2 \times 3$); YZ-view



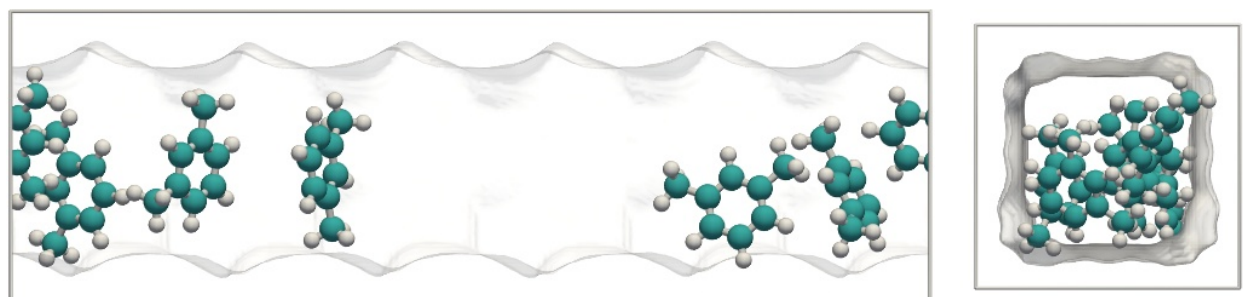
(d) CoBDP ($2 \times 2 \times 3$); XYZ-view

Figure S28: Energy landscape of a system of $2 \times 2 \times 3$ CoBDP unit cells. The CoBDP unit cell has edge lengths $a = 13.253 \text{ \AA}$, $b = 13.253 \text{ \AA}$, and $c = 13.995 \text{ \AA}$, with cell angles $\alpha = \beta = \gamma = 90^\circ$. The CoBDP pore system consists of rectangular channels running in the c -direction. About 65% of the structure is void. Shown adsorbates: p -xylene at 1 kPa and 433K. Color code: carbon (cyan), hydrogen (white).

4.6.2 Snapshots



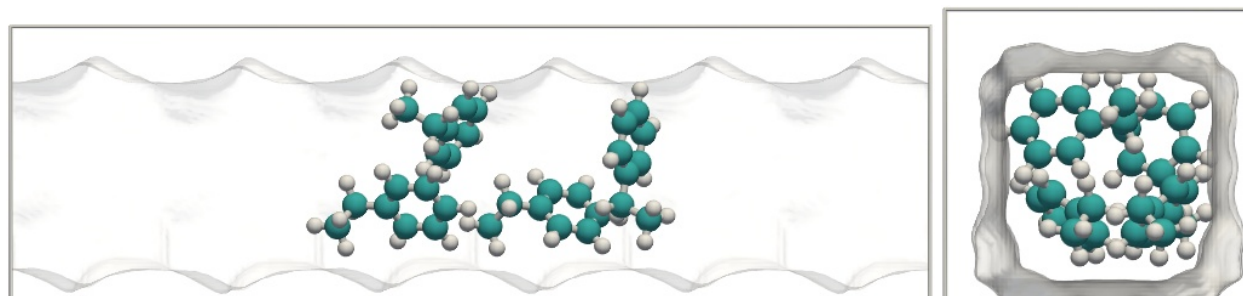
(a) *p*-xylene.



(b) *m*-xylene.



(c) *o*-xylene.



(d) ethylbenzene.

Figure S29: Snapshots of *p*-xylene, *o*-xylene, *m*-xylene, and ethylbenzene in CoBDP at 2626 Pa and 433 K. The channel dimension is such that *p*-xylene is able to stack perpendicular to the channel direction aligned from wall to wall. Color code: carbon (cyan), hydrogen (white).

4.6.3 Langmuir-Freundlich parameters

	site A			site B		
	$q_{i,A,sat}$ [molec. uc ⁻¹]	$b_{i,A}$ [Pa ^{-$v_{i,A}$]}	$v_{i,A}$ [-]	$q_{i,B,sat}$ [molec. uc ⁻¹]	$b_{i,B}$ [Pa ^{-$v_{i,B}$]}	$v_{i,B}$ [-]
o-xylene	4.8	1.28×10^{-5}	1.4	1.5	1.6×10^{-4}	0.7
m-xylene	4.8	3.19×10^{-5}	1.27	1.2	4.72×10^{-5}	0.7
p-xylene	4.5	2.3×10^{-6}	1.7	1.6	1.46×10^{-4}	0.7
ethylbenzene	4.5	7.38×10^{-6}	1.5	1.4	1.6×10^{-4}	0.7
benzene	2.3	3.95×10^{-15}	3.3	5.4	9.5×10^{-6}	1.05
toluene	5.4	2.84×10^{-6}	1.4	2	4.46×10^{-5}	0.7

Table S9: Dual-site Langmuir-Freundlich parameters for pure component xylene isomers at 433 K in CoBDP. The saturation capacities are expressed in molecules per unit cell; these numbers need to be multiplied by the conversion factor of 0.935796.

4.6.4 Adsorption isotherms

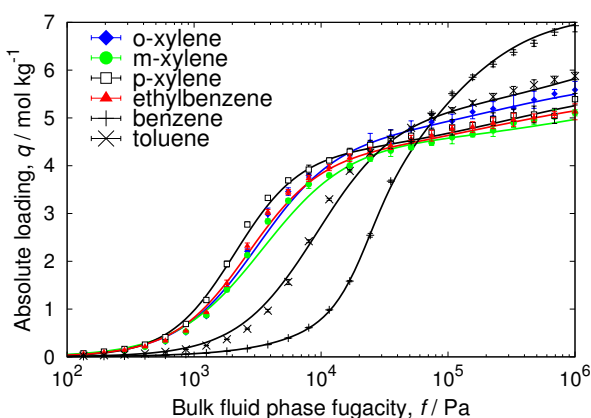
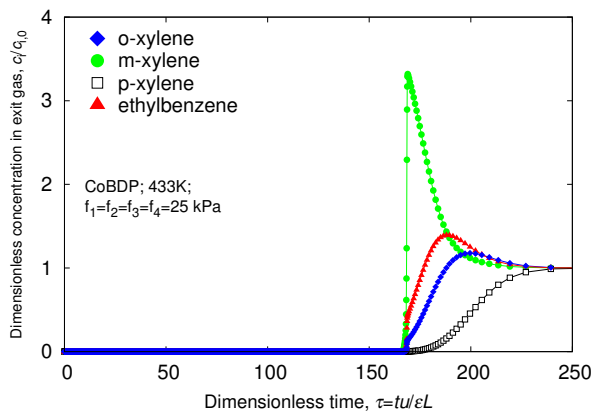
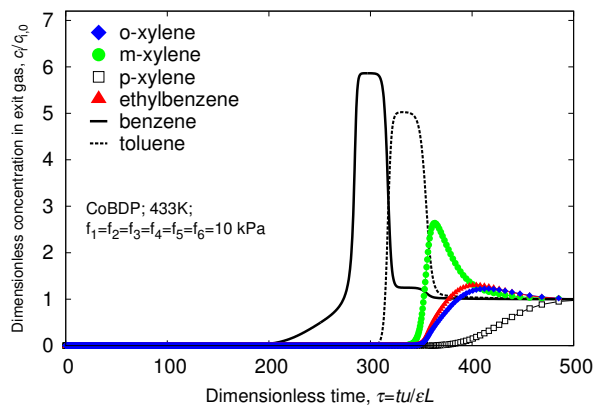


Figure S30: Pure component isotherms of xylene isomers (lines are dual-site Langmuir-Freundlich fits of the pure components, points are the pure component isotherms from CBMC simulations).

4.6.5 Breakthrough simulations



(a) 4-component equimolar mixture of o-, m-, p-xylene and ethylbenzene

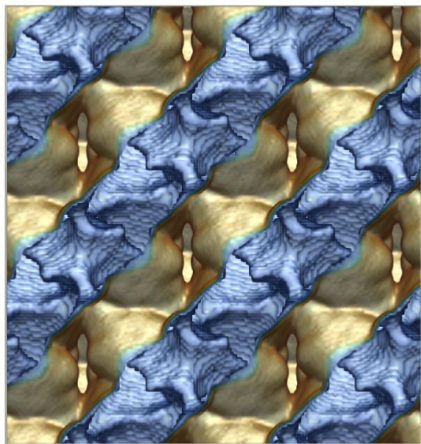


(b) 6-component equimolar mixture of o-, m-, p-xylene and ethylbenzene mixed with benzene and toluene

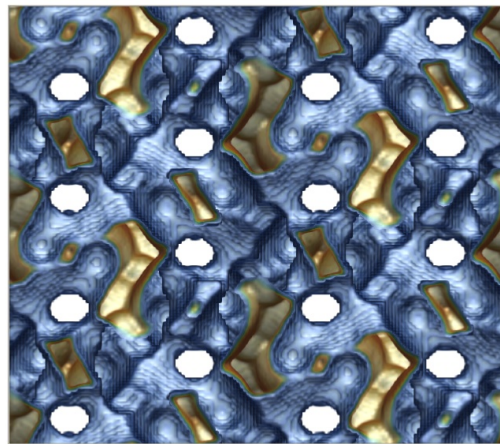
Figure S31: Simulated step-type breakthrough of xylene isomers in CoBDP at 433K. Video animations of the breakthrough behavior as a function of time are provided as Supplementary information.

4.7 JUC-77

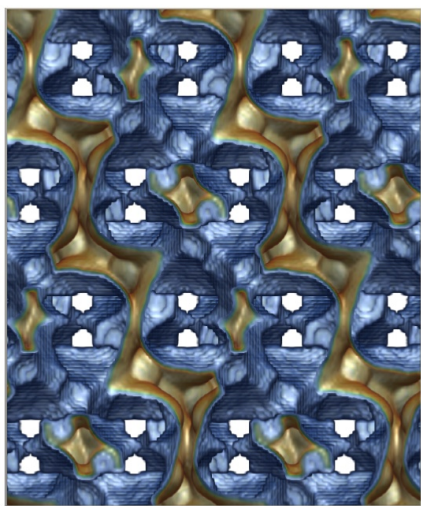
4.7.1 Energy landscapes



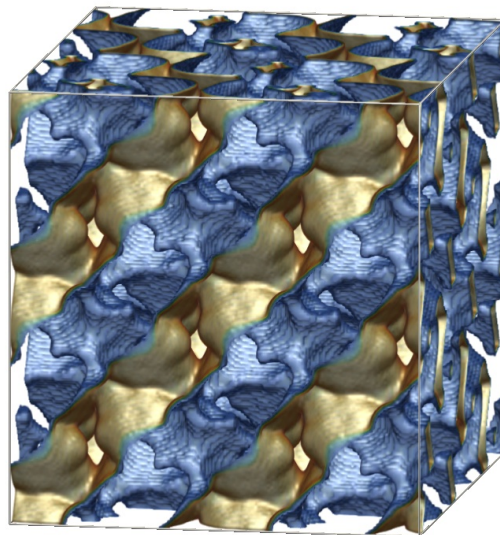
(a) JUC-77 ($2 \times 2 \times 2$); XY-view.



(b) JUC-77 ($2 \times 2 \times 2$); XZ-view



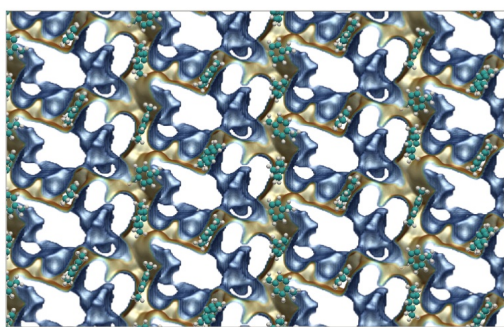
(c) JUC-77 ($2 \times 2 \times 2$); YZ-view



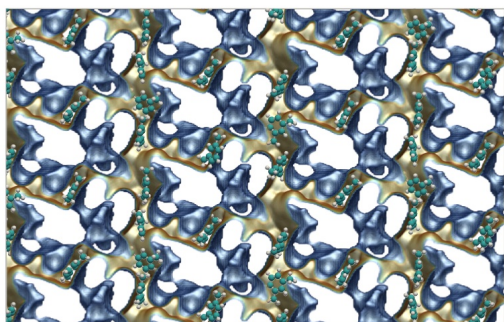
(d) JUC-77 ($2 \times 2 \times 2$); XYZ-view

Figure S32: Energy landscape of a system of $2 \times 2 \times 2$ JUC-77 unit cells. The JUC-77 unit cell has edge lengths $a = 19.2396 \text{ \AA}$, $b = 20.3017 \text{ \AA}$, and $c = 46.143 \text{ \AA}$, with cell angles $\alpha = \beta = \gamma = 90^\circ$.

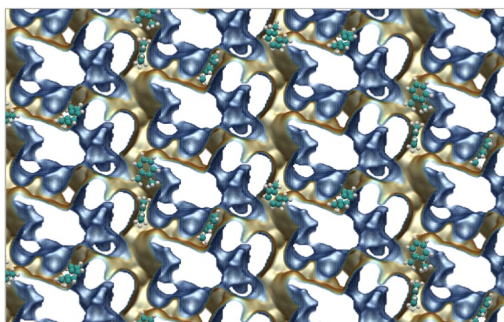
4.7.2 Snapshots



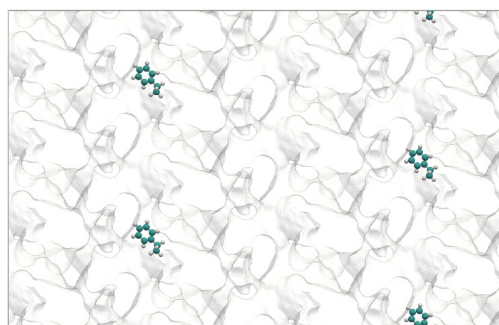
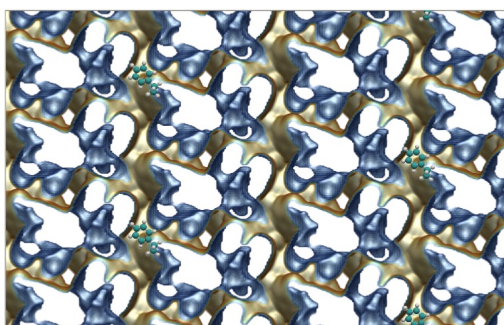
(a) *p*-xylene.



(b) *m*-xylene.



(c) *o*-xylene.



(d) ethylbenzene.

Figure S33: Snapshots of *p*-xylene, *o*-xylene, *m*-xylene, and ethylbenzene in JUC-77 at 100 Pa and 433 K. Color code: carbon (cyan), hydrogen (white).

4.7.3 Langmuir-Freundlich parameters

	site A			site B		
	$q_{i,A,sat}$ [mol kg ⁻¹]	$b_{i,A}$ [Pa ^{-$v_{i,A}$}]	$v_{i,A}$ [-]	$q_{i,B,sat}$ [mol kg ⁻¹]	$b_{i,B}$ [Pa ^{-$v_{i,B}$}]	$v_{i,B}$ [-]
o-xylene	0.4	2.4×10^{-3}	0.8	0.9	2.01×10^{-2}	1
m-xylene	0.53	1.24×10^{-2}	0.822	0.77	3.1×10^{-2}	1.1
p-xylene	0.6	1.24×10^{-2}	0.9	0.7	3.14×10^{-2}	1.05
ethylbenzene	0.4	7.02×10^{-4}	0.9	0.9	2.98×10^{-3}	1.2
benzene	1.7	1.79×10^{-5}	0.9	1.2	3.78×10^{-4}	1
toluene	1.6	6.83×10^{-6}	0.8	1.2	8.18×10^{-4}	1.2

Table S10: Dual-site Langmuir-Freundlich parameters for pure component xylene isomers at 433 K in JUC-77.

4.7.4 Adsorption isotherms

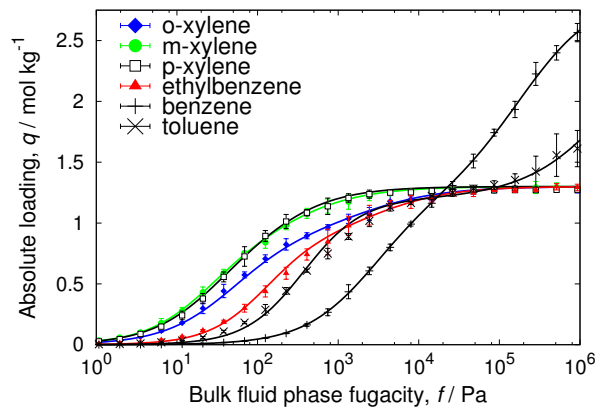
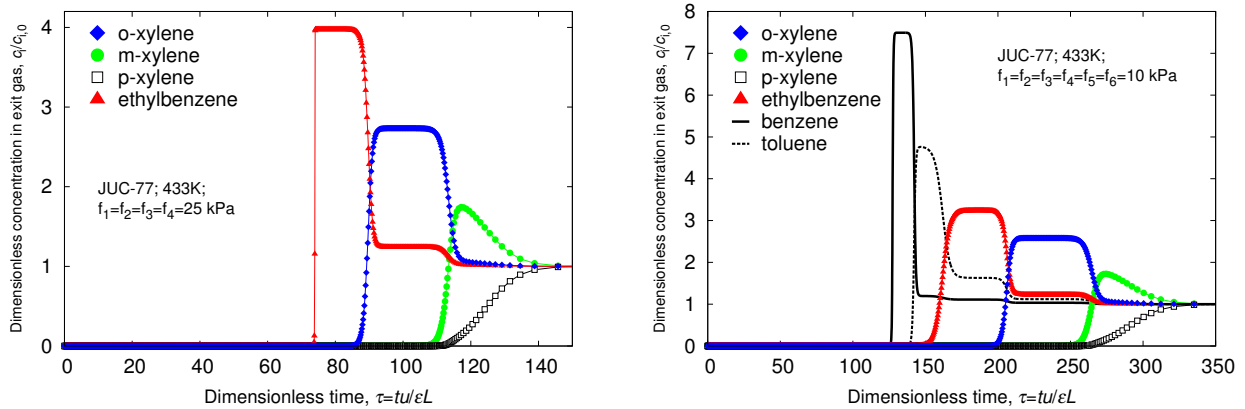


Figure S34: Pure component isotherms of xylene isomers (lines are dual-site Langmuir-Freundlich fits of the pure components, points are the pure component isotherms from CBMC simulations).



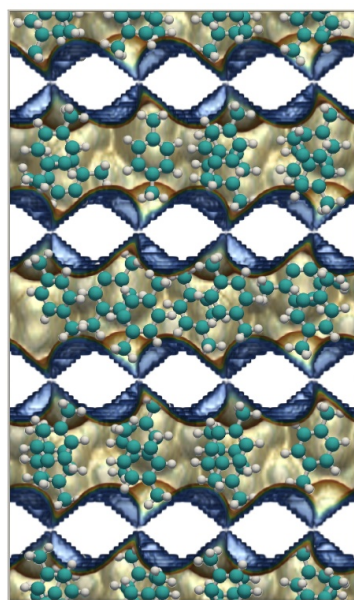
(a) 4-component equimolar mixture of o-, m-, p-xylene and ethylbenzene

(b) 6-component equimolar mixture of o-, m-, p-xylene and ethylbenzene mixed with benzene and toluene

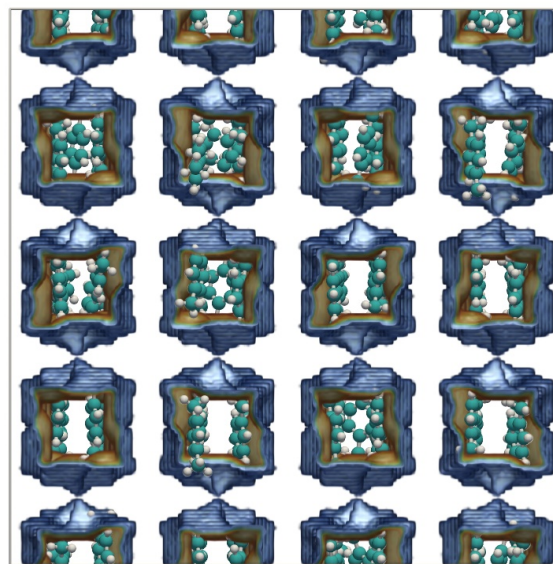
Figure S35: Simulated step-type breakthrough of xylene isomers in JUC-77 at 433K. Video animations of the breakthrough behavior as a function of time are provided as Supplementary information.

4.8 MAF-X8

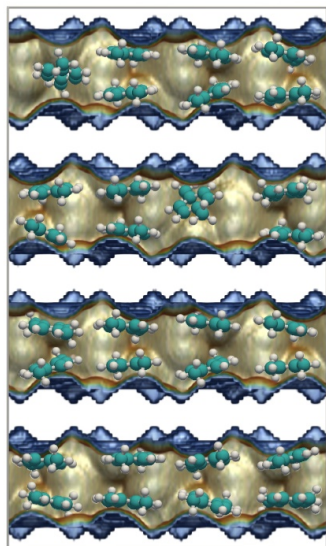
4.8.1 Energy landscapes



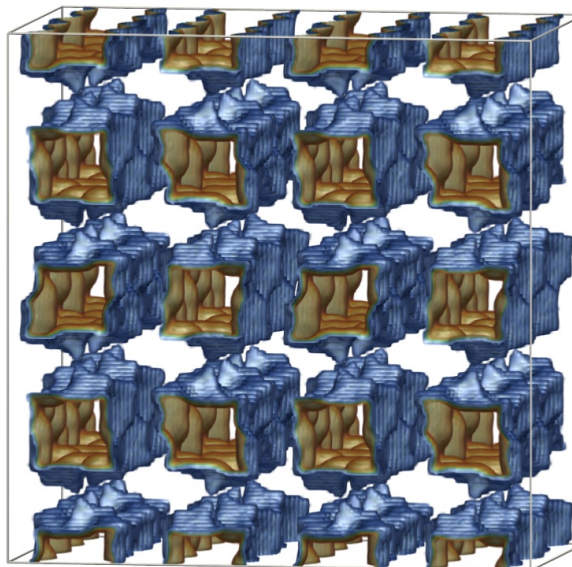
(a) MAF-X8 ($2 \times 2 \times 2$); XY-view.



(b) MAF-X8 ($2 \times 2 \times 2$); XZ-view



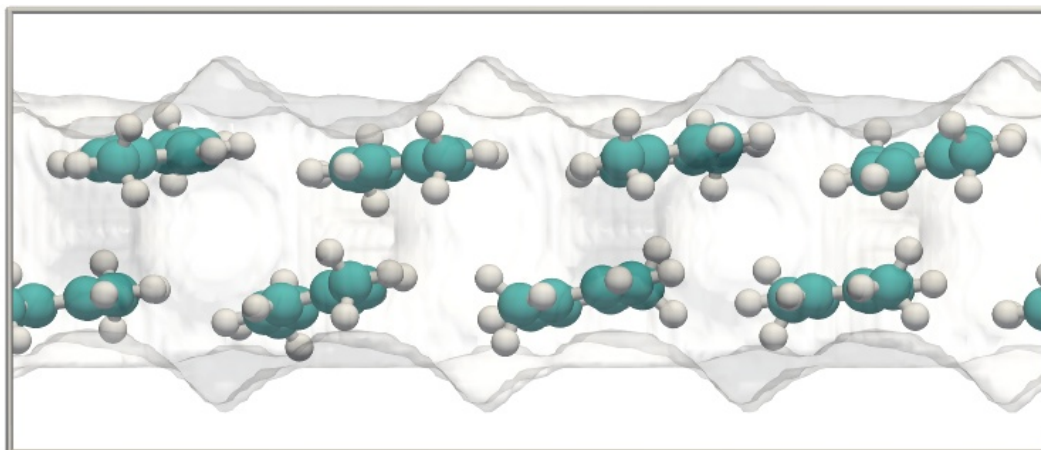
(c) MAF-X8 ($2 \times 2 \times 2$); YZ-view



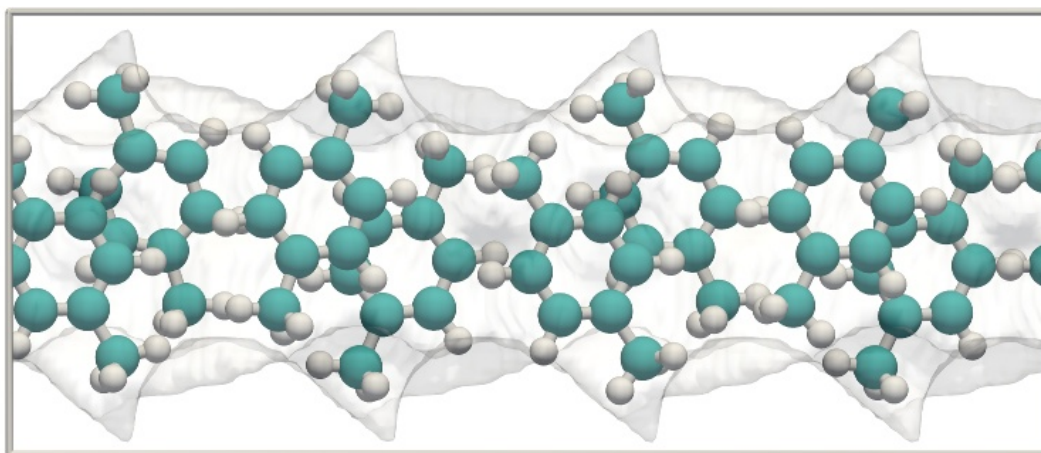
(d) MAF-X8 ($2 \times 2 \times 2$); XYZ-view

Figure S36: Energy landscape of a system of $2 \times 2 \times 2$ MAF-X8 unit cells. The MAF-X8 unit cell has edge lengths $a = 13.9249 \text{ \AA}$, $b = 23.653 \text{ \AA}$, and $c = 23.637 \text{ \AA}$, with cell angles $\alpha = \beta = \gamma = 90^\circ$. The MAF-X8 pore system consists of rectangular channels running in the a -direction. About 49% of the structure is void. Shown adsorbates: *p*-xylene at 1 kPa and 433K. Color code: carbon (cyan), hydrogen (white).

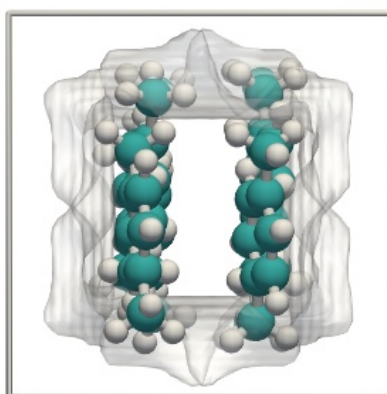
4.8.2 Stacking of p-xylene in MAF-X8



(a) top view.



(b) side view.



(c) parallel channel view

Figure S37: Stacking of p-xylene in MAF-X8. The molecule are stacked in an alternating fashion. Para-xylene is able to make efficiently use of the space available in the MAF-X8 structure. The molecule is adsorbed at the wall but able to stack from wall to opposite wall. Color code: carbon (cyan), hydrogen (white).

4.8.3 Stacking of p-xylene in MAF-X8: schematic snapshots

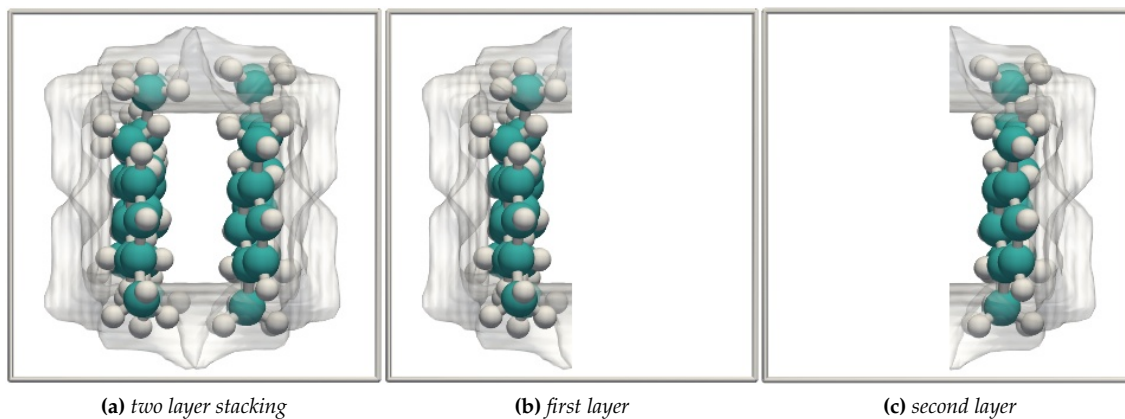


Figure S38: The xylenes stacks in two layers adsorbed at the “left” and “right” walls of the (approximately) rectangular channels. The channel width-dimensions is such that the two layers are formed consisting of pairs of xylenes. The height- and length-dimensions of MAF-X8 are most commensurate with p-xylene.

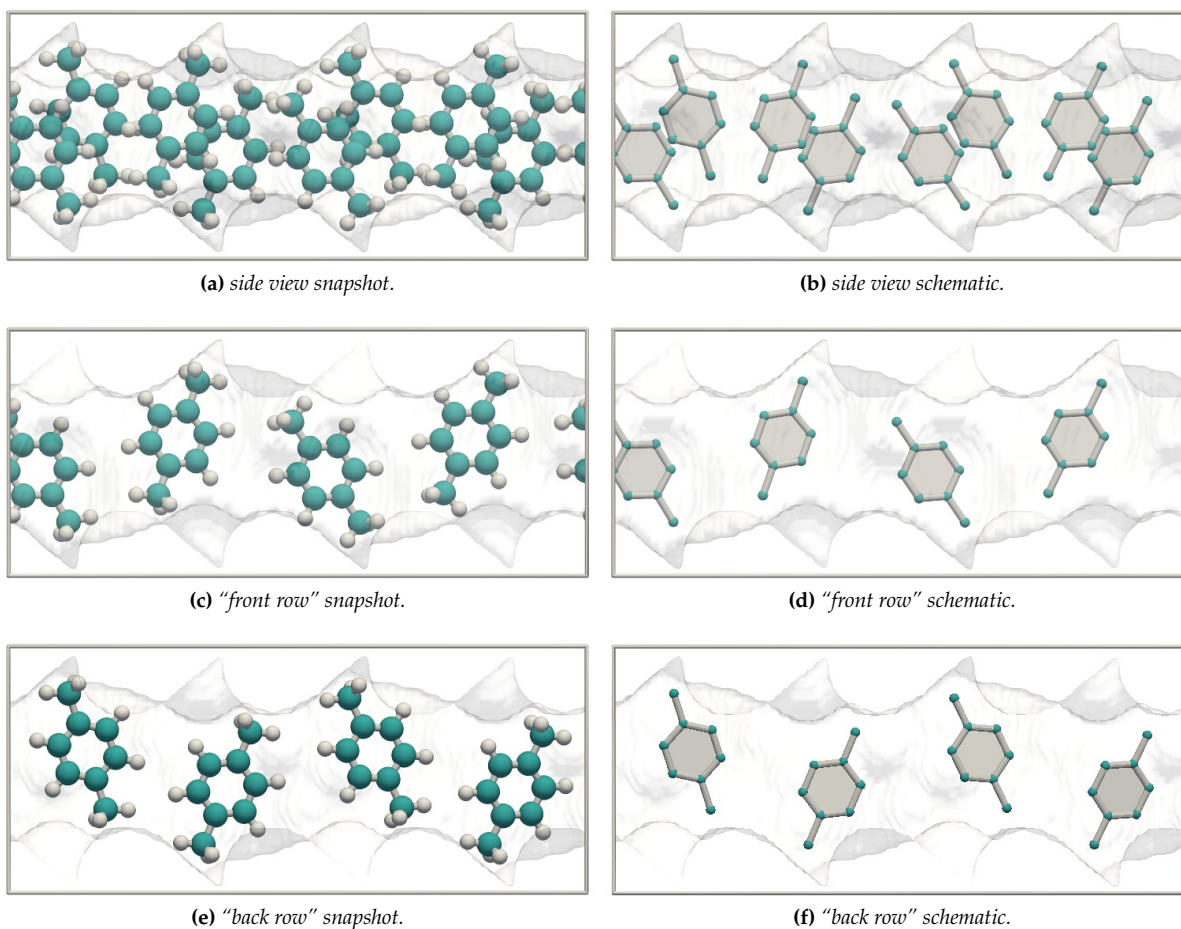
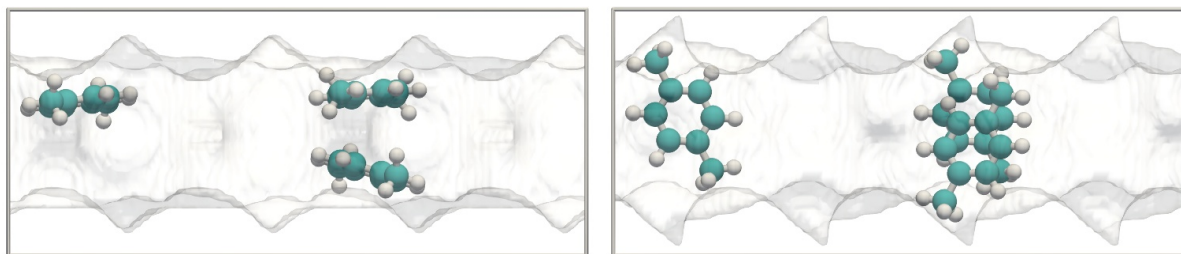
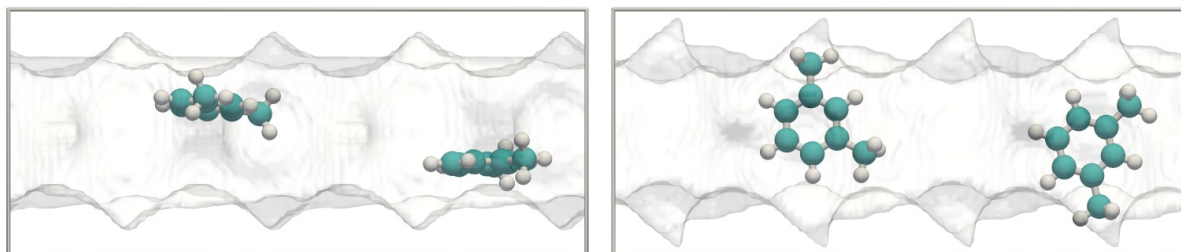


Figure S39: Side view of the two layer stacking of p-xylene in MAF-X8: left figures are snapshots from CBMC simulations, right figures are schematic representations with the hydrogens removed. Color code: carbon (cyan), hydrogen (white).

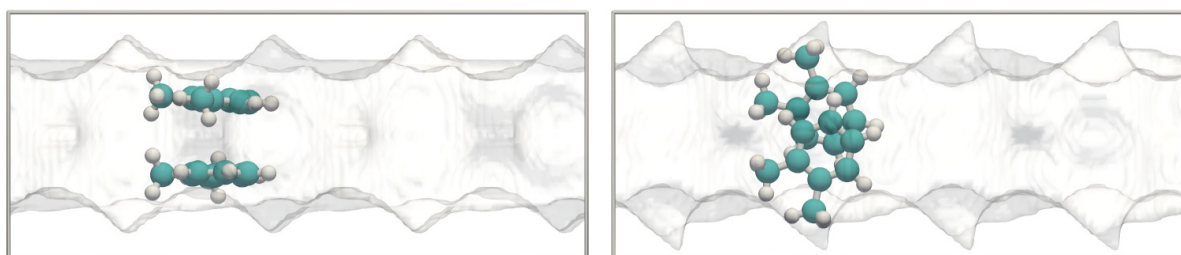
4.8.4 Snapshots at low loading



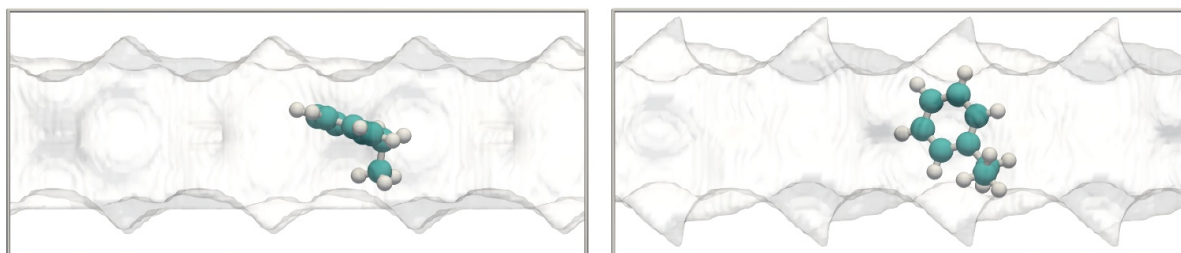
(a) *p*-xylene.



(b) *m*-xylene.



(c) *o*-xylene.



(d) ethylbenzene.

Figure S40: Snapshots of *p*-xylene, *m*-xylene, *o*-xylene, and ethylbenzene in MAF-X8 at 10^{-6} Pa and 433 K. Color code: carbon (cyan), hydrogen (white).

4.8.5 Snapshots at saturation loading

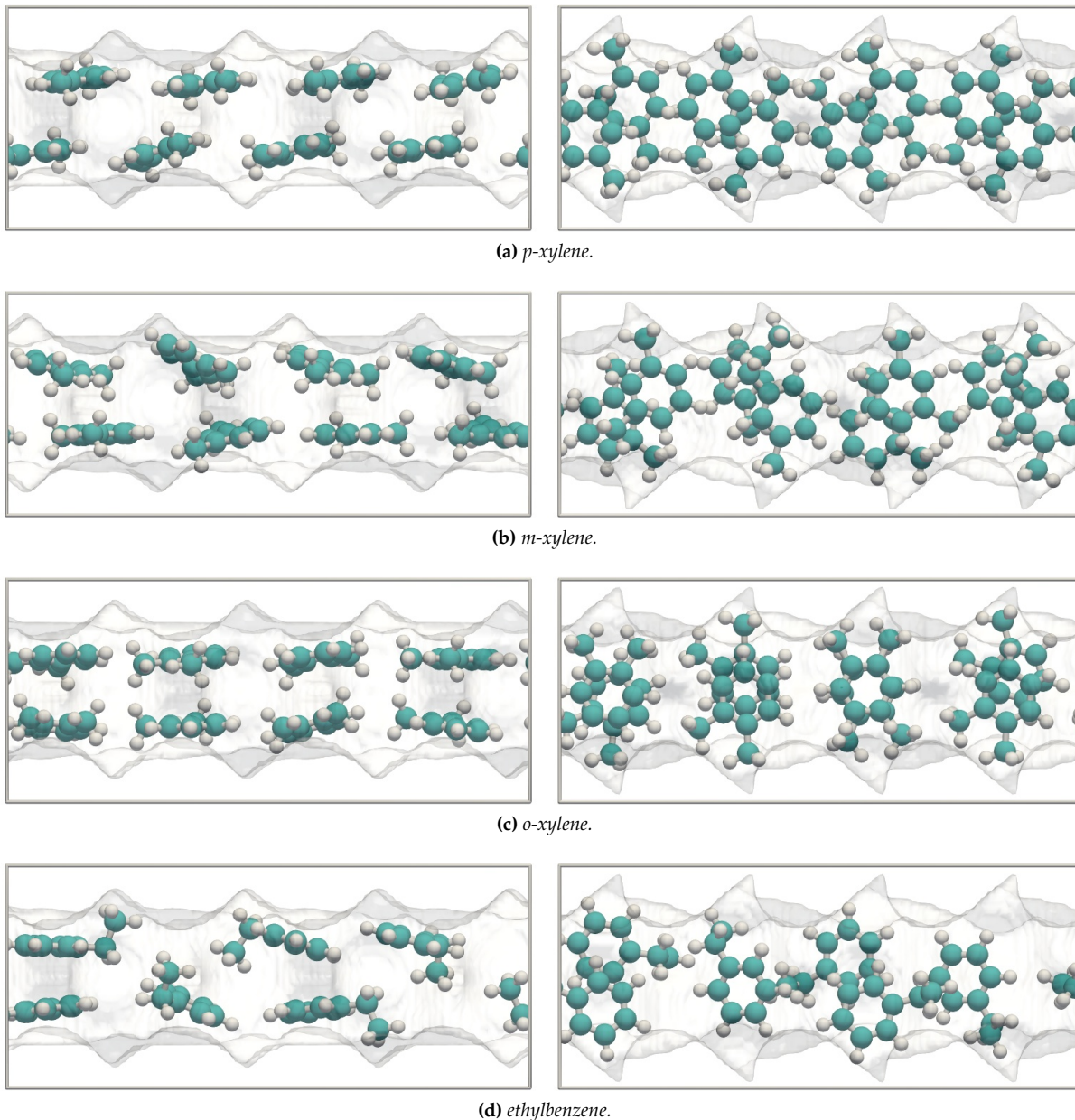


Figure S41: Snapshots of *p*-xylene, *m*-xylene, *o*-xylene, and ethylbenzene in MAF-X8 at 10^6 Pa and 433 K. The saturation loading of *p*-xylene, *m*-xylene, and *o*-xylene is the same (for the shown channel-section the maximum loading is 8 molecules). The saturation loading of ethylbenzene is lower than *p*-, *m*-, *o*-xylene, because it can not stack in the same way. Note that *p*-xylene alternates, while *m*-, and *o*-xylene are facing each other. The *p*-xylene molecule is able to stack more efficiently with less repulsion between the molecules. Color code: carbon (cyan), hydrogen (white).

4.8.6 Langmuir-Freundlich parameters

	site A			site B		
	$q_{i,A,sat}$ [mol kg ⁻¹]	$b_{i,A}$ [Pa ^{-$\nu_{i,A}$}]	$\nu_{i,A}$ [-]	$q_{i,B,sat}$ [mol kg ⁻¹]	$b_{i,B}$ [Pa ^{-$\nu_{i,B}$}]	$\nu_{i,B}$ [-]
o-xylene	1.55	1.33	0.42	1.75	5.72×10^6	1.1
m-xylene	1.4	1.24×10^1	0.6	1.85	2.24×10^6	1.06
p-xylene	1.55	1.33×10^1	0.54	1.75	5.12×10^7	1.2
ethylbenzene	1.4	11	0.74	1.3	3.76×10^4	1
benzene	3.4	5.48×10^{-2}	0.3	1.8	1.75×10^2	1
toluene	1.8	6.95×10^{-1}	0.5	1.8	1.31×10^4	1

Table S11: Dual-site Langmuir-Freundlich parameters for pure component xylene isomers at 433 K in MAF-X8.

4.8.7 Adsorption isotherms

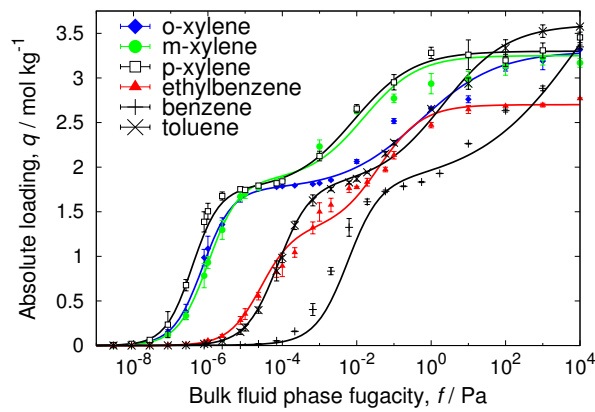
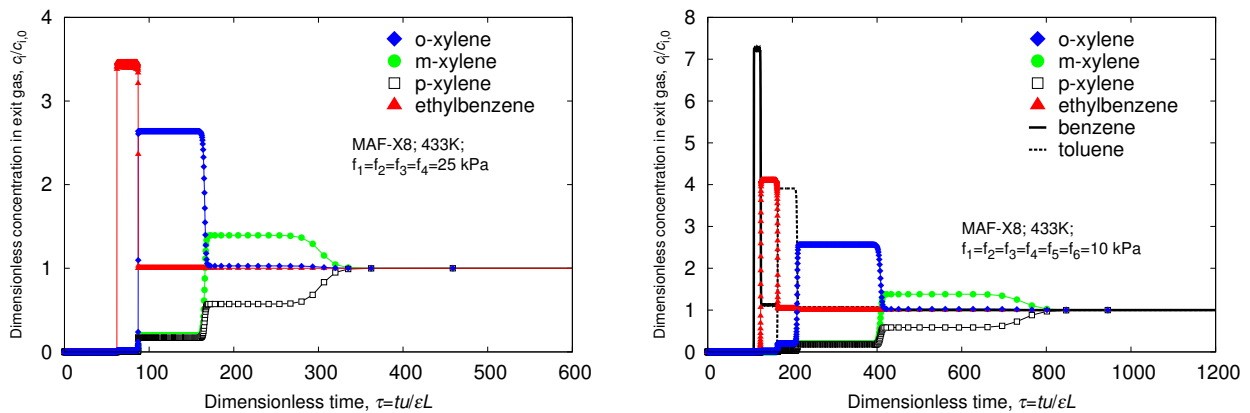


Figure S42: Pure component isotherms of xylene isomers (lines are dual-site Langmuir-Freundlich fits of the pure components, points are the pure component isotherms from CBMC simulations).

4.8.8 Breakthrough simulations



(a) 4-component equimolar mixture of o-, m-, p-xylene and ethylbenzene

(b) 6-component equimolar mixture of o-, m-, p-xylene and ethylbenzene mixed with benzene and toluene

Figure S43: Simulated step-type breakthrough of xylene isomers in MAF-X8 at 433K. Video animations of the breakthrough behavior as a function of time are provided as Supplementary information.

5

Influence of saturation capacities on separations in fixed bed adsorbers

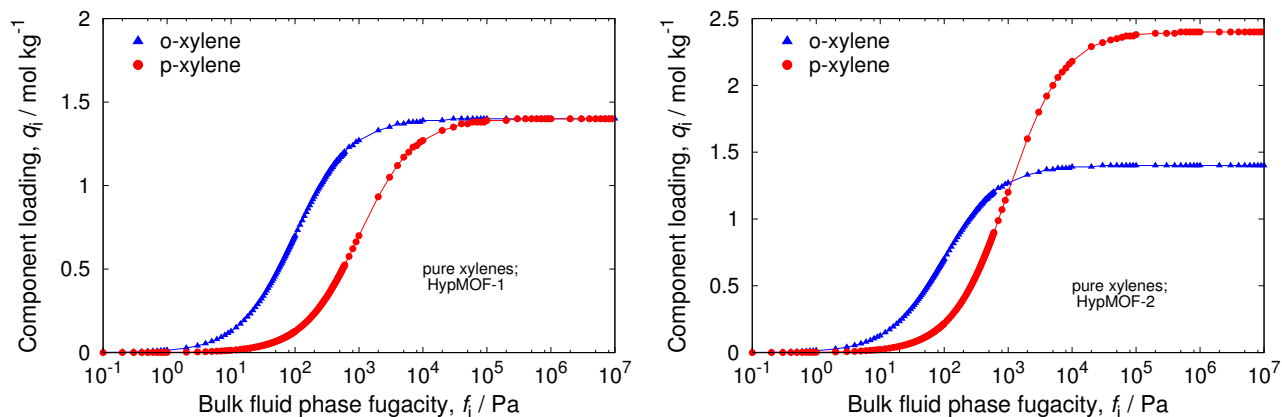
The separation of C8 hydrocarbons using MAF-X8 is strongly dictated by the significantly higher saturation capacity for p-xylene as a result of commensurate stacking. In order to illustrate the strong influence of differences in saturation capacities on the separation performance we present breakthrough calculations for a mixture of o-xylene and p-xylene using two hypothetical MOFs: HypMOF-1, and HypMOF-2. For illustration purposes we take the adsorption isotherms to be represented by 1-site Langmuir isotherms

$$q = q_{sat} \frac{bp}{1 + bp} \quad (5.1)$$

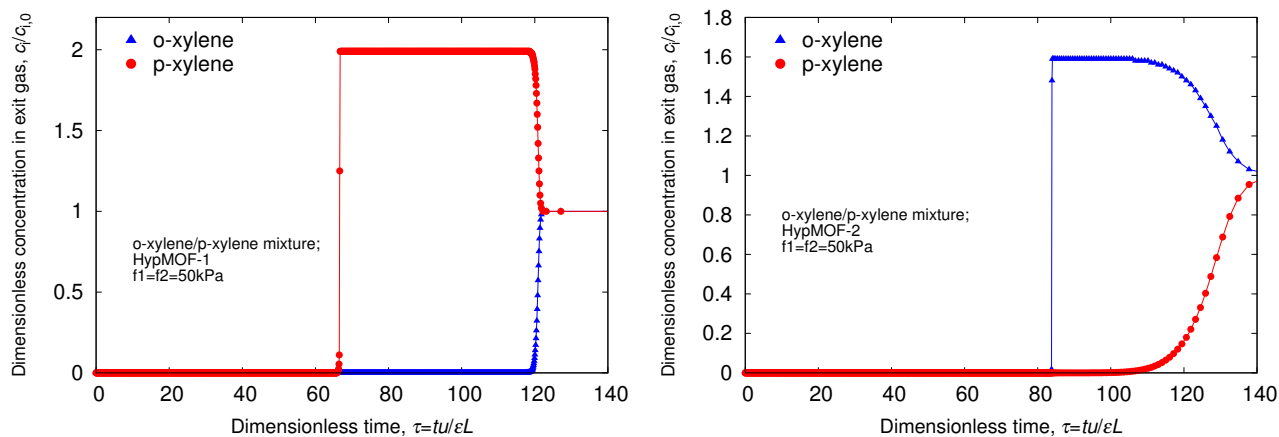
For HypMOF-1, we assume that the saturation capacities of o-xylene and p-xylene are identical, but the adsorption strength is strongly in favor of o-xylene; see Table S12. The isotherms are compared in S44 a. For HypMOF-2, the Langmuir parameter b are the same as for HypMOF-1, but in this case the saturation capacity of p-xylene is assumed to be significantly higher than that of o-xylene.

Hypothetical MOF	molecule	q_{sat} [mol kg ⁻¹]	b [Pa ⁻¹]
HypMOF-1	o-xylene	1.4	1×10^{-2}
	p-xylene	1.4	1×10^{-3}
HypMOF-2	o-xylene	1.4	1×10^{-2}
	p-xylene	2.4	1×10^{-3}

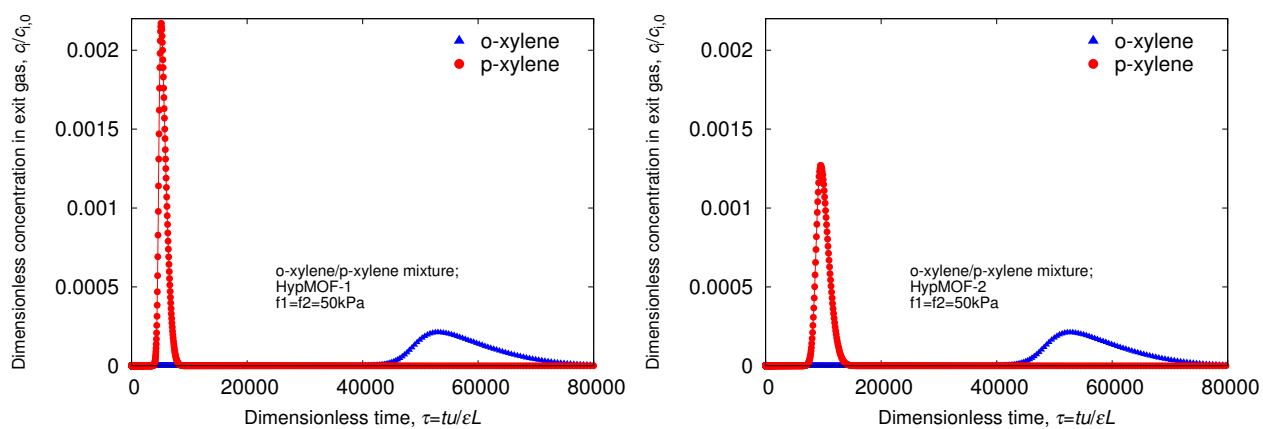
Table S12: Langmuir-Freundlich parameters for o-xylene and p-xylene in HypMOF-1 and HypMOF-2 at 433 K.



(a) Single component isotherms of *ortho* and *para*-xylene in hypothetical MOFs



(b) Step-type breakthrough curves for an equimolar mixture of *ortho* and *para*-xylene in hypothetical MOFs at 50kPa.



(c) Pulse-type breakthrough curves for an equimolar mixture of *ortho* and *para*-xylene in hypothetical MOFs at 50kPa.

Figure S44: Effect of saturation capacity in breakthrough curves.

6

Comparison of p-Selective Adsorbents

We have identified a few materials Co(BDP), MIL-125(Ti), MIL-125(Ti)-NH₂, JUC-77 and MAF-X8 that have the desired selectivity towards p-xylene. We now compare the performance of each of these MOFs against BaX, that is currently used in industrial practice. Let us first compare the adsorption selectivity and capacity metrics.

For a binary mixture the adsorption selectivity is defined as follows

$$S_{\text{ads}} = \frac{q_1/q_2}{f_1/f_2} \quad (6.1)$$

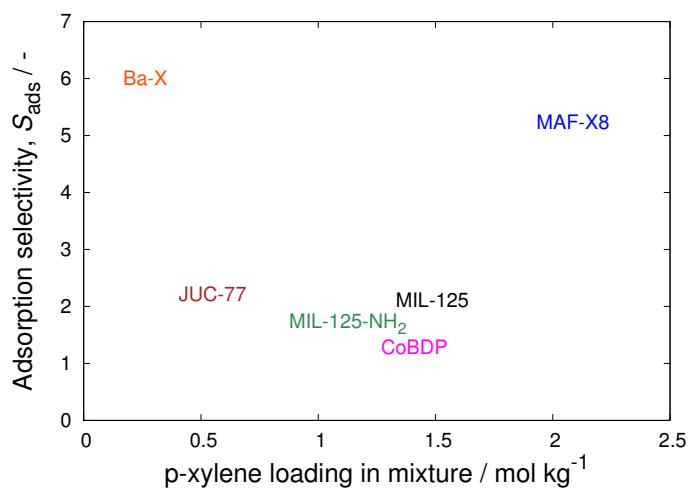
For most of the MOFs, the component to breakthrough before p-xylene is either m-xylene or p-xylene. Consequently, for separation of 4-component o-xylene(1)/m-xylene(2)/p-xylene(3)/ethylbenzene(4) mixtures we adopt the following definition of selectivity

$$S_{\text{ads}} = \frac{q_3/(q_1 + q_2 + q_4)}{f_3/(f_1 + f_2 + f_4)} = 3 \frac{q_3}{q_1 + q_2 + q_4} \quad (6.2)$$

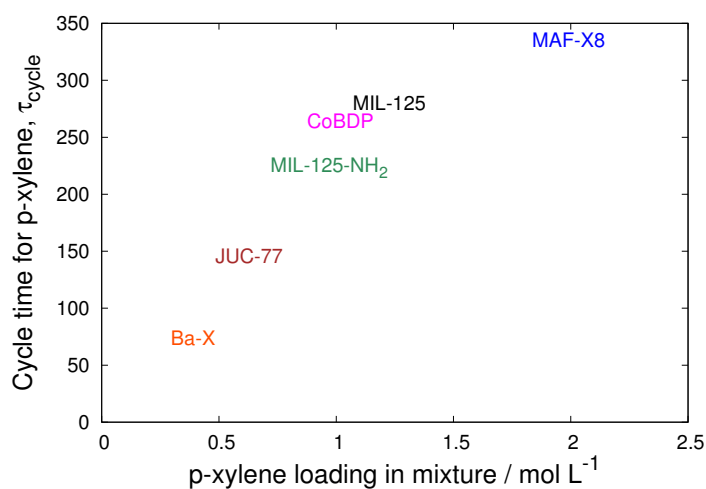
The Capacity is defined as the p-xylene loading in the adsorbed phase of a four-component mixture.

$$\text{Capacity} = q_3 \quad (6.3)$$

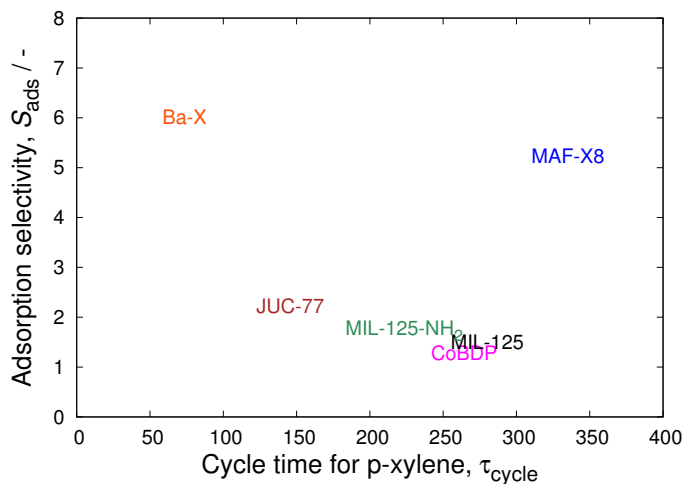
Note that q_3 is the molar loading expressed as kg of p-xylene in adsorbed phase per kg of MOF. Both the metrics are determined for a total operating pressure of 100 kPa; the results are presented in Figure S45a. We note that MAF-X8 has nearly the same adsorption selectivity as BaX, but has a significantly higher capacity to adsorb p-xylene. All other MOFs appear to be significantly poorer in selectivity as compared to BaX and MAF-X8. The other MOFs are also lower in p-xylene adsorption capacity. The separation performance of a fixed bed adsorber is dictated by both adsorption selectivity and capacity. A higher capacity to adsorb p-xylene leads to a longer breakthrough time that is desirable because of this requires less frequent regeneration. In view of the distended characteristics of several of the breakthroughs, we define the cycle time for p-xylene as the dimensionless time, τ_{cycle} , at which the concentration of the gas at the outlet is 99% of the value at the inlet. Figure S45b shows that the dimensionless p-xylene cycle time τ_{cycle} is approximately linearly dependent on the loading of p-xylene in the mixture expressed in mol of p-xylene per L of MOF. We use the volumetric capacity, obtained by multiplying q_3 by the framework density, for the plot in Figure S45b because the breakthrough simulations are compared on the basis of equal volume of MOFs packed into a fixed bed. The cycle time for p-xylene in MAF-X8 is 335.2, as compared to 73.683 with BaX. This implies that a fixed bed of BaX would require regeneration about 4.5 times more frequently than with MAF-X8. On the basis of the information presented in Figure S45, we reach the unequivocal conclusion that MAF-X8 is the best adsorbent for use in industry, with significantly improved separation performance as compared to BaX.



(a)



(b)



(c)

Figure S45: Comparison of *p*-selective adsorbents. All breakthrough simulations do not include diffusion. Inclusion of diffusional effects will significantly diminish the performance of JUC-77, MIL-125(Ti), MIL-125(Ti)-NH₂. CoBDP, MAF-X8, and BaX are not significantly influenced by diffusion.

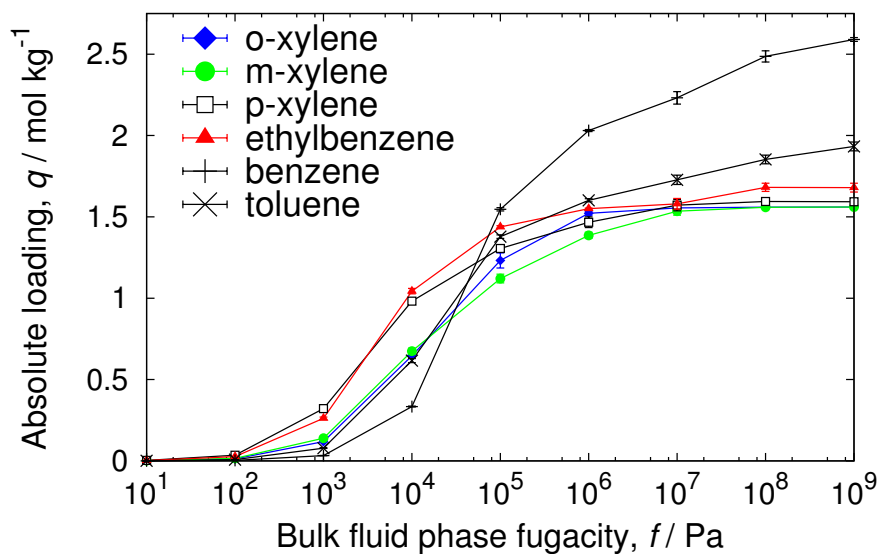
7

Screening of Potential Zeolite Adsorbents

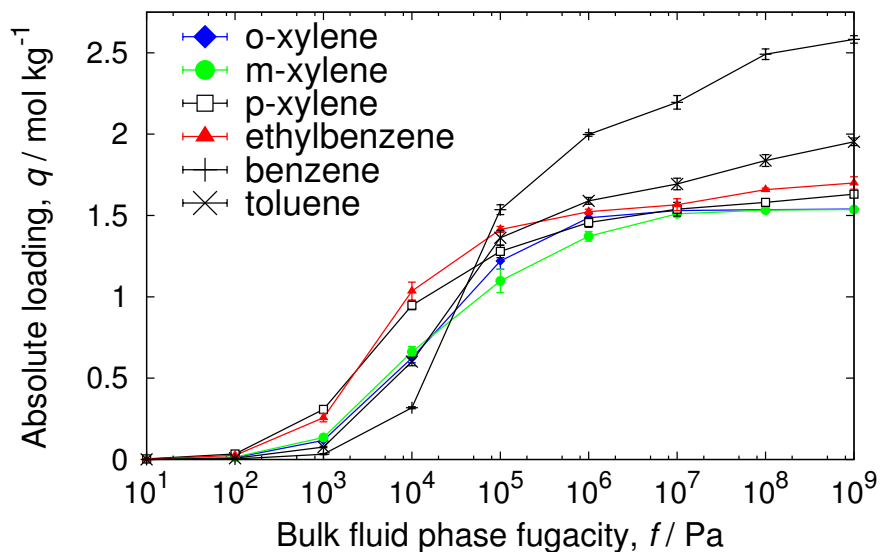
7.1 BEA

unit cell size	$a = b = 12.632[\text{\AA}], c = 26.186[\text{\AA}]$
unit cell angles	$\alpha = \beta = \gamma = 90[^\circ]$
unit cells	$2 \times 2 \times 1$
framework density	$1528.19 [\text{kg}/\text{m}^3]$
description	BEA zeolite
crystallographic data	ref. [39]
void fraction	0.4213 [-]
accessible pore volume	$0.2757 [\text{cm}^3/\text{g}]$
nitrogen surface area	$994 [\text{m}^2/\text{g}], 1519 [\text{m}^2/\text{cm}^3]$
optimization	-
charges	REPEAT with PES from VASP

Pure component isotherms; CBMC; BEA ; 433K



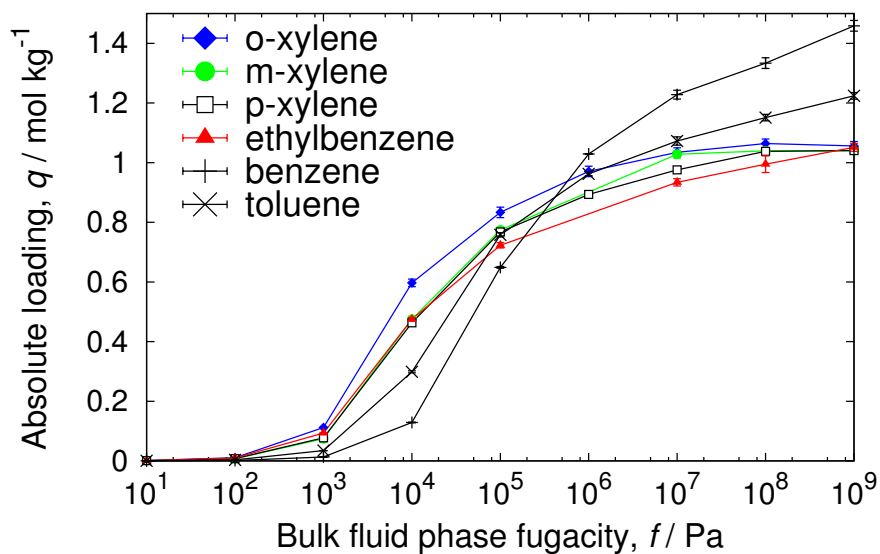
Pure component isotherms; CB/CFCMC; BEA ; 433K



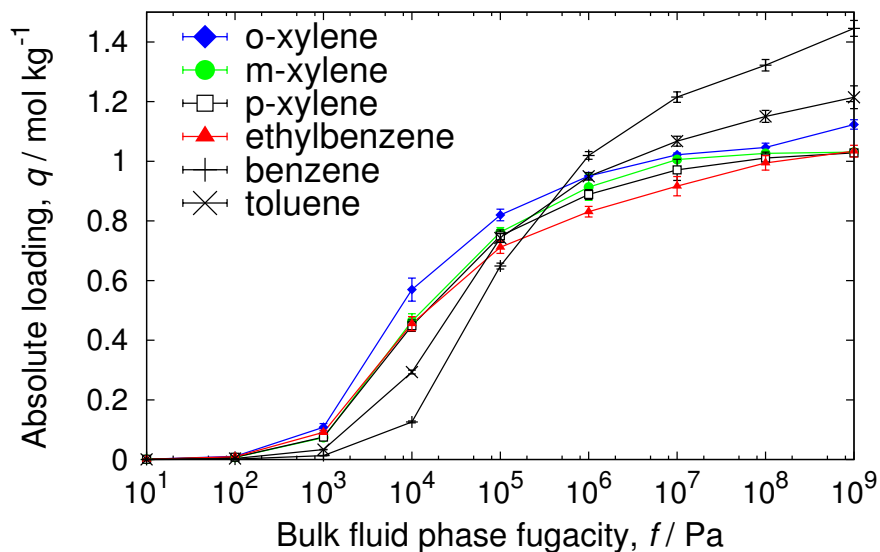
7.2 DON

unit cell size	$a = 18.89[\text{\AA}], b = 23.365[\text{\AA}], c = 8.469[\text{\AA}]$
unit cell angles	$\alpha = \beta = \gamma = 90[^\circ]$
unit cells	$2 \times 2 \times 4$
framework density	$1708.28 [\text{kg}/\text{m}^3]$
description	DON zeolite
crystallographic data	ref. [40]
void fraction	$0.2879 [-]$
accessible pore volume	$0.1685 [\text{cm}^3/\text{g}]$
nitrogen surface area	$525 [\text{m}^2/\text{g}], 897 [\text{m}^2/\text{cm}^3]$
optimization	-
charges	REPEAT with PES from VASP

Pure component isotherms; CBMC; DON ; 433K

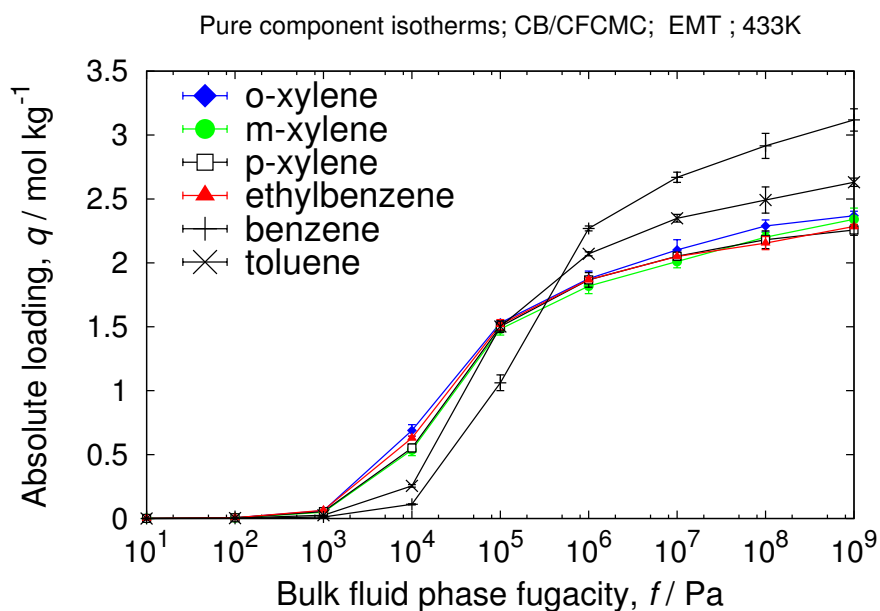
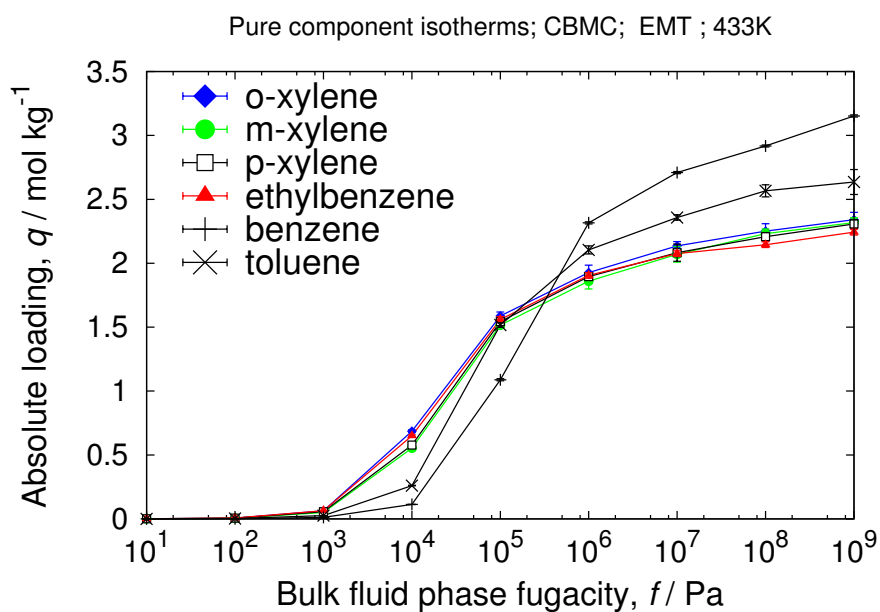


Pure component isotherms; CB/CFCMC; DON ; 433K



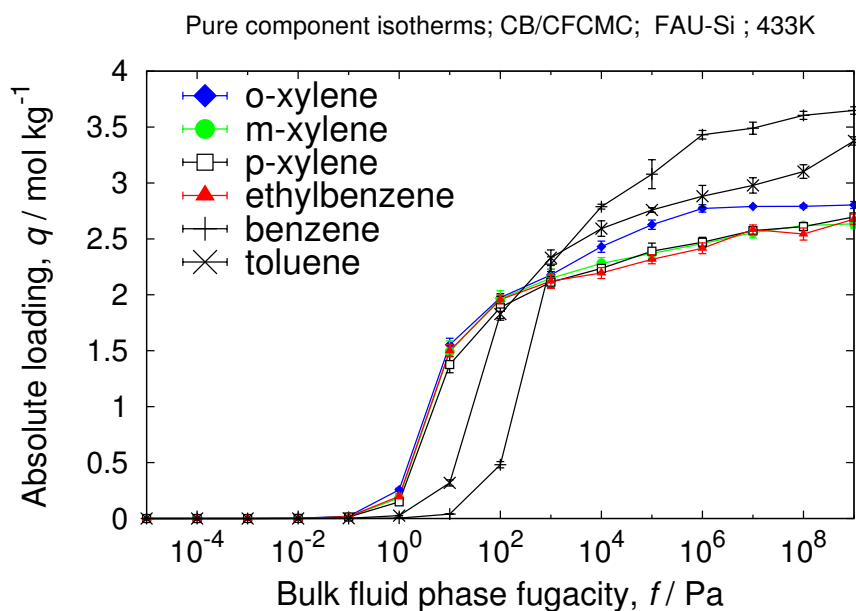
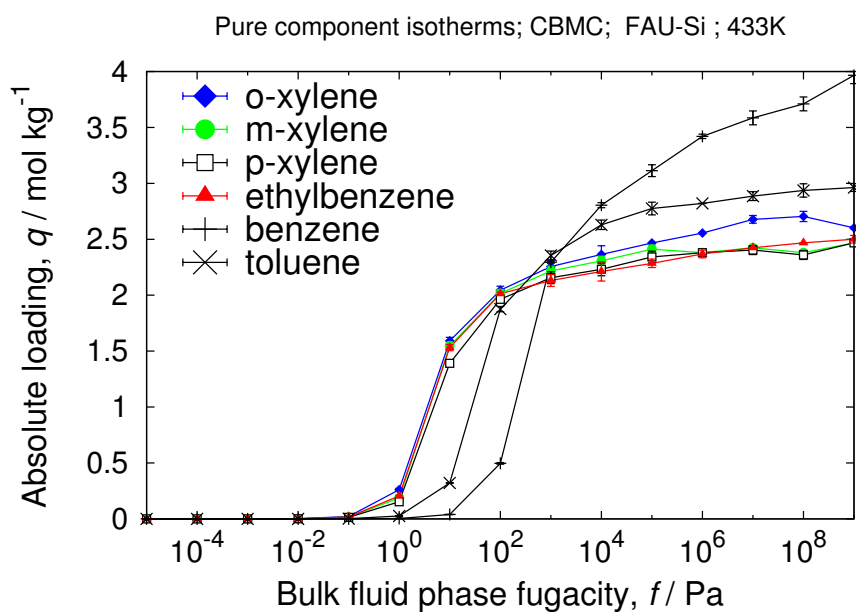
7.3 EMT

unit cell size	$a = b = 17.215[\text{\AA}], c = 28.082[\text{\AA}]$
unit cell angles	$\alpha = \beta = 90[^\circ], \gamma = 120[^\circ]$
unit cells	$2 \times 2 \times 1$
framework density	$1328.95 [\text{kg}/\text{m}^3]$
description	EMT zeolite
crystallographic data	ref. [41]
void fraction	0.4920 [-]
accessible pore volume	$0.3702 [\text{cm}^3/\text{g}]$
nitrogen surface area	$1136 [\text{m}^2/\text{g}], 1510 [\text{m}^2/\text{cm}^3]$
optimization	-
charges	REPEAT with PES from VASP



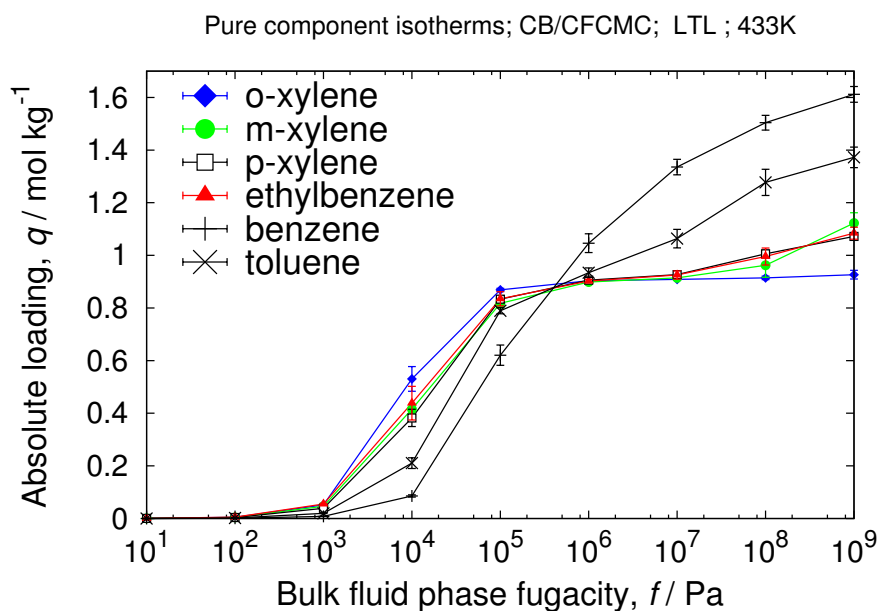
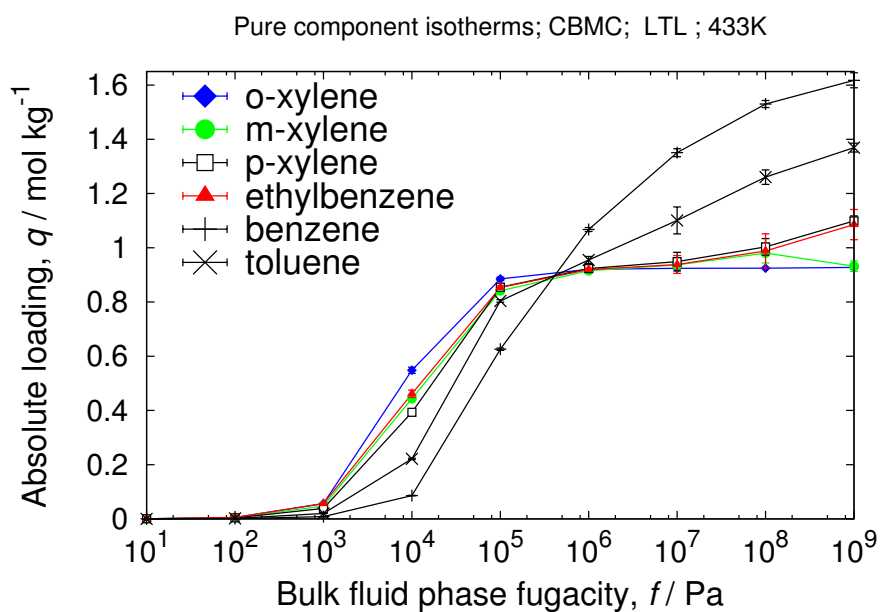
7.4 FAU-Si

unit cell size	$a = b = c = 24.2576[\text{\AA}]$
unit cell angles	$\alpha = \beta = \gamma = 90[^\circ]$
unit cells	$2 \times 2 \times 2$ (primitive cells)
framework density	1319.71 [kg/m ³]
description	FAU-Si zeolite
crystallographic data	ref. [42]
void fraction	0.4838 [-]
accessible pore volume	0.3666 [cm ³ /g]
nitrogen surface area	1156 [m ² /g], 1526 [m ² /cm ³]
optimization	-
charges	REPEAT with PES from VASP



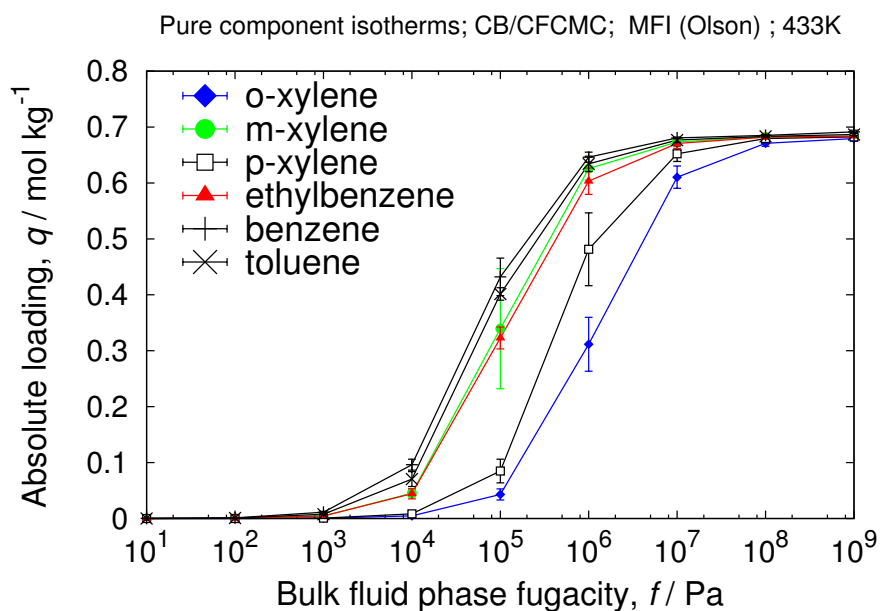
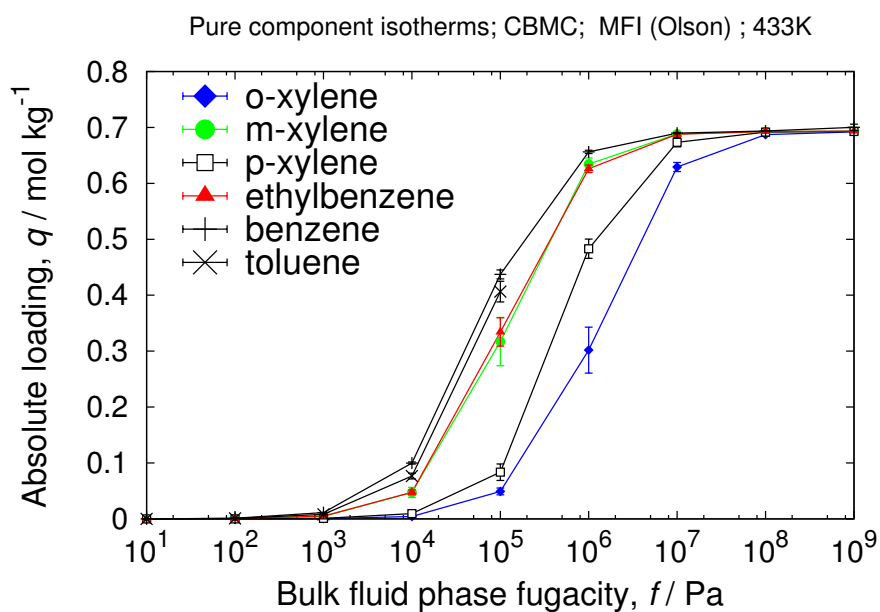
7.5 LTL

unit cell size	$a = b = 18.126[\text{\AA}], c = 7.567[\text{\AA}]$
unit cell angles	$\alpha = \beta = 90[^\circ], \gamma = 120[^\circ]$
unit cells	$2 \times 4 \times 4$
framework density	$1668.22 [\text{kg}/\text{m}^3]$
description	LTL zeolite
crystallographic data	ref. [43]
void fraction	0.5198 [-]
accessible pore volume	$0.3116 [\text{cm}^3/\text{g}]$
nitrogen surface area	$550 [\text{m}^2/\text{g}], 918 [\text{m}^2/\text{cm}^3]$
optimization	-
charges	REPEAT with PES from VASP



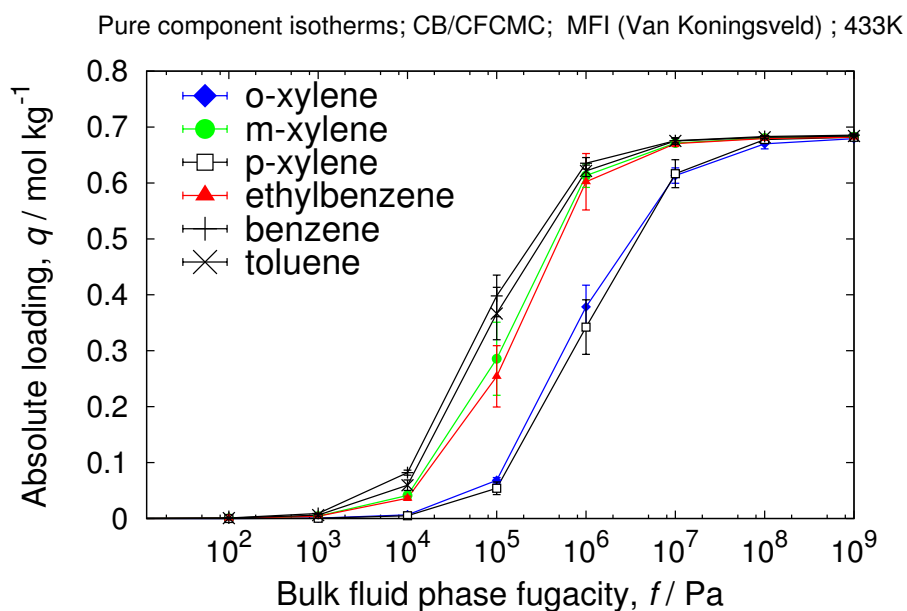
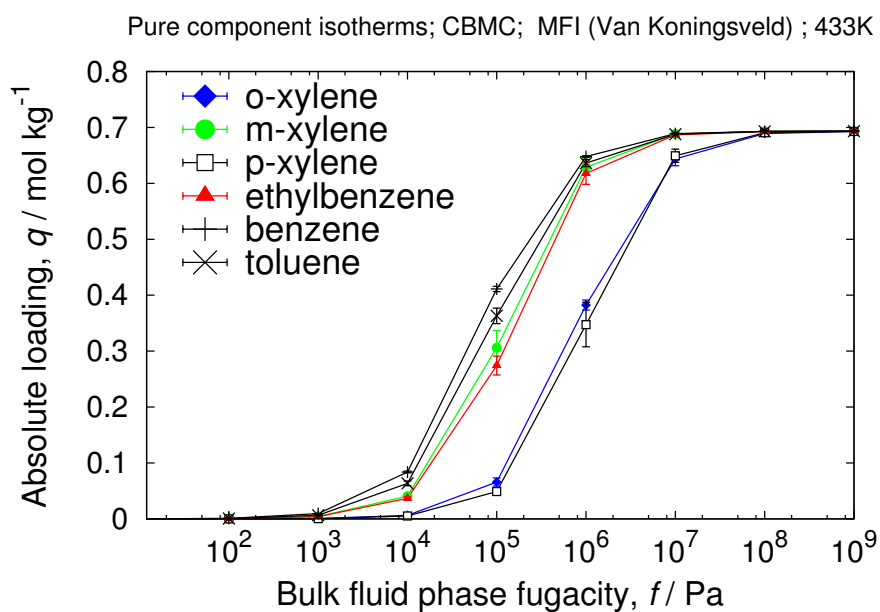
7.6 MFI-ortho (Olson)

unit cell size	$a = 20.07[\text{\AA}], b = 19.92[\text{\AA}], c = 13.42[\text{\AA}]$
unit cell angles	$\alpha = \beta = \gamma = 90[^\circ]$
unit cells	$2 \times 2 \times 2$
framework density	1785.22 [kg/m ³]
description	MFI-Olson zeolite
crystallographic data	ref. [44]
void fraction	0.2988 [-]
accessible pore volume	0.1674 [cm ³ /g]
nitrogen surface area	599 [m ² /g], 1069 [m ² /cm ³]
optimization	-
charges	REPEAT with PES from VASP



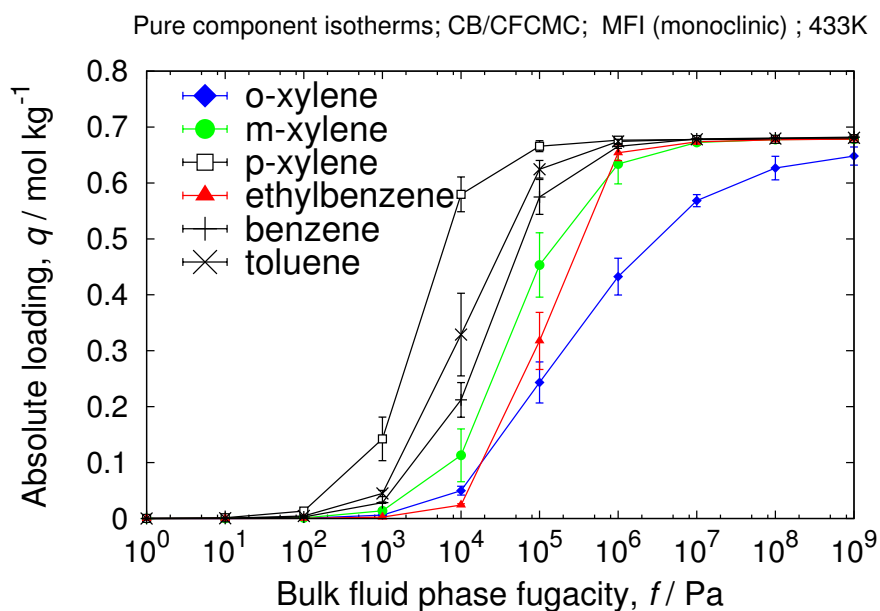
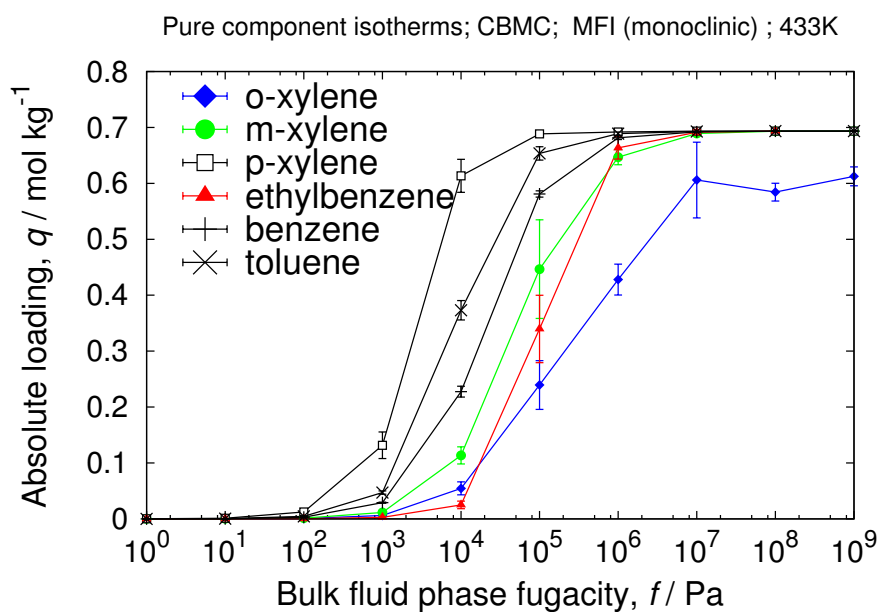
7.7 MFI-ortho (Van Koningsveld)

unit cell size	$a = 20.022, b = 19.899, c = 13.383 [\text{\AA}]$
unit cell angles	$\alpha = \beta = \gamma = 90[^\circ]$
unit cells	$2 \times 2 \times 2$
framework density	$1796.34 [\text{kg}/\text{m}^3]$
description	MFI zeolite
crystallographic data	ref. [45]
void fraction	0.2941 [-]
accessible pore volume	$0.1637 [\text{cm}^3/\text{g}]$
nitrogen surface area	$584 [\text{m}^2/\text{g}], 1050 [\text{m}^2/\text{cm}^3]$
optimization	-
charges	REPEAT with PES from VASP



7.8 MFI-mono

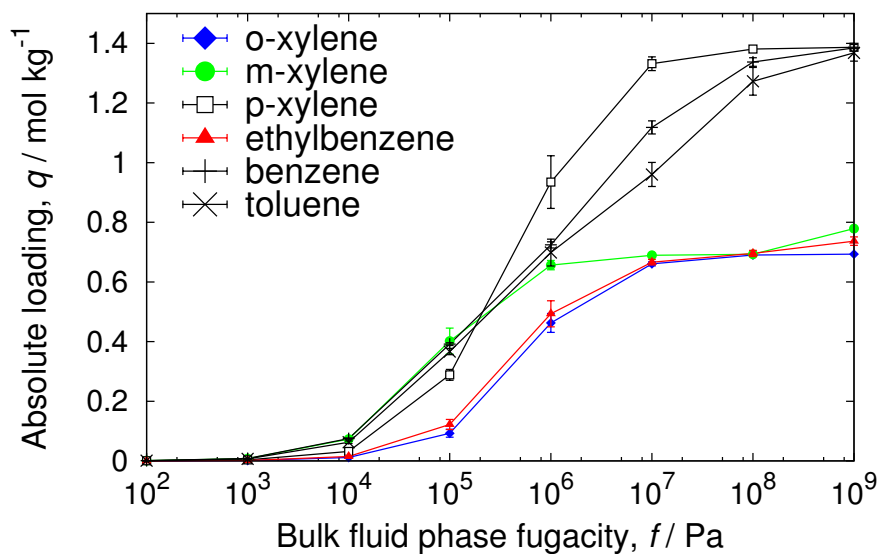
unit cell size	$a = 20.1087[\text{\AA}], b = 19.879[\text{\AA}], c = 13.369[\text{\AA}]$
unit cell angles	$\alpha = 90.67[^\circ], \beta = \gamma = 90[^\circ]$
unit cells	$2 \times 2 \times 2$
framework density	1792.54[kg/m ³]
description	MFI-mono zeolite
crystallographic data	ref. [46]
void fraction	0.2860
accessible pore volume	0.1595
nitrogen surface area	663 [m ² /g], 1188 [m ² /cm ³]
optimization	-
charges	REPEAT with PES from VASP



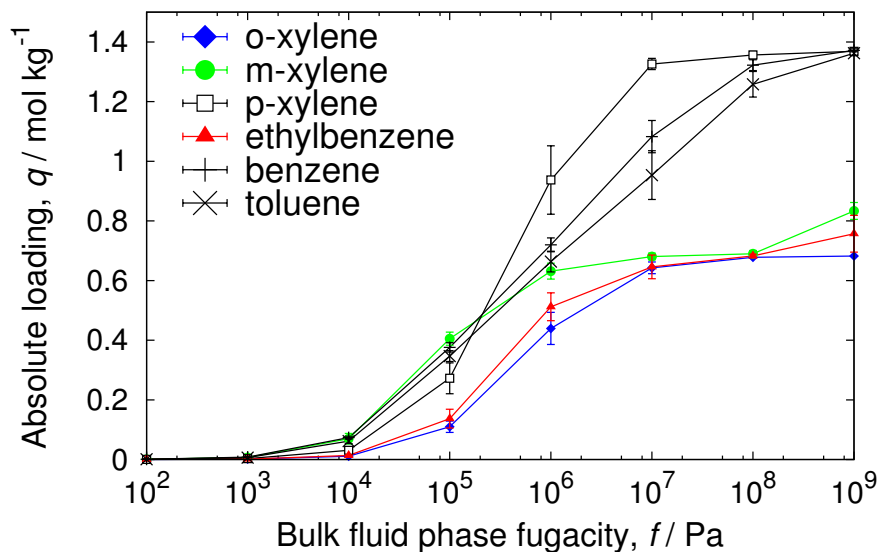
7.9 MFI-para

unit cell size	$a = 20.121[\text{\AA}], b = 19.82[\text{\AA}], c = 13.438[\text{\AA}]$
unit cell angles	$\alpha = \beta = \gamma = 90[^\circ]$
unit cells	$2 \times 2 \times 2$
framework density	$1787.28 [\text{kg}/\text{m}^3]$
description	MFI-para zeolite
crystallographic data	ref. [47]
void fraction	0.2782 [-]
accessible pore volume	$0.1559 [\text{cm}^3/\text{g}]$
nitrogen surface area	$602 [\text{m}^2/\text{g}], 1076 [\text{m}^2/\text{cm}^3]$
optimization	-
charges	REPEAT with PES from VASP

Pure component isotherms; CBMC; MFI (para) ; 433K

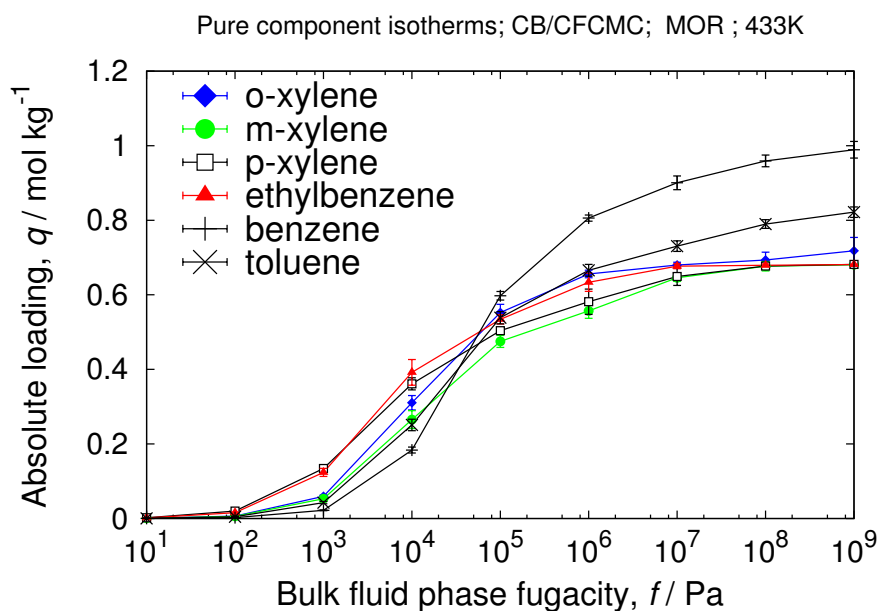
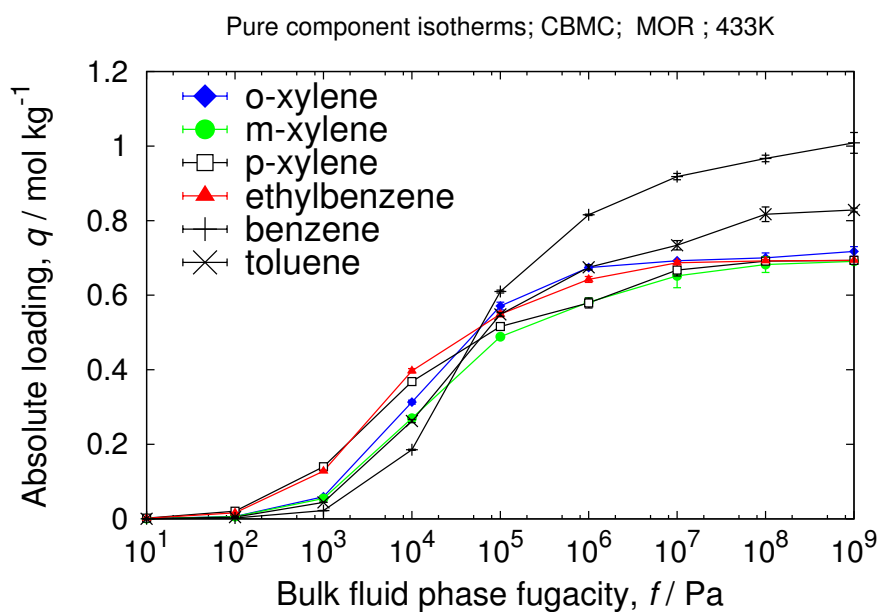


Pure component isotherms; CB/CFCMC; MFI (para) ; 433K



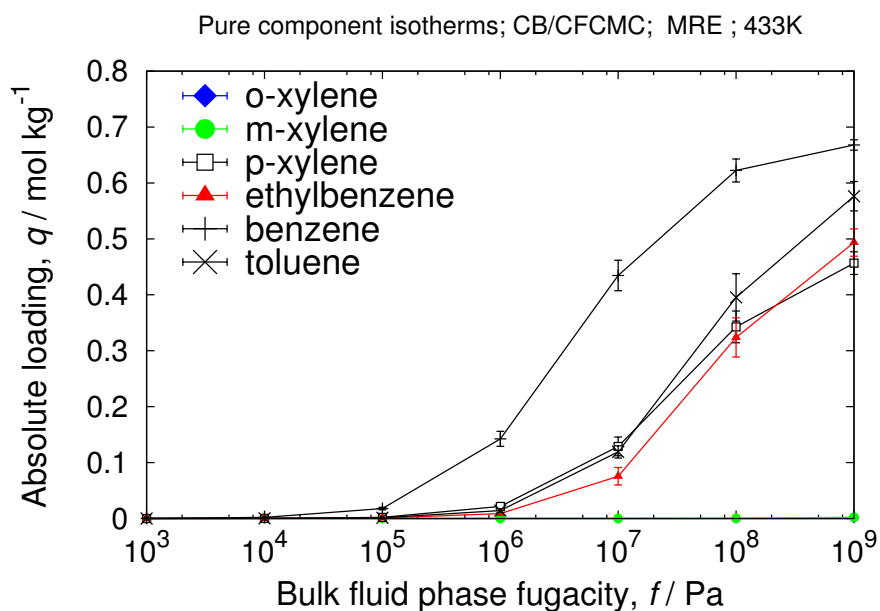
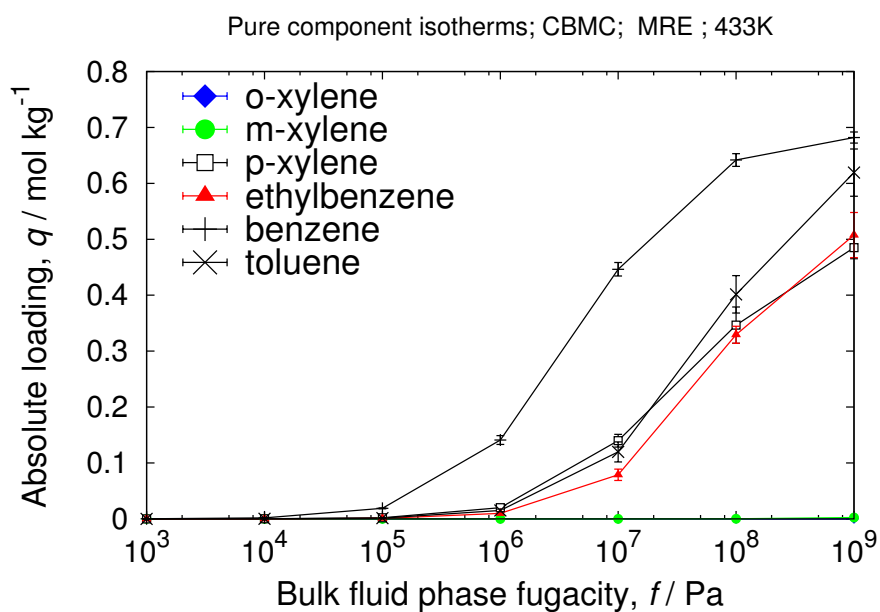
7.10 MOR

unit cell size	$a = 18.256, b = 20.534, c = 7.542 [\text{\AA}]$
unit cell angles	$\alpha = \beta = \gamma = 90 [^\circ]$
unit cells	$2 \times 2 \times 4$
framework density	$1693.89 [\text{kg}/\text{m}^3]$
description	MOR zeolite
crystallographic data	ref. [48]
void fraction	$0.2677 [-]$
accessible pore volume	$0.1580 [\text{cm}^3/\text{g}]$
nitrogen surface area	$994 [\text{m}^2/\text{g}], 1519 [\text{m}^2/\text{cm}^3]$
optimization	-
charges	REPEAT with PES from VASP



7.11 MRE

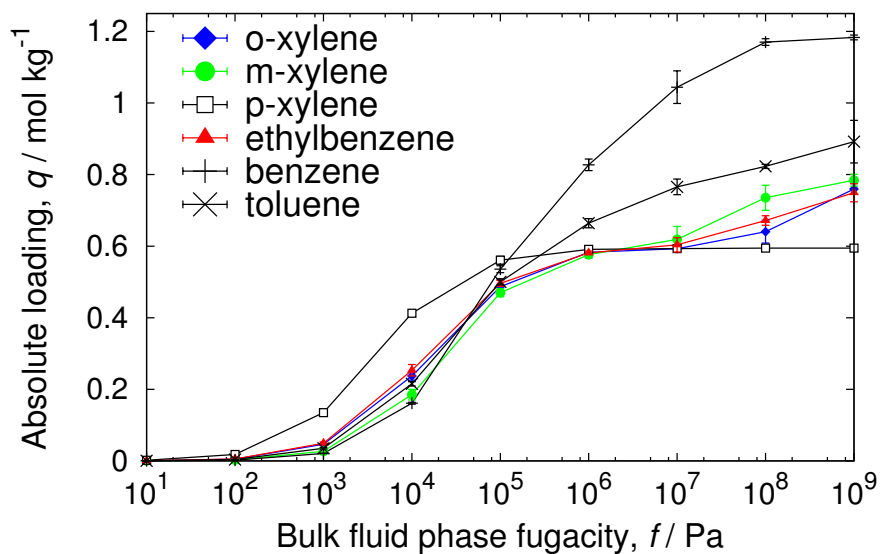
unit cell size	$a = 8.257[\text{\AA}], b = 14.562[\text{\AA}], c = 20.314[\text{\AA}]$
unit cell angles	$\alpha = \beta = \gamma = 90[^\circ]$
unit cells	$4 \times 2 \times 2$
framework density	1960.706 [kg/m ³]
description	MRE-type, ZSM-48
crystallographic data	ref. [49]
void fraction	0.1753 [-]
accessible pore volume	0.0894 [cm ³ /g]
nitrogen surface area	573 [m ² /g], 292 [m ² /cm ³]
optimization	-
charges	REPEAT with PES from VASP



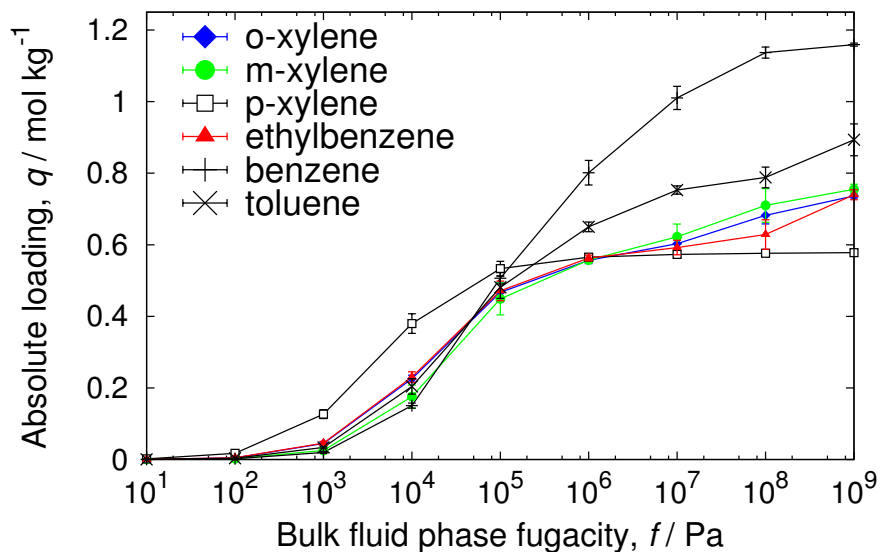
7.12 MTW

unit cell size	$a = 25.552[\text{\AA}], b = 5.256[\text{\AA}], c = 12.117[\text{\AA}]$
unit cell angles	$\alpha = 90[^\circ], \beta = 109.312[^\circ], \gamma = 90[^\circ]$
unit cells	$1 \times 6 \times 3$
framework density	$1819.05 [\text{kg}/\text{m}^3]$
description	MTW-type zeolite
crystallographic data	ref. [50]
void fraction	$0.2116 [-]$
accessible pore volume	$0.1163 [\text{cm}^3/\text{g}]$
nitrogen surface area	$818 [\text{m}^2/\text{g}], 450 [\text{m}^2/\text{cm}^3]$
optimization	-
charges	REPEAT with PES from VASP

Pure component isotherms; CBMC; MTW ; 433K



Pure component isotherms; CB/GFCMC; MTW ; 433K

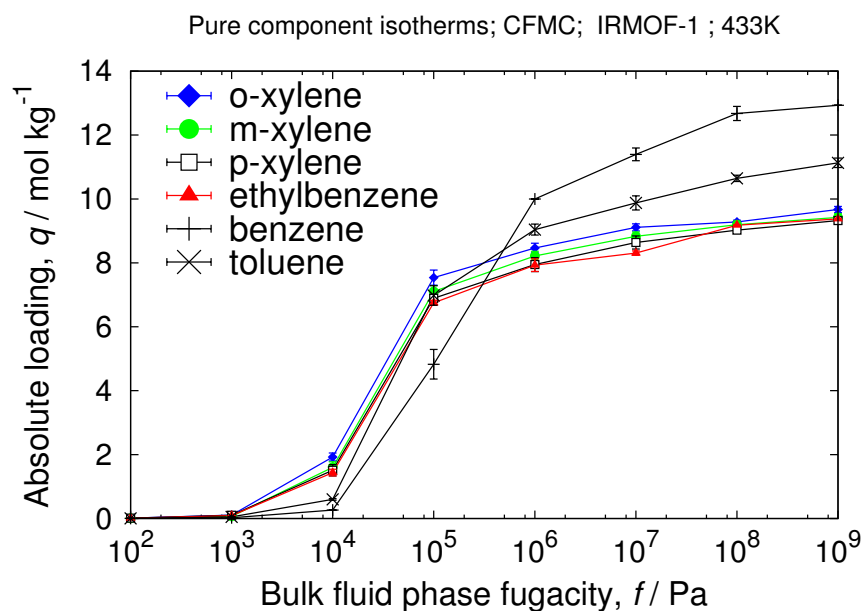
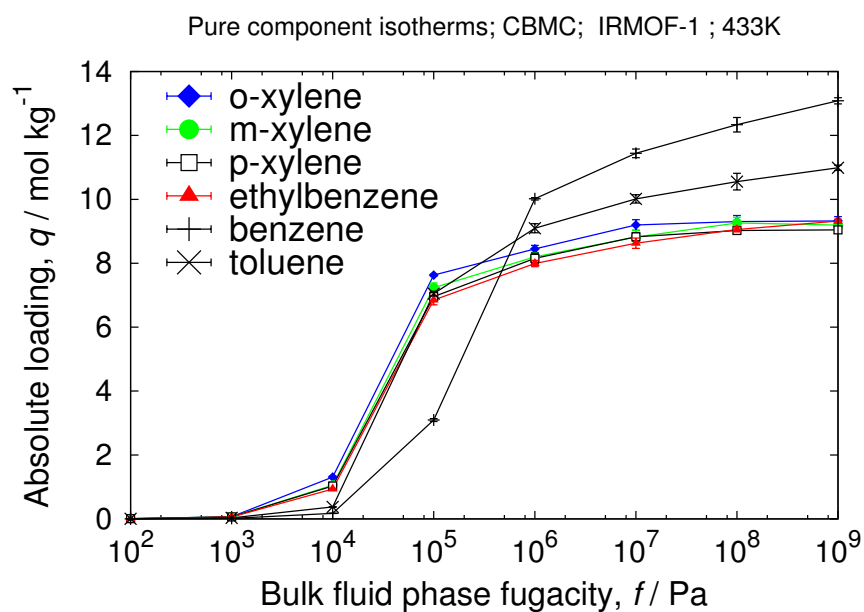


8

Screening of Potential MOF Adsorbents

8.1 IRMOF-1

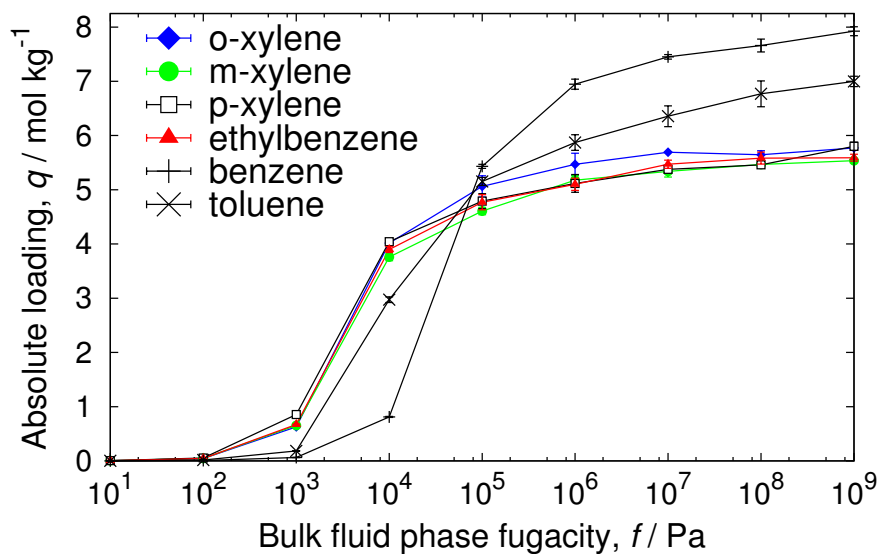
unit cell size	$a = b = c = 25.832[\text{\AA}]$
unit cell angles	$\alpha = \beta = \gamma = 90[^\circ]$
unit cells	$2 \times 2 \times 2$ (primitive cells)
framework density	593.39 [kg/m ³]
description	IRMOF-1
crystallographic data	ref. [51]
void fraction	0.8039[-]
accessible pore volume	0.9271[cm ³ /g]
nitrogen surface area	3592 [m ² /g], 2131 [m ² /cm ³]
optimization	-
charges	REPEAT with PES from VASP



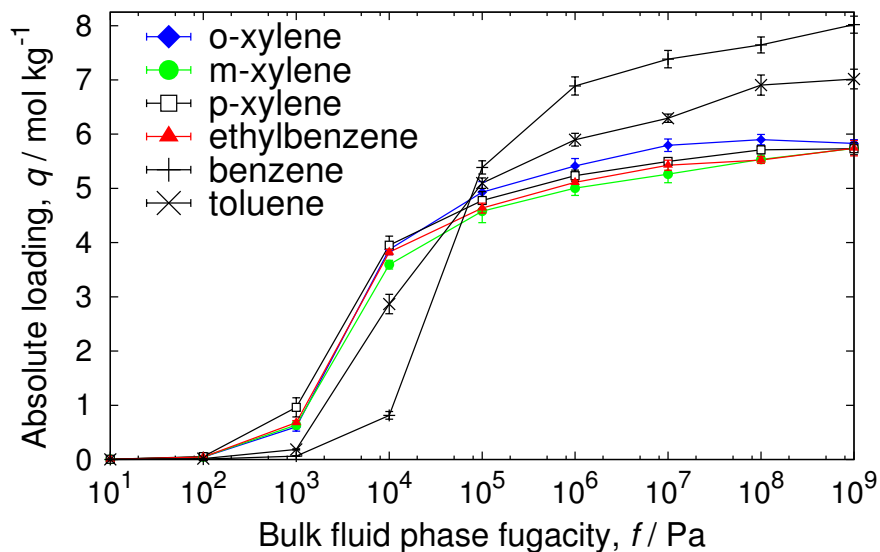
8.2 CoBDP

unit cell size	$a = 13.253[\text{\AA}], b = 13.253[\text{\AA}], c = 13.995[\text{\AA}]$
unit cell angles	$\alpha = \beta = \gamma = 90[^\circ]$
unit cells	$2 \times 2 \times 3$
framework density	721.88 [kg/m ³]
description	Co(BDP)
crystallographic data	ref. [52]
void fraction	0.6535 [-]
accessible pore volume	0.9053 [cm ³ /g]
nitrogen surface area	2244 [m ² /g], 1620 [m ² /cm ³]
optimization	VASP fixed cell, PBE, precision=high
charges	REPEAT with PES from VASP

Pure component isotherms; CBMC; CoBDP ; 433K

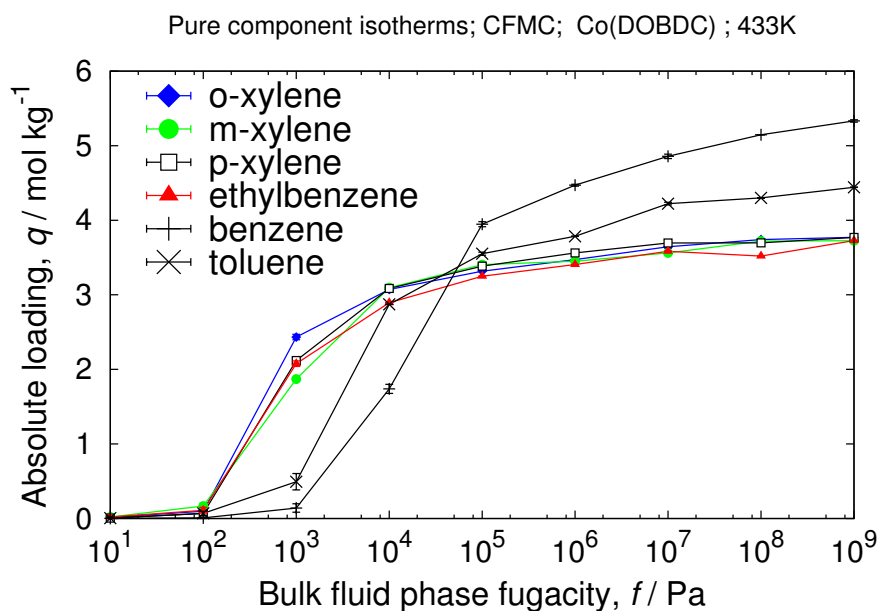
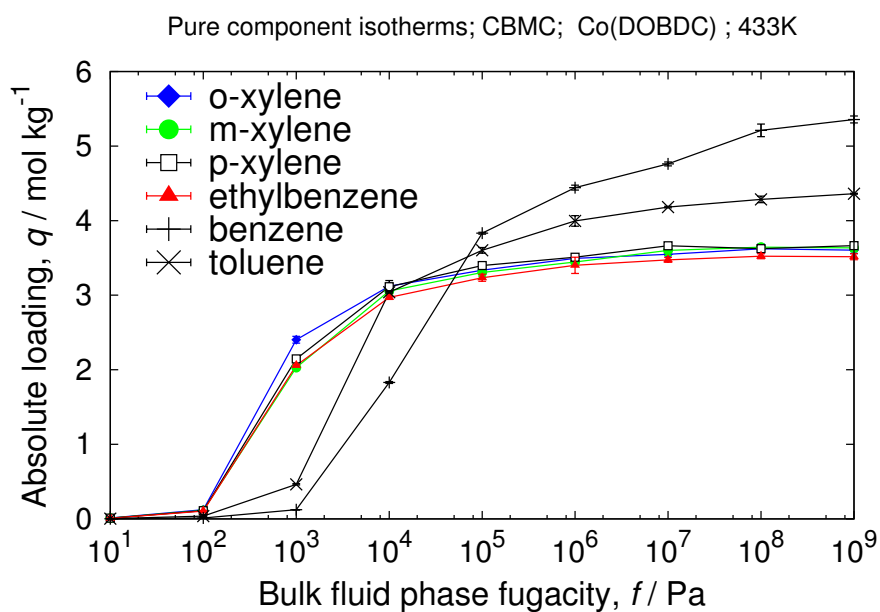


Pure component isotherms; CFMC; CoBDP ; 433K



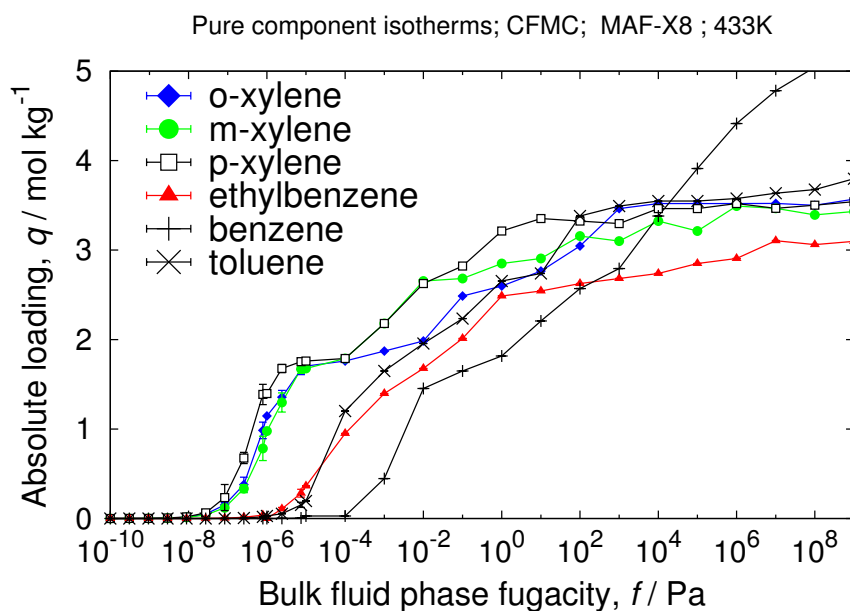
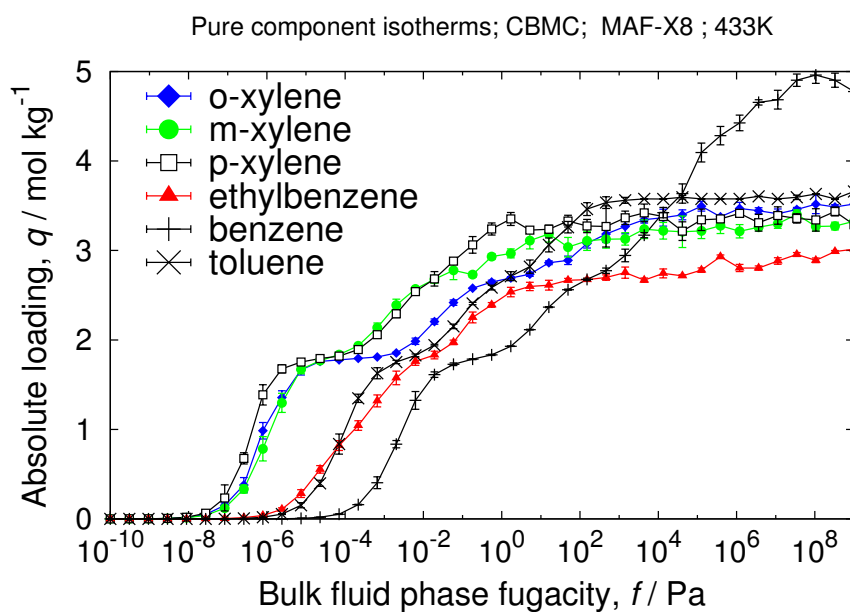
8.3 CoDOBDC

unit cell size	$a = 25.885[\text{\AA}], b = 25.885[\text{\AA}], c = 6.8058[\text{\AA}]$
unit cell angles	$\alpha = \beta = 90, \gamma = 120[^\circ]$
unit cells	$2 \times 2 \times 4$
framework density	1180.56 [kg/m ³]
description	Co(DOBDC)
crystallographic data	ref. [53]
void fraction	0.7061 [-]
accessible pore volume	0.5981 [cm ³ /g]
nitrogen surface area	1338[m ² /g], 1580[m ² /cm ³]
optimization	-
charges	REPEAT with PES from VASP



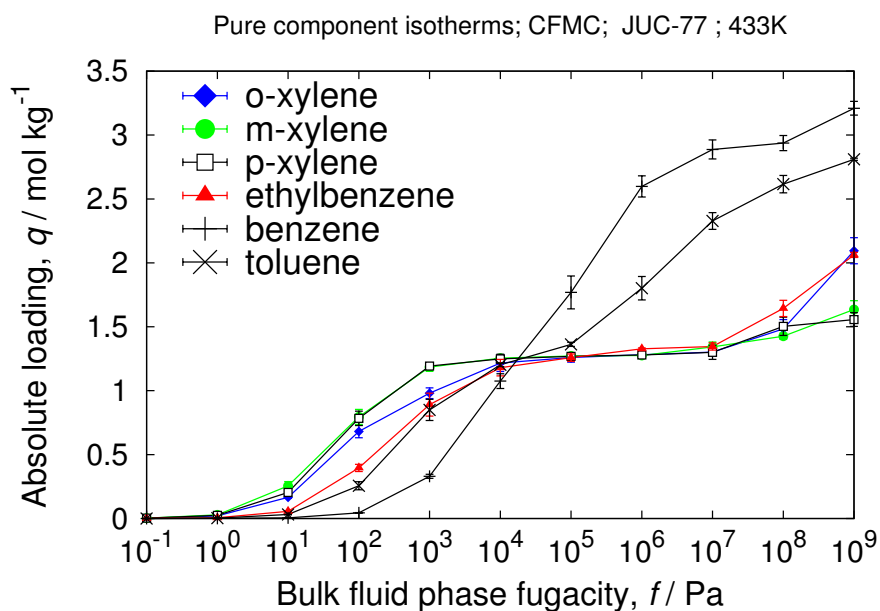
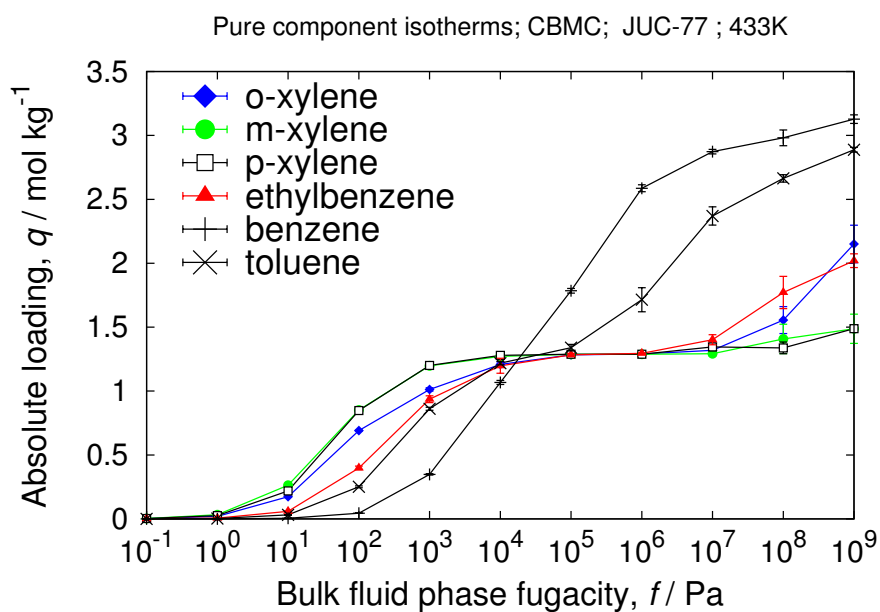
8.4 MAF-X8

unit cell size	$a = 13.9249[\text{\AA}], b = 23.653[\text{\AA}], c = 23.637[\text{\AA}]$
unit cell angles	$\alpha = \beta = \gamma = 90[^\circ]$
unit cells	$2 \times 2 \times 2$
framework density	954.29 [kg/m ³]
description	MAF-X8
crystallographic data	ref. [54]
void fraction	0.4947[-]
accessible pore volume	0.5184 [cm ³ /g]
nitrogen surface area	1465 [m ² /g], 1397 [m ² /cm ³]
optimization	-
charges	REPEAT with PES from VASP



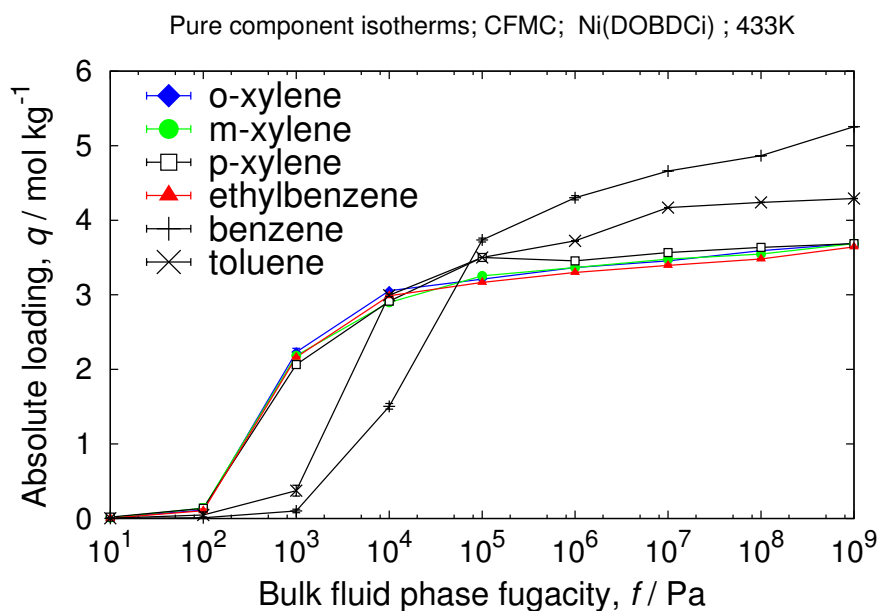
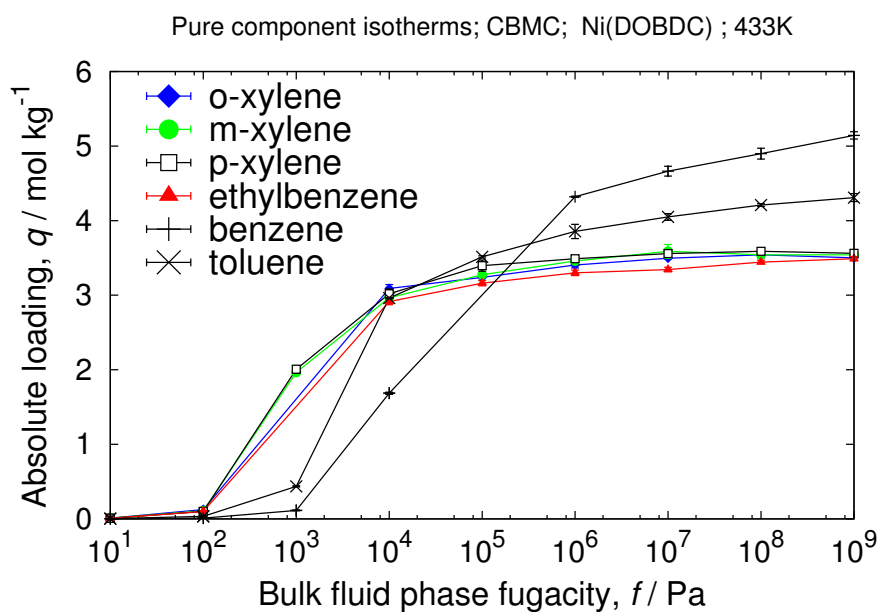
8.5 JUC-77

unit cell size	$a = 19.2396[\text{\AA}], b = 20.3017[\text{\AA}], c = 46.143[\text{\AA}]$
unit cell angles	$\alpha = \beta = \gamma = 90[^\circ]$
unit cells	$2 \times 2 \times 2$ (primitive cells)
framework density	1144.03 [kg/m ³]
description	JUC-77
crystallographic data	ref. [55]
void fraction	0.4783 [-]
accessible pore volume	0.4181 [cm ³ /g]
nitrogen surface area	1098 [m ² /g], 1256 [m ² /cm ³]
optimization	VASP fixed cell, PBE, precision=high
charges	REPEAT with PES from VASP



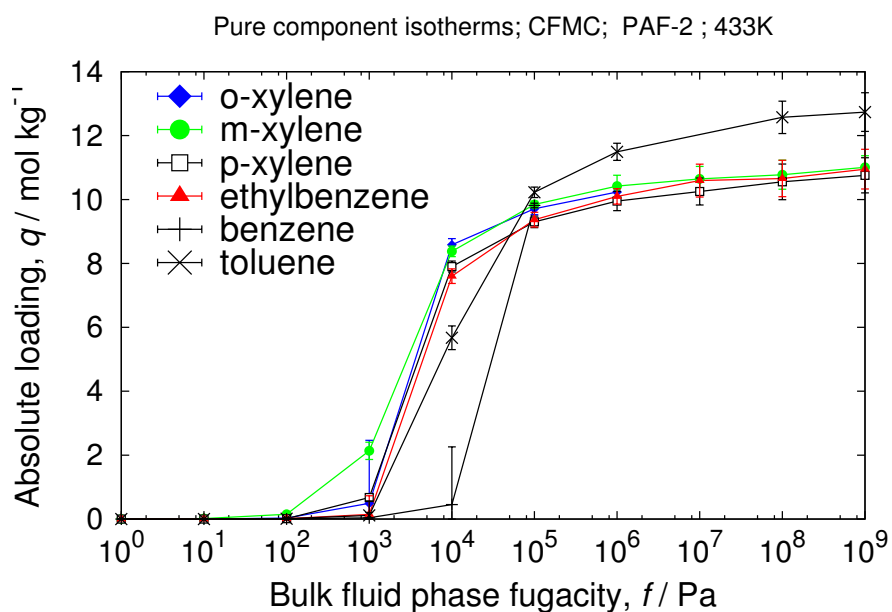
8.6 NiDOBDC

unit cell size	$a = 25.7856[\text{\AA}], b = 25.7856[\text{\AA}], c = 6.7701[\text{\AA}]$
unit cell angles	$\alpha = \beta = 90, \gamma = 120[^\circ]$
unit cells	$2 \times 2 \times 4$
framework density	1194.12 [kg/m ³]
description	Ni(DOBDC)
crystallographic data	ref. [56]
void fraction	0.6943[-]
accessible pore volume	0.5804 [cm ³ /g]
nitrogen surface area	1312 [m ² /g], 1566 [m ² /cm ³]
optimization	-
charges	REPEAT with PES from VASP



8.7 PAF-2

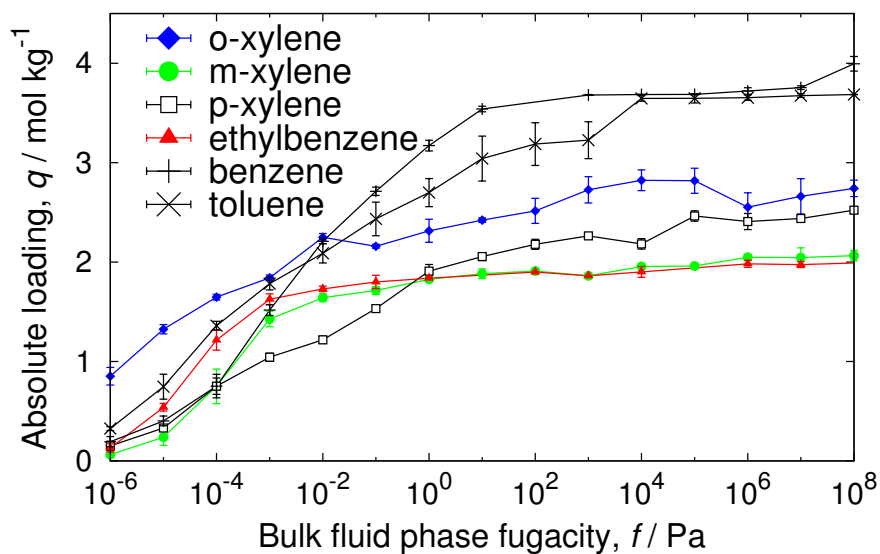
unit cell size	$a = 26.2266[\text{\AA}], b = 26.2266[\text{\AA}], c = 26.2266[\text{\AA}]$
unit cell angles	$\alpha = \beta = \gamma = 90[^\circ]$
unit cells	$2 \times 2 \times 2$ (primitive cells)
framework density	464.44 [kg/m ³]
description	PAF-2
crystallographic data	ref. [57]
void fraction	0.7996 [-]
accessible pore volume	1.7215[cm ³ /g]
nitrogen surface area	4623 [m ² /g], 2150 [m ² /cm ³]
optimization	VASP fixed cell, PBE, precision=high
charges	REPEAT with PES from VASP



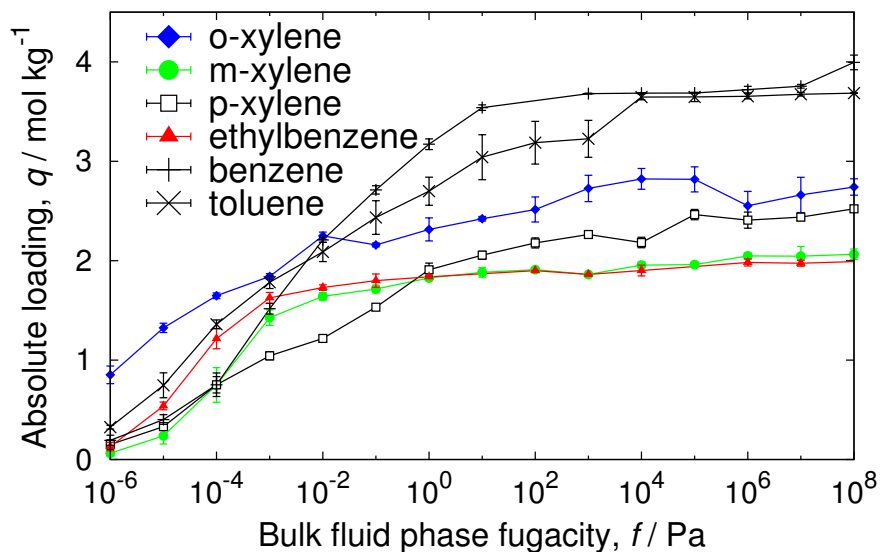
8.8 UiO-66

unit cell size	$a = b = c = 20.7004[\text{\AA}]$
unit cell angles	$\alpha = \beta = \gamma = 90[^\circ]$
unit cells	$2 \times 2 \times 2$
framework density	1219.0883[kg/m ³]
description	UiO-66
crystallographic data	ref. [58]
void fraction	0.4965 [-]
accessible pore volume	0.4072 [cm ³ /g]
nitrogen surface area	1116 [m ² /g], 1360 [m ² /cm ³]
optimization	-
charges	REPEAT with PES from VASP

Pure component isotherms; CBMC; UiO-66 ; 433K

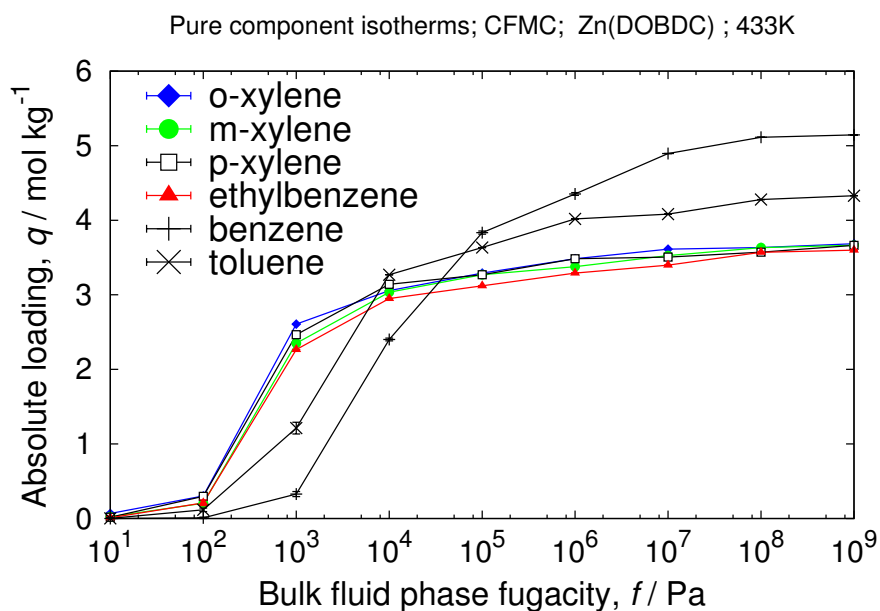
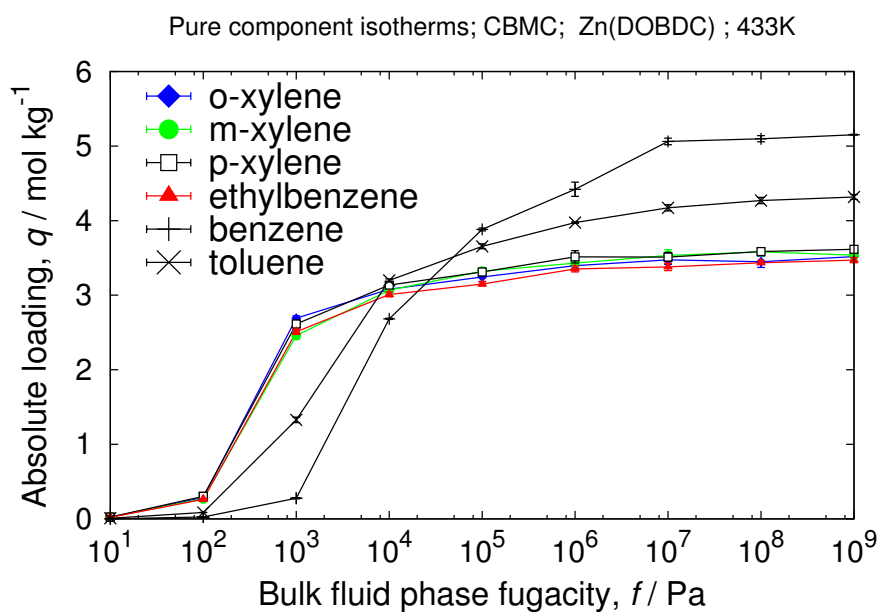


Pure component isotherms; CFMC; UiO-66 ; 433K



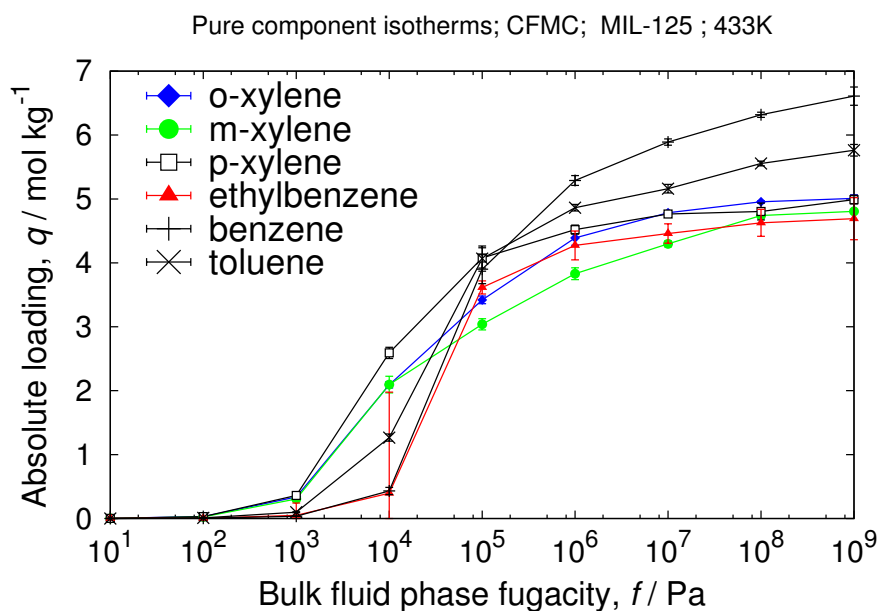
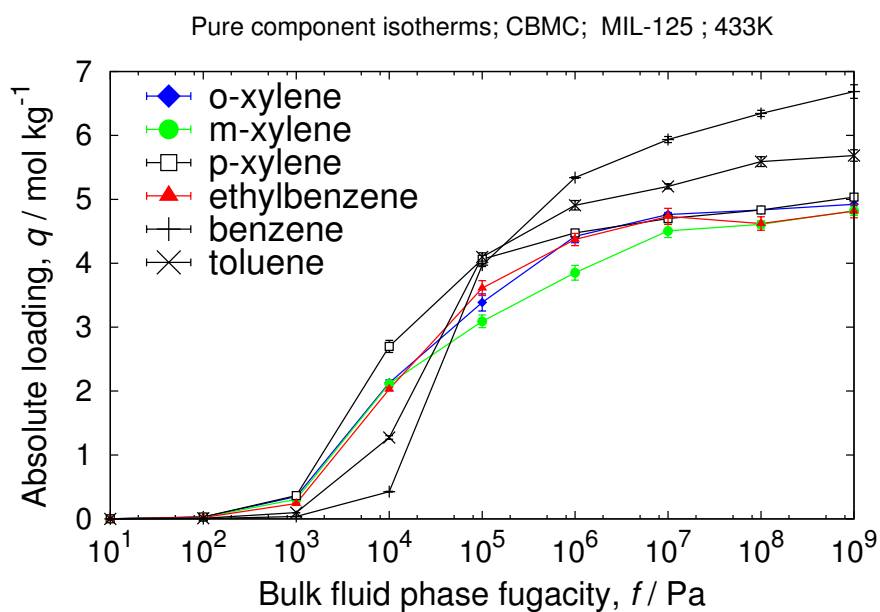
8.9 ZnDOBDC

unit cell size	$a = b = 25.9320[\text{\AA}], c = 6.8365[\text{\AA}]$
unit cell angles	$\alpha = \beta = 90, \gamma = 120[^\circ]$
unit cells	$2 \times 2 \times 4$
framework density	1219.61 [kg/m ³]
description	Zn(DOBDC)
crystallographic data	ref. [59]
void fraction	0.7193[-]
accessible pore volume	0.5898 [cm ³ /g]
nitrogen surface area	1289 [m ² /g], 1572 [m ² /cm ³]
optimization	-
charges	REPEAT with PES from VASP



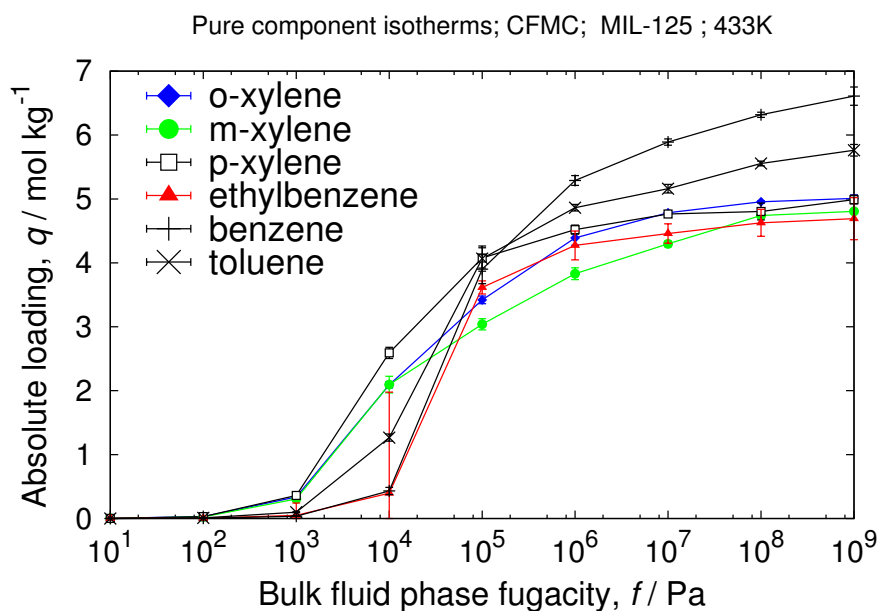
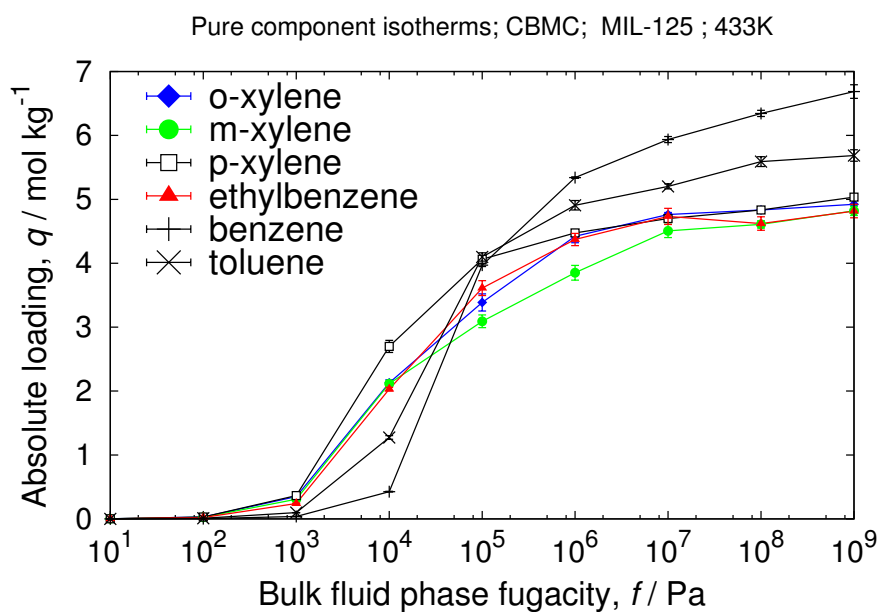
8.10 MIL-125

unit cell size	$a = 18.65430[\text{\AA}], b = 18.65430[\text{\AA}], c = 18.1444[\text{\AA}]$
unit cell angles	$\alpha = \beta = \gamma = 90[^\circ]$
unit cells	$2 \times 2 \times 2$
framework density	822.47 [kg/m ³]
description	MIL-125
crystallographic data	ref. [60]
void fraction	0.6203 [-]
accessible pore volume	0.7542 [cm ³ /g]
nitrogen surface area	2231 [m ² /g], 1835 [m ² /cm ³]
optimization	VASP fixed cell, PBE, precision=high
charges	REPEAT with PES from VASP



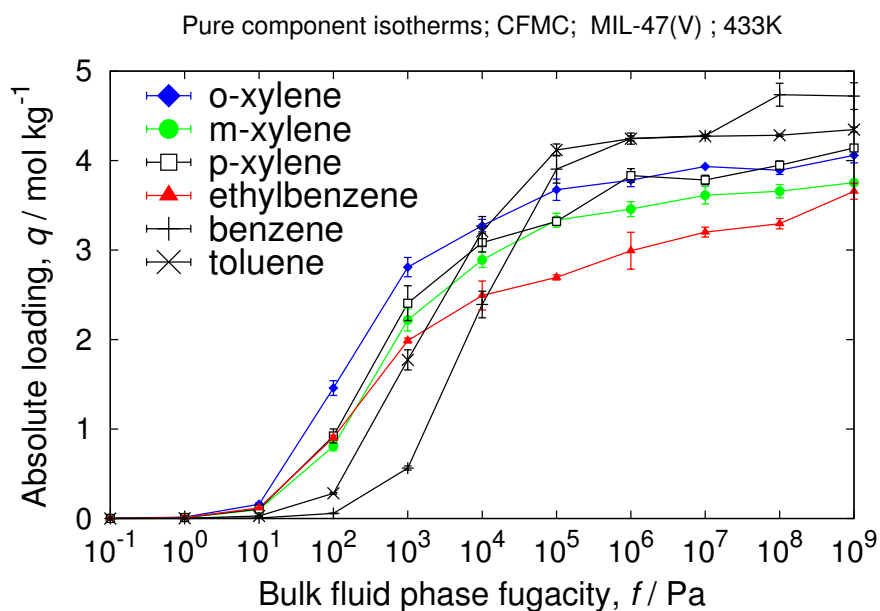
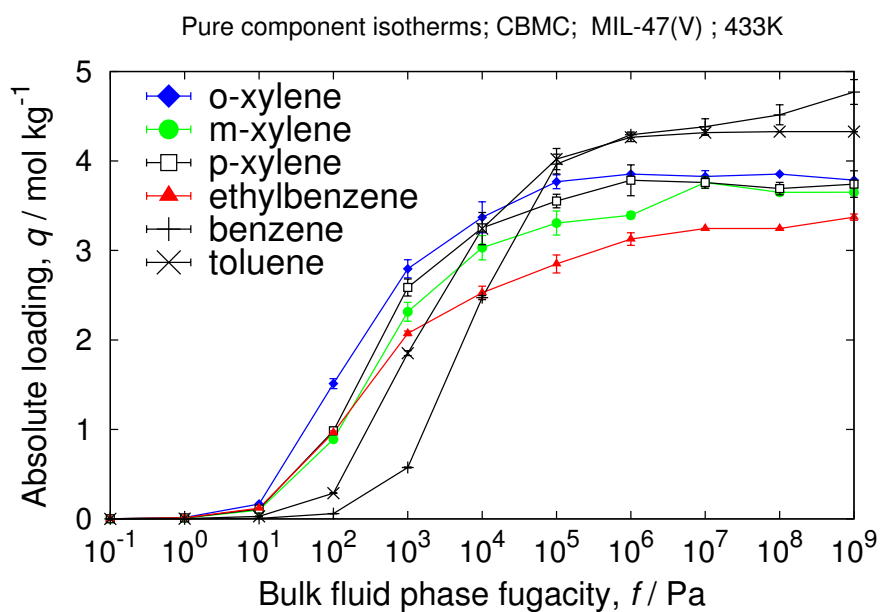
8.11 MIL-125-NH₂

unit cell size	$a = b = 18.729[\text{\AA}], c = 18.172[\text{\AA}]$
unit cell angles	$\alpha = \beta = \gamma = 90[^\circ]$
unit cells	$2 \times 2 \times 2$
framework density	861.6161 [kg/m ³]
description	MIL-125
crystallographic data	ref. [61]
void fraction	0.5921 [-]
accessible pore volume	0.6872 [cm ³ /g]
nitrogen surface area	2231 [m ² /g], 1835 [m ² /cm ³]
optimization	VASP fixed cell, PBE, precision=high
charges	REPEAT with PES from VASP



8.12 MIL-47

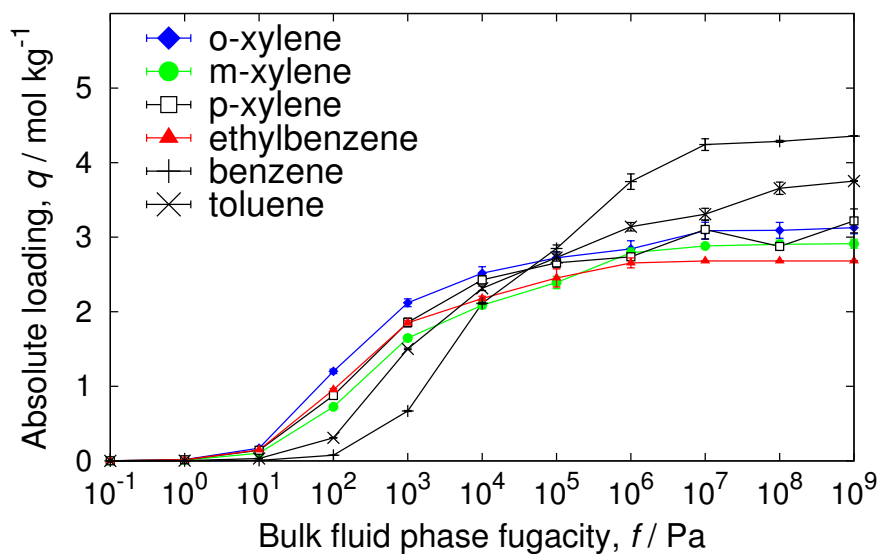
unit cell size	$a = 6.8179[\text{\AA}], b = 16.143[\text{\AA}], c = 13.939[\text{\AA}]$
unit cell angles	$\alpha = \beta = \gamma = 90[^\circ]$
unit cells	$4 \times 2 \times 2$
framework density	1000.36 [kg/m ³]
description	MIL-47
crystallographic data	ref. [62]
void fraction	0.6089 [-]
accessible pore volume	0.6084 [cm ³ /g]
nitrogen surface area	1655 [m ² /g], 1656 [m ² /cm ³]
optimization	-
charges	REPEAT with PES from VASP



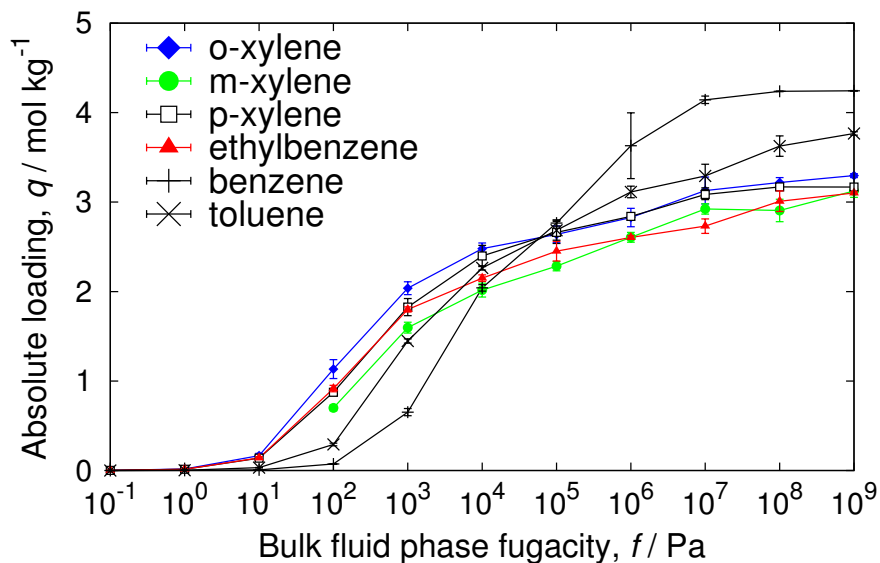
8.13 MIL-53

unit cell size	$a = 16.733[\text{\AA}], b = 13.038[\text{\AA}], c = 6.812[\text{\AA}]$
unit cell angles	$\alpha = \beta = \gamma = 90[^\circ]$
unit cells	$2 \times 2 \times 4$
framework density	$1041.90[\text{kg}/\text{m}^3]$
description	MIL-53
crystallographic data	ref. [63]
void fraction	$0.5501[-]$
accessible pore volume	$0.5279[\text{cm}^3/\text{g}]$
nitrogen surface area	$1435[\text{m}^2/\text{g}], 1495[\text{m}^2/\text{cm}^3]$
optimization	-
charges	REPEAT with PES from VASP

Pure component isotherms; CBMC; MIL-53(Al) ; 433K

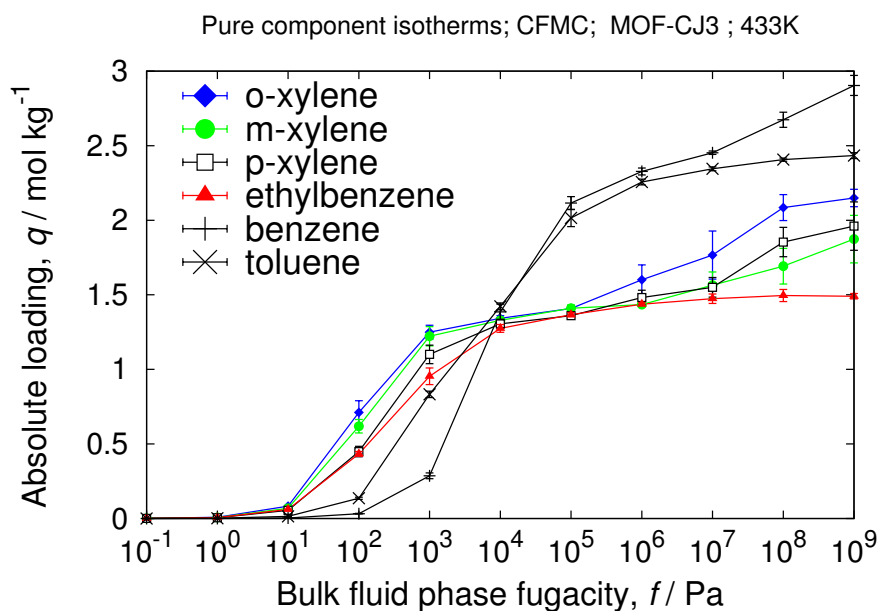
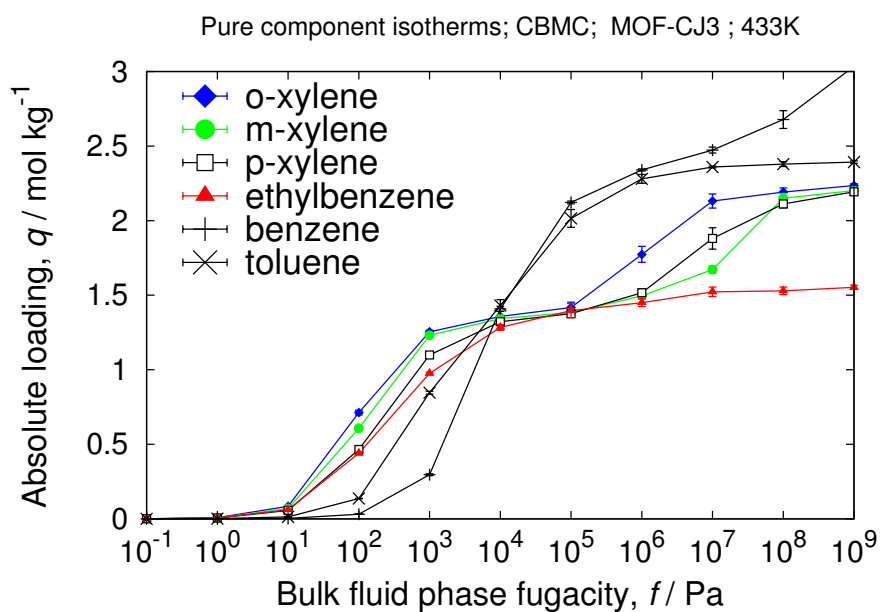


Pure component isotherms; CFMC; MIL-53(Al) ; 433K



8.14 MOF-CJ3

unit cell size	$a = 20.588[\text{\AA}], b = 20.588[\text{\AA}], c = 17.832[\text{\AA}]$
unit cell angles	$\alpha = \beta = \gamma = 90[^\circ]$
unit cells	$2 \times 2 \times 4$
framework density	954.29 [kg/m ³]
description	MOF-CJ3
crystallographic data	ref. [64]
void fraction	0.4478[-]
accessible pore volume	0.3441 [cm ³ /g]
nitrogen surface area	870 [m ² /g], 1133 [m ² /cm ³]
optimization	VASP fixed cell, PBE, precision=high
charges	REPEAT with PES from VASP



Bibliography

- [1] E.D. Bloch, W.L. Queen, R. Krishna, J.M. Zadrozny, C.M. Brown, and J.R. Long. Hydrocarbon separations in a metal-organic framework with open iron(II) coordination sites. *Science*, 335:1606–1610, 2012.
- [2] Z.R. Herm, B.M. Wiers, J.M. van Baten, M.R. Hudson, P. Zajdel, C.M. Brown, N. Maschicchi, R. Krishna, and J.R. Long. Separation of hexane isomers in a metal-organic framework with triangular channels. *Science*, 340:960–964, 2013.
- [3] J. Yang, R. Krishna, J. Li, and J. Li. Experiments and simulations on separating a CO₂/CH₄ mixture using K-KFI at low and high pressures. *Microporous Mesoporous Mater.*, 184:21–27, 2014.
- [4] R. Krishna. The Maxwell-Stefan description of mixture diffusion in nanoporous crystalline materials. *Microporous Mesoporous Mater.*, 185:30–50, 2014.
- [5] R. Krishna and J.R. Long. Screening metal-organic frameworks by analysis of transient breakthrough of gas mixtures in a fixed bed adsorber. *J. Phys. Chem. C*, 115:12941–12950, 2011.
- [6] R. Krishna and R. Baur. Modelling issues in zeolite based separation processes. *Sep. Purif. Technol.*, 33:213–253, 2008.
- [7] R. Krishna and R. Baur. Adsorption and reaction in zeolites: Modelling and numerical issues. <http://www.science.uva.nl/research/cr/zeolite/>, 11 November 2003.
- [8] R. Krishna and J.M van Baten. Investigating the potential of MgMOF-74 membranes for CO₂ capture. *J. Membr. Sci.*, 377:249–260, 2011.
- [9] Y. He, R. Krishna, and B. Chen. Metal-organic frameworks with potential for energy-efficient adsorptive separation of light hydrocarbons. *Energy Environ. Sci.*, 5:9107–9120, 2012.
- [10] R. Krishna and J.M. van Baten. A comparison of the CO₂ capture characteristics of zeolites and metal-organic frameworks. *Sep. Purif. Technol.*, 87:120–126, 2012.
- [11] H. Wu, K. Yao, Y. Zhu, B. Li, Z. Shi, and R. Krishna. Cu-TDPAT, an rht-type dual-functional metal-organic framework offering significant potential for use in H₂ and natural gas purification processes operating at high pressures. *J. Phys. Chem. C*, 116:16609–16618, 2012.
- [12] Z. L. Fang, S. R. Zheng, J. B. Tan, S. L. Cai, J. Fun, X. Yan, and W. G. Zhang. Tubular metalorganic framework-based capillary gas chromatography column for separation of alkanes and aromatic positional isomers. *J. Chromatogr. A*, 1285:132–138, 2013.
- [13] M. Tuckerman. *Statistical Mechanics: Theory and Molecular Simulations*. Oxford University Press, New York, 2010.
- [14] M.P. Allen and D.J. Tildesley. *Computer Simulation of Liquids*. Clarendon Press, Oxford, 1987.
- [15] D. Frenkel and B. Smit. *Understanding Molecular Simulation 2nd Edition*. Academic Press, London, UK, 2002.
- [16] D.C. Rapaport. *The Art of Molecular Dynamics Simulation 2nd Edition*. Cambridge University Press, Cambridge, 2004.
- [17] A.R. Leach. *Molecular Modelling: Principles and Applications*. Prentice Hall, Longman, Essex, England, 2nd edition, 2001.

- [18] R.H. Rohrbaugh and P.C. Jurs. Description of molecular shape applied in studies of structure/activity and structure/property relationships. *Anal. Chim. Acta.*, 199:99–109, 1987.
- [19] W.L. Jorgensen, D.S. Maxwell, and J. Tirado-Rives. Development and testing of the opls all-atom force field on conformational energetics and properties of organic liquids. *J. Am. Chem. Soc.*, 118:11225–11236, 1996.
- [20] Accelrys. Materials studio,“ accelrys. 2001-2007 accelrys software inc. <http://accelrys.com/products/materials-studio/index.html>.
- [21] T.J.H. Vlugt and M. Schenk. Influence of framework flexibility on the adsorption properties of hydrocarbons in the zeolite silicalite. *J. Phys. Chem. B.*, 106:12757–12763, 2002.
- [22] D.C. Ford, D. Dubbeldam, and R.Q. Snurr. The effect of framework flexibility on diffusion of small molecules in the metal-organic framework IRMOF-1. *Diffusion Fundamentals III*, 11:1–8, 2009.
- [23] C. Campana, B. Mussard, and T.K. Woo. Electrostatic potential derived atomic charges for periodic systems using a modified error functional. *J. Chem. Theory Comput.*, 5(10):2866–2878, 2009.
- [24] S.L. Mayo, B.D. Olafson, and W.A. Goddard. DREIDING - a generic force-field for molecular simulations. *J. Phys. Chem.*, 94:8897–8909, 1990.
- [25] A.K. Rappé, C.J. Casewit, K.S. Colwell, W.A. Goddard, and W.M.J. Skiff. UFF, a full periodic-table force-field for molecular mechanics and molecular-dynamics simulations. *J. Am. Chem. Soc.*, 114:10024–10035, 1992.
- [26] P. Bai, M. Tsapatsis, and J. I. Siepmann. Trappe-zeo: Transferable potentials for phase equilibria force field for all-silica zeolites. *J. Chem. Phys.*, 117:24375–24387, 2013.
- [27] T. Watanabe, T.A. Manz, and D.S. Sholl. Accurate treatment of electrostatics during molecular adsorption in nanoporous crystals without assigning point charges to framework atoms. *J. Phys. Chem. C*, 115(11):4824–4836, 2011.
- [28] W. Shi and E.J. Maginn. Continuous fractional component Monte Carlo: An adaptive biasing method for open system atomistic simulations. *J. Chem. Theory Comput.*, 3(4):1451–1463, 2007.
- [29] A.P. Lyubartsev A.A. Martsinovski, S.V. Shevkunov, and P.N. Vorontsov-Velyaminov. New approach to Monte Carlo calculation of the free energy: Method of expanded ensembles. *J. Chem. Phys.*, 96(3):1776–1783, 1992.
- [30] F.A. Escobedo and J.J. de Pablo. Expanded grand canonical and Gibbs ensemble Monte Carlo simulation of polymers. *J. Chem. Phys.*, 105(10):4391–4394, 1996.
- [31] S. Duane, A.D. Kennedy, B.J. Pendleton, and D. Roweth. Hybrid Monte Carlo. *Phys. Lett. B*, 195:216–222, 1987.
- [32] S. Chempath, L.A. Clark, and R.Q. Snurr. Two general methods for grand canonical ensemble simulation of molecules with internal flexibility. *J. Chem. Phys.*, 118(16):7635–7643, 2003.
- [33] W. Shi and E.J. Maginn. Improvement in molecule exchange efficiency in Gibbs ensemble Monte Carlo: Development and implementation of the continuous fractional component move. *J. Comput. Chem.*, 29(15):2520–2530, 2008.
- [34] D. Dubbeldam, A.T. Knoop, and K.S. Walton. On the inner workings of monte carlo codes. *Mol. Simulat.*, 39(14-15):1253–1292, 2013.
- [35] T.W. Rosch and E.J. Maginn. Reaction ensemble monte carlo simulation of complex molecular systems. *J. Chem. Theory Comput.*, 7:269–279, 2011.
- [36] F. Wang and D.P. Landau. Determining the density of states for classical statistical models: A random walk algorithm to produce a flat histogram. *Phys. Rev. E*, 64:056101, 2001.

- [37] F. Wang and D.P. Landau. Efficient, multiple-range random walk algorithm to calculate the density of states. *Phys. Rev. Lett.*, 86(10):2050–2053, 2001.
- [38] M. Minceva and A. Rodrigues. Adsorption of xylenes on faujasite type zeolite: Equilibrium and kinetics in batch adsorber. *Chemical Engineering Research and Design*, 82:667–681, 2004.
- [39] J.M. Newsam, M.M.J. Treacy, W. T. Koetsier, and C.B. de Gruyter. Structural characterization of zeolite beta. *Proc. Roy. Soc. A (London)*, 420:375–405, 1988.
- [40] T. Wessels, Ch. Baerlocher, L.B. McCusker, and E.J. Croyghton. An ordered form of the extra-large-pore zeolite UTD-1: Synthesis and structure analysis from powder diffraction data. *J. Am. Chem. Soc.*, 121:6242–6247, 1999.
- [41] Ch. Baerlocher, L.B. McCusker, and R. Chiappetta. Location of the 18-crown-6 template in EMC-2 (EMT). rietveld refinement of the calcined and as-synthesized forms. *Microporous Mater.*, 2:269–280, 1994.
- [42] J.J. Hriljac, M.M. Eddy, A.K. Cheetham, J.A. Donohue, and G.J. Ray. Powder neutron diffraction and Si-29 MAS NMR studies of siliceous zeolite-Y. *J. Solid State Chem.*, 106:66–72, 1993.
- [43] J.M. Newsam. Structures of dehydrated potassium zeolite-L at 298-K and 78-K and at 78-K containing sorbed perdeuteriobenzen. *J. Phys. Chem.*, 93:7689–7694, 1989.
- [44] D.H. Olson, G.T. Kokotailo, S.L. Lawton, and W.M. Meier. Crystal structure and structure-related properties of ZSM-5. *J. Phys. Chem.*, 85:2238–2243, 1981.
- [45] H. van Koningsveld, H. van Bekkum, and J.C. Jansen. On the location and disorder of the tetrapropylammonium (TPA) ion in zeolite ZSM-5 with improved framework accuracy. *Acta Cryst. B*, 43:127–132, 1987.
- [46] H. van Koningsveld, J. C. Jansen, , and H. van Bekkum. The monoclinic framework structure of zeolite H-ZSM-5. comparison with the orthorhombic framework of as-synthesized ZSM-5. *Zeolites*, 10:235–242, 1990.
- [47] H. van Koningsveld and et al. The location of p-xylene in a single cristal of zeolite H-ZSM-5 with a new sorbate-induced, orthorhombic framework symmetry. *Acta. Cryst.*, B45:423–431, 1989.
- [48] V. Gramlich. Untersuchung und verfeinerung pseudosymmetrischer strukturen. *Ph.D. Thesis, ETH, Zürich, Switzerland*, 1971.
- [49] J.L. Schlenker, J.L., Rohrbaugh, W.J., Chu, P., Valyocsik, E.W., and G. T. Kokotailo. The framework topology of ZSM-48: a high silica zeolite. *Zeolites*, 5:355–358, 1985.
- [50] C.A. Fyfe, H. Gies, G.T. Kokotailo, B. Marler, , and D.E. Cox. Crystal structure of silica-ZSM-12 by the combined use of high-resolution solid-state MAS NMR spectroscopy and synchrotron x-ray powder diffraction. *J. Phys. Chem.*, 94:3718–3721, 1990.
- [51] H. Li, M. Eddaoudi, M. O’Keeffe, and O. M. Yaghi. *Nature*, 402:276, 1999.
- [52] M. Dinca H.J. Choi and J.R. Long. Broadly hysteretic H₂ adsorption in the microporous metal-organic framework Co(1,4-benzenedipyrazolate). *J. Am. Chem. Soc.*, 130:7848–7850, 2008.
- [53] P.D.C. Dietzel, Y. Morita, R. Blom, and H. Fjellvag. *Angew. Chem. Int. Ed*, 44:6354, 2005.
- [54] C.-T. He, J.-Y. Tian, S.-Y. Liu, G. Ouyang, J.-P. Zhang, and X.-M. Chen. A porous coordination framework for highly sensitive and selective solid-phase microextraction of non-polar volatile organic compounds. *Chem. Sci.*, 4:351–356, 2013.
- [55] Z. Jin, H.-Y. Zhao, X.-J. Zhao, Q.-R. Fang, J.R. Long, and G.-S. Zhu. A novel microporous mof with the capability of selective adsorption of xylenesw. *Chem. Comm*, 46:8612–8614, 2010.
- [56] P.D.C. Dietzel, B. Panella, M. Hirscher, R. Blom, and H. Fjellvag. *Chem. Comm*, page 959, 2006.

- [57] H. Ren, T. Ben, E. Wang, X. Jing, M. Xue, B. Liu, Y. Cui, S. Qiu, and G. Zhu. *Chem. Comm*, 46:291–239, 2010.
- [58] J.S. Cavka, S. Jakobsen, U. Olsbye, N. Guillou, C. Lamberti, S. Bordiga, and K.P. Lillerud. A new zirconium inorganic building brick forming metal organic frameworks with exceptional stability. *J. Am. Chem. Soc.*, 130:13850–13851, 2008.
- [59] J.L.C. Rowsell and O.M. Yaghi. *J. Am. Chem. Soc.*, 128:1304, 2006.
- [60] M. Dan-Hardi, C. Serre, T.F. Frot, L. Rozes, G. Maurin, C. Sanchez, and G.A. Ferey. New photoactive crystalline highly porous titanium(IV) dicarboxylate. *J. Am. Chem. Soc.*, 131:10857–10859, 2009.
- [61] Y. Fu, D. Sun, Y. Chen, R. Huang, Z. Ding, X. Fu, and Z. Li. An amine-functionalized titanium metal-organic framework photo-catalyst with visible-light-induced activity for CO₂ reduction. *Angew. Chem. Int. Ed.*, 124:3420–3423, 2012.
- [62] K. Barthelet, J. Marrot, D. Riou, and G. Ferey. A breathing hybrid organic-inorganic solid with very large pores and high magnetic characteristics. *Ang. Chem. Int. Ed.*, 41:281–284, 2002.
- [63] C. Serre, F. Millange, C. Thouvenot, M. Nogues, G. Marsolier, D. Louer, and G. Ferey. *J. Am. Chem. Soc.*, 124:13519–13526, 2002.
- [64] Z.L. Fang, S.R. Zheng, J.B. Tan, S.L. Cai, J. Fan, X. Yan, and W.G. Zhang. Tubular metal-organic framework-based capillary gas chromatography column for separation of alkanes and aromatic positional isomers. *Journal of Chromatography A*, pages 132–8, 2013.